The role of the surface chemistry on the performance of graphene-based biosensors

Vladyslav Mishyn

Vladyslav Mishyn. The role of the surface chemistry on the performance of graphene-based biosensors. Micro and nanotechnologies/Microelectronics. Université de Lille, 2021. English. NNT : 2021LILUN021 . tel-03917532

HAL Id: tel-03917532
https://theses.hal.science/tel-03917532

Submitted on 2 Jan 2023

THESE

Présentée à l'Université de Lille

SPI-ENGSYS

Pour obtenir le grade de :

DOCTEUR DE L'UNIVERSITE

Spécialité: MICRO ET NANO TECHNOLOGIES, ACOUSTIQUE ET TÉLÉCOMMUNICATIONS

présenté par

Vladyslav MISHYN

Le rôle de la chimie de surface sur la performance de biocapteurs à base de graphène

The role of the surface chemistry on the performance of graphene-based biosensors

Soutenue le 9 décembre 2021 devant la Commission d'examen.

Membres du jury :

Dr. Thomas DONEUX	Rapporteur (Université Libre de Bruxelles)
Prof. Christophe VIEU	Rapporteur (LAAS – Toulouse)
Prof. Wolfgang KNOLL	Examinateur (AIT – Vienne)
Dr. Rabah BOUKHERROUB	Président du jury (IEMN – Lille)
Prof. Henri HAPPY	Directeur de thèse (IEMN – Lille)
Prof. Sabine SZUNERITS	Co-Directrice de thèse (IEMN – Lille)

Abstract

Clinical analysis benefits world-wide from a variety of diagnostic tests. The interest in the development of new clinical tests is not only driven by the demand to sense new analytes such as viruses and biomarkers, but also to reduce costs, complexity and lengthy analysis times of current techniques. Among the numerous of possibilities available today, point-of-care (PoC) devices incorporating graphene and its derivatives are prominent players. This work aims at investigating and comparing the potential of reduced graphene oxide (rGO) and graphene formed by chemical vapor deposition (CVD) for electrical and electrochemical based PoC devices. The full biosensor manufacturing process from manufacturing of the graphene-based transducers to sensing biological molecules is described. A focus will be on the choice of the surface receptors anchored onto graphene. In this context, non-covalent receptor attachment using different pyrene-based ligands and the interest of covalent attachment *via* 4-((triisopropylsilyl)ethylenyl)benzene diazonium salts will be compared. Sensing examples discusses are based on the detection of the E7 capsid protein of the human papillomavirus (HPV), folic acid (FA) and the level of cardiac troponin I (cTnI), associated with cardiovascular diseases, in different biological samples.

Keywords: graphene, reduced graphene oxide, sensing, electrochemistry, field-effect transistors, surface chemistry.

Résumé

L'analyse clinique bénéficie dans le monde entier d'une variété de tests diagnostiques. L'intérêt pour le développement de nouveaux tests cliniques résulte d'une part du besoin de détecter de nouveaux analytes tels que les virus et les biomarqueurs, ainsi que d'une forte demande pour la réduction des coûts, de la complexité et des temps d'analyse excessif des techniques actuelles. Parmi les nombreuses possibilités disponibles aujourd'hui, les dispositifs de type « point-of-care » (PoC) incorporant du graphène et ses dérivés sont des acteurs de premier plan. Ce travail vise à étudier et à comparer le potentiel de l'oxyde de graphène réduit (rGO) et du graphène formé par dépôt chimique en phase vapeur (CVD) pour les dispositifs PoC à transduction électrique et électrochimique. Le développement complet des biocapteurs, de la fabrication des transducteurs à base de graphène à la détection de molécules biologiques, est présenté. L'accent sera mis sur le choix des récepteurs greffés à la surface du graphène. Dans ce contexte, le greffage non-covalent de récepteurs utilisant différents ligands à base de pyrène ainsi que le greffage covalent *via* des sels de 4 - ((triisopropylsilyl)éthylényl)benzène diazonium seront comparés. Les exemples de détection discutés sont basés sur la détection de la protéine de capside E7 du papillomavirus humain (PVH), acide folique (FA) et sur le niveau de troponine cardiaque I (cTnI) associé aux maladies cardiovasculaires, dans différents échantillons biologiques.

Mots clés: graphène, oxyde de graphène réduit, détection, électrochimie, transistors à base de graphène, chimie de surface.

Table of content

Acknowledgments

This work has been conducted in two different research groups: NanoBioInterfaces (NBI) and Carbon at the Institute of Electronics, Microelectronics and Nanotechnology (IEMN). I would also like to thank the Biosensor Technologies (BST) group and the group's leader Prof. Wolfgang Knoll to have such a nice opportunity to work in the Austrian Institute of Technology. This close collaboration between the two institutions made this work possible. The financial support by the University of Lille is highly acknowledged.

I am extremely grateful to my supervisors Prof. Sabine Szunerits and Prof. Henri Happy for their scientific advices and support during all these years. It was multitasking and interesting work through which I acquired lots of essential skills and made new connections. This is an excellent experience and a huge jump to my future career.

This thesis was only possible because of the special care and help of my colleagues: Rabah Boukherroub, Alexandre Barras, Wei Wei, Di Zhou, Emiliano Pallecchi, François Vaurette and Quentin Pagneux. You are the most talented people I know and I am really grateful for your advices.

I would like to thank especially my friends who made life better and meaningful. All of you was a source of my inspiration and motivation: Chiara D'Onofrio, Patrik Aspermair, Anil Bozdogan, Anton Pylypenko, Leonid Kozachenko, Denys Shynkarenko, Anton Homon, Yurii Boyko, Milica Budimir, Agathe Deveraux, Ioana Silvia Hosu, Ulrich Ramach, Bernadette Lechner, Anne Schuchanegg, Aleksandra Loczechin, Mathias Dolci, Michele Lodato, Teresa Rodrigues, Ines de Hoon, Soukaina Ben Salk, Tomasz Swebocki, Marie-Helene Polt and Yuanyuan Miao. It is my great pleasure to have you in my life.

I would like to express my gratitude to my family and my dear Anna. You were supporting me all these years through ups and downs. This means everything to me. I extend my thanks to my new family member cat Baudelaire, who is the cutest cat in the world.

Abbreviations

2

2PDS	Dithiodipyridine

A

Ab	Antibody
AFM	Atomic force microscopy
AMI	Acute myocardial infarction
AMI	Acute myocardial infarction
APTES	3-aminopropyltriethoxysilane

B

BSA	Bovine serum albumin

C

CDR	Complementarity determining regions
CNP	Charge neutrality point
cTnI	Cardiac troponin I
CV	Cyclic voltammetry
CVD	Chemical vapor deposition

D

DMF	N, N-Dimethylformamide
DMSO	Dimethyl sulfoxide
DNA	Deoxyribonucleic acid
dopa-CD	β-cyclodextrin-modified dopamine
DPV	Differential pulse voltammetry
DTT	Dithiothreitol

E

EDC	1-ethyl-3-(3-dimethyl aminopropyl)-carbodiimide
EDTA	Ethylenediaminetetraacetic acid
EIS	Impedance spectroscopy
ELISA	Enzyme-Linked Immunosorbent Assay
EPD	Electrophoretic deposition

F

FA	Folic acid
Fab	Antigen-binding fragment
Fc	Ferrocene
F_{const}	Constant fragment
FET	Field-effect transistor

G

GFET	Graphene field-effect transistor
GO	Graphene oxide

H

HMDS	Hexamethyldisilazane
HPLC	High-performance liquid chromatography
HPV	Human papillomavirus

I

IDE	Interdigitated electrodes

L

LOD	Limit of detection

N

NHS	N-Hydroxysuccinimide

P

PBA	1-pyrenebutyric acid

PBASE	1-Pyrenebutyric acid N-hydroxysuccinimide ester
PBS	Phosphate-Buffered Saline
PCR	Polymerase chain reaction
PEG	Polyethylene glycol
PEI	Polyethyleneimine
PMAL	Pyrene-propanoic amid ethylmaleimide
PMMA	Poly(methyl methacrylate)
PoC	Point-of-care
prGO	Porous reduced graphene oxide
PSE	Pyrene-conjugated dithiopyridine
PyPEG	Pyrene-conjugated polyethylene glycole
R	
rGO	Reduced graphene oxide
RMS	Root mean square average roughness
RNA	Ribonucleic acid
RIE	Reactive ion etching
RMS	Root mean square
S	
SAM	Self-Assembled Monolayer
SELEX	Systemic evolution of ligands by exponential enrichment
SEM	Scanning Electron Microscopy
T	
TBAF	Tetrabutylammonium fluoride
$TBAPF_6$	Tetrabutylammonium hexafluorophosphate
THF	Tetrahydrofuran
TIPS	Triisopropylsilyl protective group
TMPS	Trimethoxyphenylsilane
U	
UV	Ultraviolet
X	
XPS	X-ray photoelectron spectroscopy

Objectives

This thesis is dedicated to the development and surface modification of graphene-based interfaces with the ultimate goal of biosensing. Different graphene derivatives are used in combination with covalent and non-covalent modification strategies to detect analytes such as folic acid (FA), cardiac troponin I (cTnI) and the E7 protein of human papillomavirus (E7 HPV). Various characterization techniques (Raman imaging and spectroscopy, scanning electron microscopy (SEM), atomic force microscopy (AFM), X-ray photoelectron spectroscopy (XPS)) are combined with electrical and electrochemical detection approaches to elucidate the role of the surface chemistry on the performance of graphene-based biosensors.

Chapter 1 gives a general introduction into the biosensing field. It provides the information about diverse graphene materials used as a transducer, its advantages and limitations. Different approaches of electrical and electrochemical detections techniques such as cyclic voltammetry (CV), differential pulse voltammetry (DPV) and graphene field-effect transistor (GFET) will be introduced. The Langmuir adsorption model will be presented to describe the kinetics of binding reactions in biosensing field. This chapter also highlights the surface chemistry strategies for graphene modification as a key component for the sensitive and selective biosensing.

Chapter 2 is dedicated to the development of an electrochemical biosensors based on reduced graphene oxide (rGO). The process of electrophoretic deposition (EPD) of graphene materials is optimized in order to obtain robust and stable rGO-coated electrodes. These electrodes are covalently modified using a triisopropylsilyl (TIPS)-protected ethynyl aryldiazonium salt which avoids the formation of multilayers as mostly observed with diazonium chemistry. Following the full characterization and quantification of the active sites, the ethynyl-terminated electrodes are used for biosensing of cardiac biomarker troponin I (cTnI) *via* covalent coupling of the corresponding aptamer to the interface. On the other hand, a classical three-electrodes system is developed on a flexible substrate for advanced sensing of folic acid (FA). These electrodes are modified with reduced graphene oxide (rGO)/polyethyleneimine (PEI) and non-covalently coupled with β-cyclodextrin-modified dopamine (dopa-CD) to capture FA.

Chapter 3 outlines the development of electrical sensors based on a liquid-gated reduced graphene oxide field-effect transistor (rGO FET). The full process from the interface pre-treatment to the deposition and reduction of graphene oxide (GO) will be reported. The influence of pH, ionic strength and Debye screening length on nonspecific detection of bovine serum albumin (BSA) will be investigated to show the advantages and the limitations of rGO FET. Furthermore, the rGO interface will be modified with 1-byrenebutyric acid (PBA) *via* π-π stacking and then with the aptamer *via* NHS/EDC protocol for the detection of E7 protein of human papillomavirus.

Chapter 4 reports the manufacturing of chemical vapor deposited graphene field-effect transistors (CVD GFET) and its electrical properties such as ambipolar transistor characteristics, stability and pH susceptibility. rGO and CVD GFETs will be compared and the advantages and the limitations of each will be demonstrated. The triisopropylsilyl (TIPS)-protected ethynyl aryldiazonium surface chemistry will be performed aiming to obtain ethynyl-terminated functional monolayer with the improved electrical characteristics. These interfaces will be further used for electrical sensing of cardiac biomarker troponin I (cTnI).

Chapter 5 is devoted to the pyrene-based ligands that are the most widely used graphene surface anchors for sensing related applications. A systematic Raman and electrochemical investigation on the reaction conditions will be employed and influence of pyrene functionalities will be reported. The use of pyrene-maleimide and pyrene-conjugated dithiopyridine is highlighted as being more advantageous over 1-pyrenbutyric acid and 1-pyrenebutyric acid N-hydroxysuccinimide ester concluded on spectral and electrochemical investigation utilizing ferrocene derivatives.

Chapter 6 summarizes the results and presents some perspectives on the work.

Chapter 1: Introduction

1.1. Introduction to biosensors

Biosensors are analytical devices that convert a receptor/ target biomolecule reaction into a measurable signal (e.g. electrical, magnetic, optical etc.), which correlates to the analyte concentration.[1] A classic biosensor architecture consists of two elements: a surface linked biorecognition element that interacts selectively with the target molecule in physiological medium and a transducer for the detection of the biological reaction on the interface (**Figure 1.1**).[2] Traditional *in vitro* diagnostics such as HPLC, ELISA, 2D gel electrophoresis or mass-spectrometry are time-consuming and require centralized laboratories, experienced personnel and bulky equipment. Compared to conventional biochemical assays such as immunoassays and polymerase chain reaction-based strategies, biosensors benefit from the fast response time (normally several minutes), minimum need for operator input and high specificity. The first biosensor reported dates back to the work by Leland C. Clark,[3] who is considered to be the father of biosensors. Based on his experience with the oxygen electrode, he proposed making electrochemical sensors more intelligent by entrapping enzymes such as glucose oxidase onto the oxygen electrode using a dialysis membrane.[4] In presence of the enzyme and O_2, glucose is oxidized into gluconic acid and hydrogen peroxide. The concentration of glucose in the blood sample is indirectly determined by monitoring the O_2 consumption. This glucose analyzer became commercially available in 1975 in the form of an amperometric sensor. Since then myriads of biosensors technologies have been developed covering a broad range of applications.

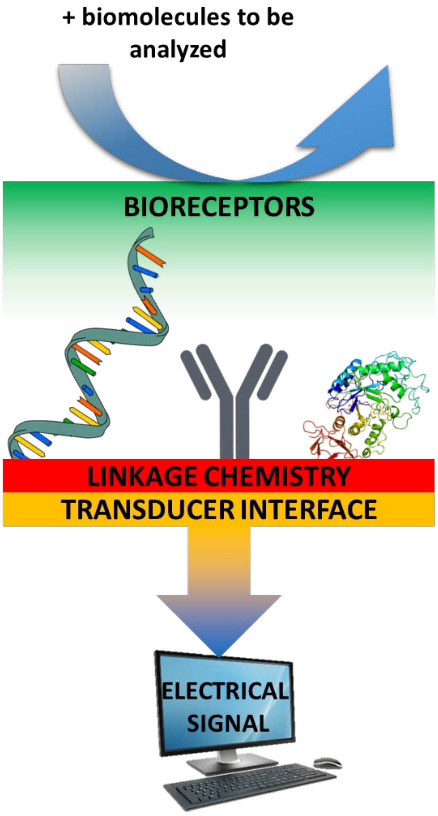

Figure 1.1: Biosensor basic architecture.

There are several classes of biorecognition elements: proteins (e.g. enzymes and antibodies), nucleic acids and aptamers, synthetic (e.g. molecularly imprinted polymers or dopamine-modified cyclodextrins).[5-6] Though all of them aim to provide the specificity of the biosensor, the choice of the receptor relies first of all on a target analyte. Such factors as stability of the sensor, cost and the most importantly the affinity constant have to be considered.

Proteins are large biomolecules that are constituted of one or more long chains of amino acid residues. They perform vast functionalities in living organisms, including catalyzing metabolic reactions, providing structure to cells and organisms, transportation etc.[7] Each protein folds in a unique 3D structure depending on a defined amino acid sequence and surrounding conditions such as pH, temperature and solvent. The primary structure corresponds to a polypeptide chain molecular level. The secondary structure is an evolved structure of the primary level consisting of local patterns stabilized by hydrogen bonds (α-helix and β-sheets). The tertiary structure reveals 3D shape of a protein. More complex associations of several protein units is called the quaternary structure (**Figure 1.2**).[8]

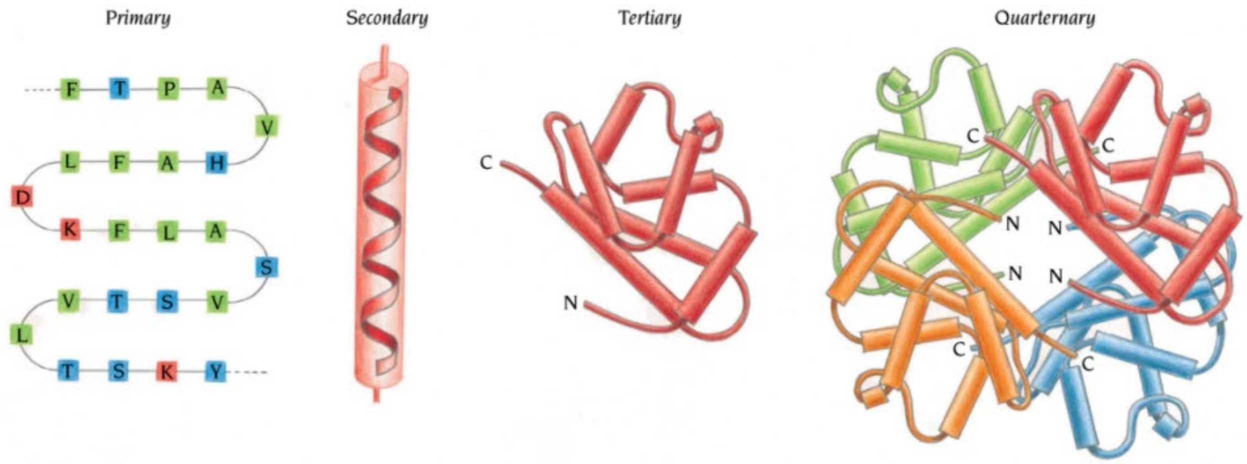

Figure 1.2: Four types of protein structure: primary: amino acid sequence of a protein polypeptide; secondary: a local regularly structure such as α-helix and β-sheets; ternary: packing such structural elements into a compact globular 3D domain unit; quaternary: final protein that might contain several polypeptide chains (reprinted from [8]).

An enzyme is a protein molecule that acts as a catalyst in living organisms.[9] Enzymes specifically capture a target bioanalyte with binding cavities buried within their 3D structure, using non-covalent interactions to form recognition pattern.[10] Following bioanalyte binding an intermediate complex is formed before release of the measurable end product (**Figure 1.3a**). The product of this catalytic reaction is often monitored by utilizing amperometric or electrochemical transduction methods.[11] A very short diffusion pathway to the transducer interface is necessary to detect the product of reaction.

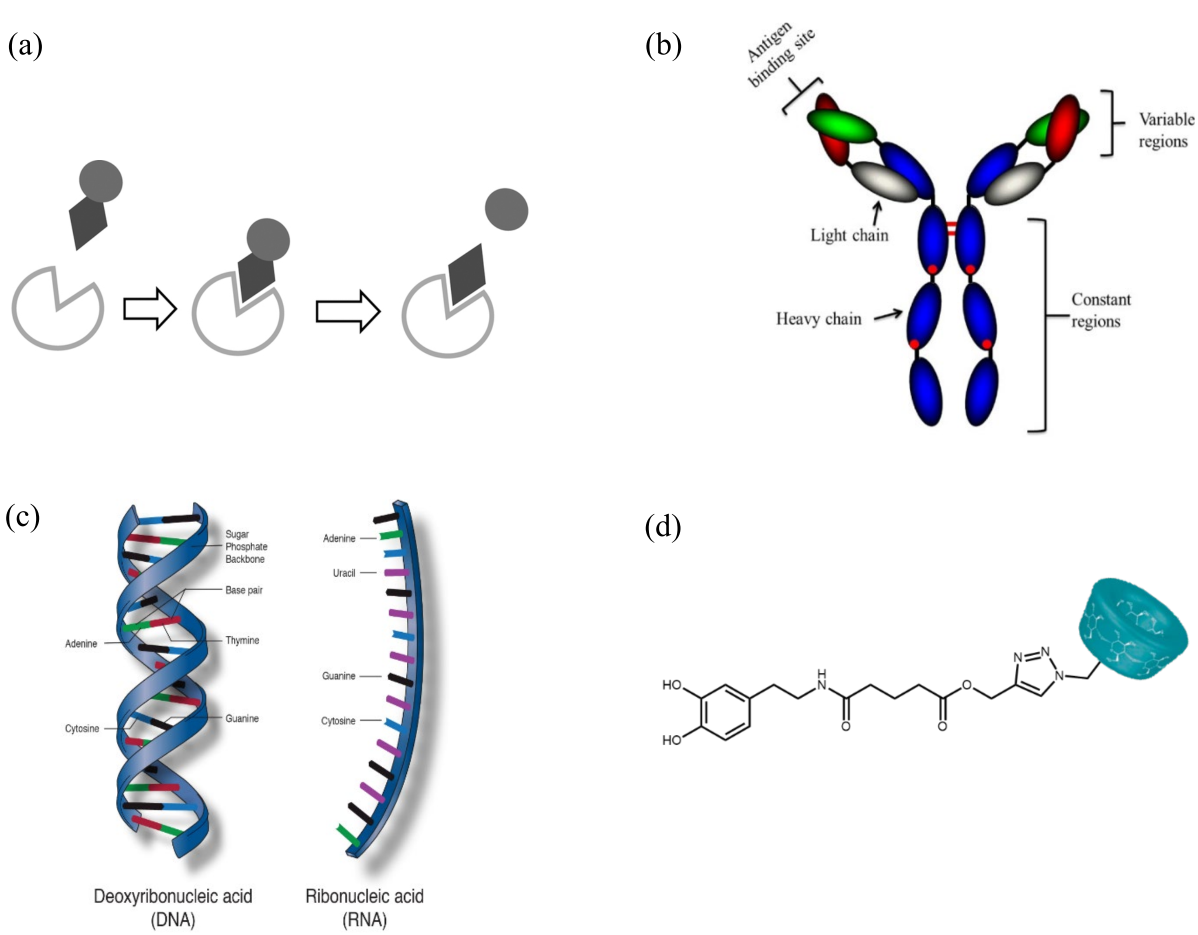

Figure 1.3: Receptors for biosensing: (a) an enzymatic reaction: target bioanalyte binds active site (left) to form bioanalyte-enzyme complex (middle) where a catalytic reaction converts target bioanalyte to measurable reaction product (dark circle, right) (adapted from [5]); (b) Structure of an antibody (Ab) (adapted from [12]); (c) nucleic acids structure (reprinted from [23]); (d) dopamine-modified cyclodextrin as an example of synthetic biorecognition element (adapted from [6]).

Antibodies (Ab), also called immunoglobulins, are large Y-shaped proteins (**Figure 1.3b**) produced by plasma cells that are utilized by the immune system to identify and target pathogens such as bacteria and viruses.[12] A typical Ab is a large molecule of about 150 kDa made up of four peptide chains: two heavy chains with molecular weights of 50 kDa and two light chains (25 kDa molecular weight) linked by disulphide bonds.[13] Ab can be subdivided in two principal blocks: the antigen-binding fragment (Fab) and the constant fragment (F_{const}). The F_{const} is common to a given type of immunoglobulin and it is not involved into the antigen biorecognition. Antigen binding is mediated by the variable regions, known as the complementarity determining regions (CDRs).[13] The antigen binding site is called paratope. The paratope binds specifically the epitope similar to lock and key mechanism. Antibody-based biosensors are called immunosensors with the most common application in the enzyme-linked immunosorbent assay (ELISA) first introduced by

Engvall and Perlmann in 1971.[14-16] The ELISA kits for the detection of cardiac biomarker Troponin I (cTnI) are available commercially with the lowest limit of detection of 4.4 pg mL^{-1} and became a golden standard for monitoring the onset and progress of cardiovascular diseases. The electrochemical immunosensors also found its niche in label-free sensing of gliadin in food samples,[17] cardiac marker cTnI,[18] uropathogenic *Escherichia coli*[19] and others with a typical linear range in ng mL^{-1} concentrations.

Antibodies and enzymes suffer from the costly manufacturing, limited chemical stability with binding properties strongly depending on pH and temperature.[20-21] The surface linkage is also constrained as proteins require mild conditions and the functional groups are difficult to introduce in the protein's structure. Though the antibodies and enzymes are widely used and well reported, they were not utilized in this work giving the preferences to more robust and novel receptors such aptamers and synthetic capturing molecules introduced below.

Nucleic acids, deoxyribonucleic acid (DNA) and ribonucleic acid (RNA), are charged biopolymers conserving the genetic information essential for all living organisms (**Figure 1.3c**).[22-23] They consist of nucleotides, which are the monomers made of three components: a 5-carbon sugar, a phosphate group and a nitrogenous base. If the sugar is ribose, the polymer is RNA; if the sugar is the ribose derivative deoxyribose, the polymer is called DNA. The phosphate bond links the monomers in a chain and provides a charged skeleton to the molecule. The nitrogenous bases are nucleobases, which are: adenine, cytosine, guanine, thymine, and uracil. Thymine is present only in DNA and uracil only in RNA. While RNA is generally single stranded, DNA arranges into a double helix, resulting from the complementary base coupling between two single strands. This process, known as hybridization, is highly selective since a single base mismatch between two hybridized strands can strongly destabilize the complex.[24] The formed DNA or RNA chain is arranged in a unique sequence different in length and nucleobases sequence.

Aptamers are short single strands of synthetic DNA or RNA designed through a combinatorial selection process called Systemic Evolution of Ligands by Exponential Enrichment (SELEX) shown in **Figure 1.4**.[25] This is a combinatorial *in vitro* technique where a library of randomly generated oligonucleotide sequences is introduced to a target analyte ensuring a selective and strong interaction pair. Unbound aptamer sequences are then removed only retaining bound aptamer sequences for polymerase chain reaction (PCR) amplification to regenerate the oligonucleotide library for the next SELEX round.[5] In contrast to proteins which production depend on the immunization of animals and the cell culture techniques, the aptamers can be synthesized at low cost with on-demand sequences. Along with that, the terminal groups such as amine, azide or thiol can be easily introduced to the aptamer chain making them perfect candidates for interface modification. These receptors are also more chemically stable and can undergo metal catalyzed reactions (e.g. Huisgen 1,3-dipolar cycloaddition) without altering the aptamer properties. The aptamers are used in much wider range of biosensor applications: from small molecules to proteins and whole cells with nano to femtomolar afinity.[25-26]

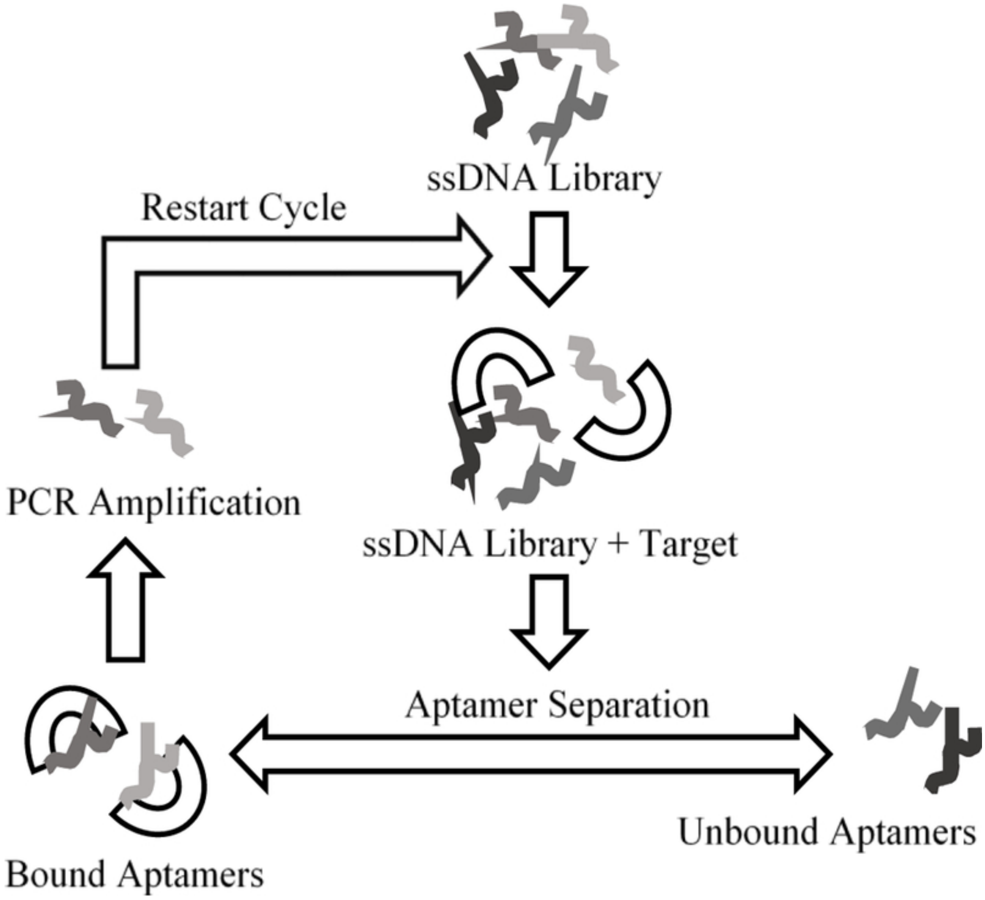

Figure 1.4: Systemic Evolution of Ligands by Exponential Enrichment (SELEX): a library of random sequences of single strands of synthetic DNA (ssDNA) reacting with a target analyte. Unbound ssDNA is removed while those which are bound undergo PCR amplification. The cycle can be repeated several times to select the candidate with the lowest K_D (reprinted from [5]).

Bioreceptors are not limited to proteins and nucleic acids. Synthetic biorecognition elements are artificially synthesized to mimic biologically defined interactions *via* hydrogen bonds, 3D cavities, hydrophobic and hydrophilic reciprocity and other weak non-covalent interactions.[5] These pseudo-natural bioreceptors are synthesized by using natural subunits and cannot be fully discussed within this work. As an example, anchoring β-cyclodextrins to dopamine molecule results in bifunctional biological receptor (**Figure 1.3d**). The dopamine functionality acts as an anchoring side *via* π-π interactions on such material as graphene, while the cyclodextrin's hydrophilic shell and hydrophobic cavity can host various organic and inorganic guest molecules such as dopamine,[27] ascorbic acid,[28] uric acid[29] and tryptophan.[30] The synthetic biorecognition elements benefit from the desirable chemical functionalities, superior stability and reproducibility.

The kinetics of binding reactions in biosensing field, such as antigen to antibody or protein to aptamer, is usually described by the Langmuir adsorption model.[31] The model represents the adsorption of analyte on a solid interface with a finite number of binding sites (receptors) at certain conditions (temperature, volume and pressure). The model can be applied to a homogeneous monolayer approximation where the neighboring receptors do not influence the adsorption of one binding site. If all conditions are fulfilled, the equilibrium equation can be written as:

$$[Receptor] + [Analyte] \leftrightarrows [Receptor - Analyte] \qquad Equation\ 1.1$$

The forward reaction, the adsorption, is described by the association rate constant k_{on} in $M^{-1}\ s^{-1}$, while the reverse reaction, the desorption, is associated with the dissociation rate constant k_{off} in s^{-1}. The dissociation constant (K_D) is the ratio of the dissociation rate constant k_{off} to the association rate constant k_{on}. K_D is giving the dissociation value between the analyte and receptor in molar units (M): the lower K_D the higher affinity. The dissociation constant can be also expressed as a ratio of the product of equilibrium concentrations of analyte and receptor to the equilibrium concentration of receptor-analyte complex. On the other hand, the association constant represents binding affinity value and is the inverse of the dissociation constant resulting in M^{-1} units. The overall result can be written as:

$$K_D = \frac{k_{off}}{k_{on}} = \frac{[Analyte][Receptor]}{[Receptor - Analyte]} \qquad Equation\ 1.2$$

$$K_A = K_D^{-1} = \frac{[Receptor - Analyte]}{[Receptor][Analyte]} \qquad Equation\ 1.3$$

The Langmuir adsorption model explains adsorption by assuming isothermal conditions. The model describes the surface coverage, where θ is the fractional occupancy of the adsorption sites (from 0 to 1) of formed complex receptor-analyte with respect to the total amount of binding sites. Under the assumption that the equilibrium concentration of analyte equals to the initial concentration of analyte (C_A) due to a constant inflow of the analyte, the Langmuir isotherm can be expressed as:

$$\theta = \frac{K_A\, C_A}{1 + K_A C_A} \qquad Equation\ 1.4$$

For instance, the Langmuir isotherm observed for the binding of Eugenol (analyte) to OBP14 (receptor) from the honey bee is demonstrated in **Figure 1.5a-b**.[31] The K_D value is determined at half saturation where 50 % of the binding sites are occupied. The value has a great importance in the biosensing area as it defines working concentrations range and allows to compare the data from different biosensors and the literature. Furthermore, the Langmuir isotherm fit can be used for biosensor calibration by reference measurements with a known analyte concentration.

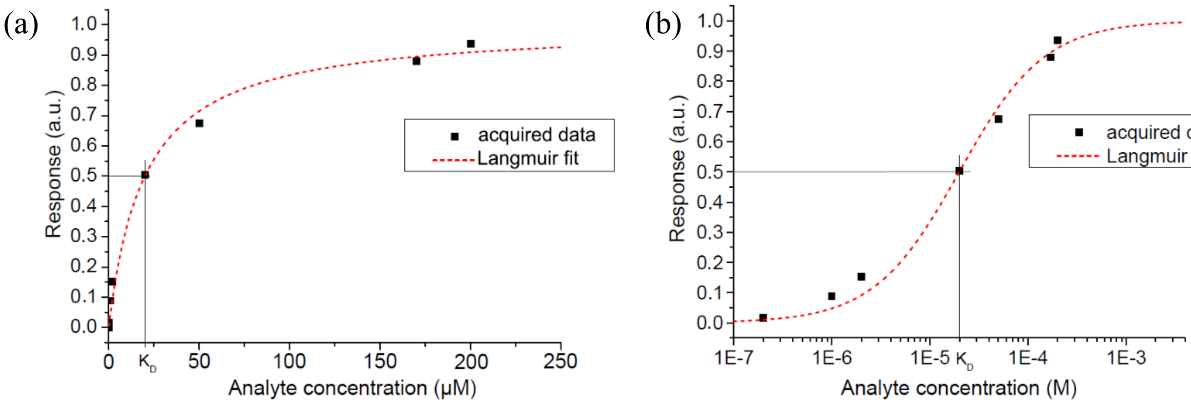

Figure 1.5: Langmuir isotherm observed for the binding of Eugenol (analyte) to OBP14 (receptor) from the honey bee: (a) linear-linear scale and (b) linear-logarithm scale. The K_D value can be found at half saturation where 50 % of the binding sites are occupied (reprinted from [31]).

1.2. Graphene-based transducers

The transducer is an element that converts the bio-recognition event into a measurable signal. Aiming to achieve requested picomolar (pM) limit of detection (LOD) for target biomolecules, nanomaterials have been widely studied as candidates for transducer coatings.[32-35] These materials allow to increase the number of immobilized receptors thus enhancing the signal read-out. Among the different nanomaterials considered, graphene and its various derivatives such as chemical vapor deposited (CVD) graphene, graphene oxide (GO), reduced graphene oxide (rGO) and the other forms of carbon material have received worldwide attention for the development of biosensors (**Figure 1.6**). Graphene is a one-atom-thick material consisting of sp^2-bonded carbon with a honeycomb structure.[36] Different electrical (graphene field-effect transistors(GFETs)) and electrochemical (cyclic voltammetry (CV), differential pulse voltammetry (DPV), impedance spectroscopy (EIS)) techniques have been used on graphene-modified electrodes due to its high electron transfer rates,[37] high charge-carrier mobility[38] and possibility being modified utilizing various approaches.[1, 39-41] Furthermore, chemically derived graphene derivatives contain a high density of charged functional groups along with edge-plane defects sites, providing many active sites for electron transfer and making these materials perfect candidates for the electrophoretic deposition on the different conductive interfaces.[42] Independent of the detection method adopted, the presence of hydrophobic domains of sp^2 honeycomb structure on graphene-based transducers renders them an excellent possibility for non-covalent immobilization of biomolecules.[43] Along with these benefits, the control of non-specific interactions remains very important for a sensitive and selective biosensing. Improvement of the antifouling properties of the interfaces is one of essential steps in the development of high-performance graphene biosensor.

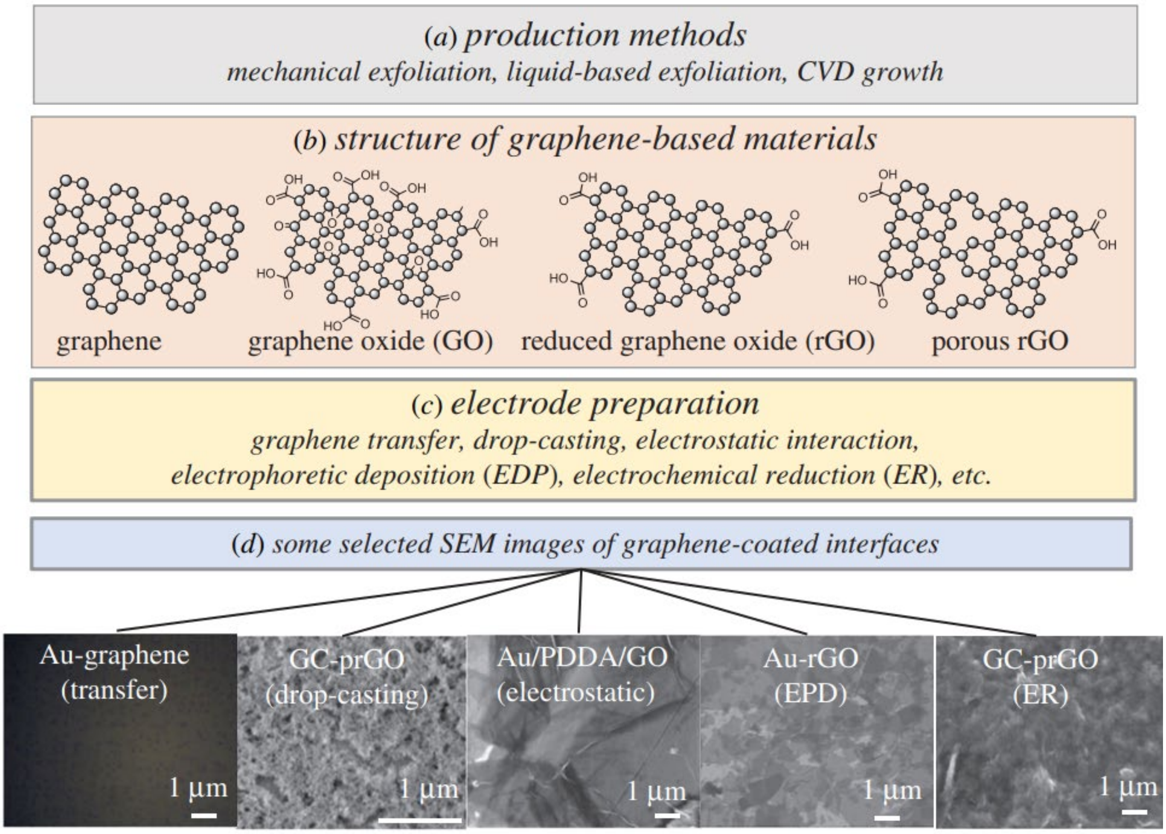

Figure 1.6: Construction of graphene-based interfaces: (a) fabrication methods of graphene; (b) chemical structures of different graphene derivatives widely used for biosensing; (c) methods for the transfer of graphene-based materials to solid substrates; (d) scanning electron microscopy (SEM) images of graphene-coated interfaces using different deposition methods and different graphene precursors. GC, glassy carbon electrode; PDDA, poly(diallyldimethylamonium) (reprinted from [1]).

There are various methods reported in the literature of the synthesis of pristine graphene monolayer and its derivatives such as GO, rGO and porous-reduced graphene oxide (prGO).[44-46] Relatively small flakes of graphene monolayer can be mechanically exfoliated from the graphite.[47] The dry mechanical exfoliation method suffers from being inefficient and does not allow to obtain large scale graphene flakes needed for the biosensing purposes. Large area single and few layer high-quality graphene nanosheets can be produced by chemical vapor deposition (CVD) methods on copper foil and are commercially available. The high quality of CVD graphene and the possibility of obtaining monolayer modified interfaces makes such electrodes advantageous for GFETs electrical biosensing. On the other hand, the solution-based exfoliation weakens the van der Waals forces between the graphene layers in graphite and allows to obtain rGO and GO flakes in an easy and efficient manner on a large scale.[48] This is the most cost-effective and commonly used synthetic approach for the construction of graphene-modified interfaces. In addition, the size of the sheets, the chemical composition and the morphology can be modulated improving, in general, the electrical properties of the material. Along with these advantages, GO has hydrophilic nature and a stable aqueous colloidal suspension can be obtained for transferring GO flakes onto the electrode substrate. The main drawback of graphene derivatives is that they usually require reduction step to restore the properties close to the pristine graphene. Because of advantages mentioned above, we opted in this work to use GO as a starting graphene material to obtain stable and scalable graphene-based electrodes *via* electrophoretic deposition and drop-casting following the chemical reduction on gain graphene's conductivity.

Depending on the preparation method, GO with C/O ratio of 4:1–2:1, is typically produced, being the most common the one proposed by Hummers and Offeman.[49] After the reduction, the C/O ratio can be improved to approximately 12:1 in most cases.[50] The reduction is needed to reduces the oxygen functional groups (usually hydroxyls, epoxides, carbonyls, carboxylic acids, quinones and lactones) and gain the properties close to the bare graphene.[50] In order to gain the conductivity for GO, various reduction techniques have been proposed: chemical (hydrazine,[51] ascorbic acid,[52] $NaBH_4$[53] etc.), thermal annealing,[54] electrochemical reduction[55] or a combination of several reduction techniques. The most commonly used and efficient GO to rGO reduction using hydrazine vapor is reported by Stankovich et al.,[56] giving a highly reduced GO with C/O ratio = 10.3. The C/O ratio is usually obtained through X-ray photoelectron spectrometry (XPS) analysis. In this work we used the combination of chemical reduction using the hydrazine vapor and consequent annealing as these methods provide the deepest reduction in a simple and reliable way.

Graphene transfer is an important step in the biosensor development process. Different techniques such as drop-casting,[57] spin-coating,[58] electrostatic interaction between positively charged interfaces and the negatively charged GO/rGO nanosheets,[59-60] electrophoretic deposition (EPD)[61] can be employed to coat electrical as well as inert surfaces with the chemically derived graphene materials.[1] Aiming to obtain the most homogeneous surface covered with a graphene monolayer, CVD graphene sheet can be easily transferred to any solid transducer interface using wet-transfer technique.[62] The choice of graphene deposition technique primarily depends on the detection technique used. For the advanced electronics such as graphene field-effect transistors it is essential to use high-quality graphene monolayers as the properties of the device are strongly depended on the graphene's quality, substrate and numbers of layers.[63-64] Hence, we decided to use GO dropcasting and CVD graphene to produce these kind of devices. For the classical planar gold electrodes where the number of layer and the surface morphology is beside the performance question, the use of EPD is preferred as this allows homogeneously cover the interface with the graphene material.

Graphene-based interfaces are characterized by means of imaging (SEM, AFM and optically), spectroscopy (Raman and XPS), electrically (FET and resistance measurements) and electrochemically (CV, DPV etc.). While spectroscopic and imaging techniques provide the information about the morphology and chemical composition of the interfaces, the electrical and electrochemical methods allow to obtain biosensing analytical response converting a surface bio-event into a measurable signal.

1.3. Functionalization of graphene and surface chemistry

Generally, the chemical functionalization can be realized through either covalent bonding or non-covalent interactions. The covalent bonding is usually achieved *via* few techniques such as diazonium electrografting[65-66] or a reaction with the remaining oxygen-containing functional groups in the graphene structure (**Figure 1.7a, c**).[67] In contrast to covalent graphene surface modification where carbon usually changes its hybridization state from sp^2 to sp^3, non-covalent strategies are versatile and do not affect significantly graphene's natural structure thereby preserving initial properties. The non-covalent interactions are relatively weak compared with covalent once. There are different non-covalent techniques to modify graphene, that employ van der Waals force,[68] electrostatic interactions,[69] hydrogen bonding[70] and π-π stacking.[71] These interactions are generally easy to achieve on a large surface required preserving the graphene electrical properties. On the other hand, the covalent modification is more controllable and robust providing the strong and stable binding of target molecules to the graphene lattice.

Electrostatic interactions can be utilized as a convenient technique for the preparation of graphene composite materials. Different GO/rGO composites were prepared based on negatively charged graphene substrate and positively charged anchoring materials such as polyethyleneimine (PEI) (**Figure 1.7a**).[67] The mixture of GO/PEI (1:1, $\zeta = 40.3 \pm 2$ mV) allows graphene deposition on a conductive interface in a cathodic EPD configuration.[6] In addition, while graphene exhibits excellent properties, the presence of abundant $-NH_2$ groups on PEI offers various opportunities for the further sensor's surface functionalization.[19]

π–π stacking interactions usually occur between two relatively large non-polar aromatic rings having overlapping π orbitals.[43] This type of linkage provides superior bonding strength compared to the other non-covalent interactions. π–π stacking benefits form not disrupting the conjugation of sp^2 graphene structure and hence preserves the electrical properties of graphene (**Figure 1.7b**).[72-73] Among the myriads aromatic compounds, pyrene-based compounds are the most widely used molecules for the graphene surface modification. Pyrene is a π-orbital-rich group that easily forms strong π–π stacking interactions with other polyaromatic materials such as graphene. A large number of small aromatic molecules such as pentacene,[74] 1-pyrenebutyric acid (PBA),[26] 1-pyrenebutyric acid n-hydroxysuccinimide ester (PBASE)[75] and dopamine[6] have also been attached previously onto graphene sheets using the π–π stacking approach.

Covalent modification of graphene benefits from the stronger bonding formed between the graphene and the ligand.[76-78] However, it is usually uneasy to directly implement the covalent modification as ideal graphene lacks functional groups that can be conjugated with.[79] In case of rGO obtained from the reduction of GO, incomplete reduction process leaves traces of oxygen-containing functionalities that are then available for further modifications.[43] Liu et al. have successfully covalently modified rGO with amino-polyethylene glycol (PEG) using carboxyl or hydroxyl groups present on the edges of rGO to enhance colloidal stability for the improved performance of graphene-based materials for safe and efficient intracellular delivery by laser-induced photoporation (**Figure 1.7a**).[67]

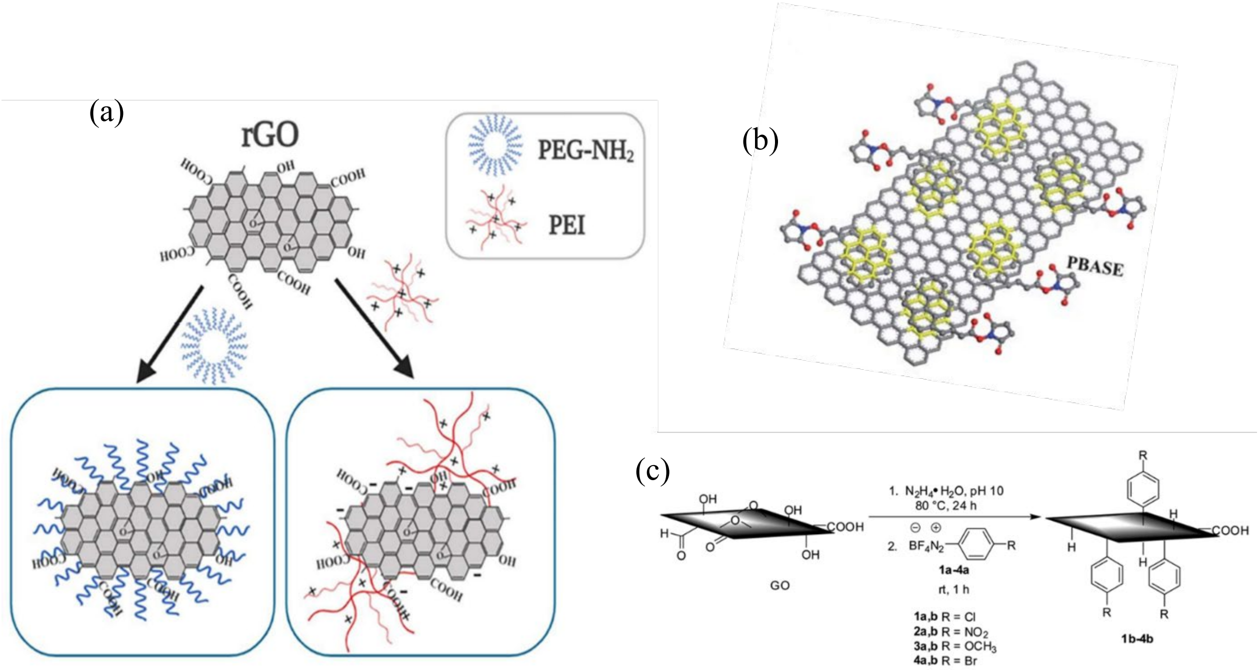

Figure 1.7: Graphene modification strategies: (a) Schematic representation of the modification of rGO where amino-polyethylene glycol (PEG) is covalently coupled to carboxyl or hydroxyl groups present on rGO and polyethyleneimine (PEI) is electrostatically adsorbed to rGO. “+” and “–” stand for positive and negative charge, respectively (adapted from [67]); (b) Noncovalent interactions between 1-pyrenebutyric acid n-hydroxysuccinimide ester (PBASE) and graphene through π–π stacking (adapted from [75]); (c) Covalent functionalization of graphene basal plane using diazonium salts reduction (adapted from [66]).

Other covalent modification strategies typically involve further disruption of the conjugation of the graphene sheets. Aryl diazonium salt molecules with varied functionalities have been successfully employed to modify carbon materials (e.g. GO,[66] CVD graphene[80] and glassy carbon[81]) *via* C–C covalent bond formation. The attachment of aryl diazonium salts can be conducted under mild conditions by either simple agitation or electrochemical reduction adsorption and it usually proceeds accompanied by the loss of N_2 (**Figure 1.7c**).[82] Functionalization of graphene using aryl diazonium salt molecules through electrochemistry offers several advantages: the reaction can be completed in a fast (in a few seconds) and self-terminated manner usually in one electrochemical cycle and monitored by means of cyclic voltammetry.[83] Leroux et al. modified a classy carbon electrode with triisopropylsilyl (TIPS)-protected ethynyl aryldiazonium salt which avoids the formation of multilayers and efficiently protects the functional group during the electrografting step.[81] After TIPS deprotection, a dense reactive ethynyl aryl monolayer is obtained which paves the way for “click” chemistry reaction.[65] Although covalent modification of graphene alters some of its natural properties,[84-86] this method is still valuable in the biosensing field when graphene's interface stability and close probe vicinity are desirable.

As described above, the chemical functionalization is essential step to achieve selective and sensitive biosensing on graphene interface. It is important to highlight that the surface chemistry also plays a critical role in passivating the surface of graphene against non-specific interactions and false positive response when complex biological samples are analyzed. Indeed, aromatic amino-acid residues (such as histidine, phenylalanine, tyrosine, and tryptophan) found in peptides and proteins can adsorb to the highly hydrophobic graphene surface through non-covalent interactions.[87-88] He et al. have demonstrated a simple post-adsorption of human serum: bovine serum albumin (HS: BSA) mixtures onto the graphene modified sensor resulted in a highly anti-fouling interface, while keeping the sensing capabilities for folate biomarkers.[89] The mixture of HS: BSA physically absorbs on unmodified graphene sites passivating them for the target analyte. Aspermair et al. showed that pre-conjugated pyrene-PEG units (PyPEG) in a ratio of 1:10 with the aptamer probe provides not only the optimal anti-fouling character to rGO transistor but also beneficial as a spacer molecule providing a good sensing sensitivity to the target HPV-16 E7 protein.[26]

1.4. Electrical and electrochemical detection techniques

Electrical and electrochemical biosensors transduce surface biological events such as protein-receptor binding or surface charge redistribution into a measurable electrical signal. The electrochemical detection usually implies the use of an electrochemical probe (e.g. ferrocene methanol, ferro/ferricyanide, ruthenium hexamine or other redox couples) which is able to change its oxidation state by exchanging electrons with the surface of electrode. The applied potential on the working electrode induces the electrochemical reaction and the number of electrons transferred (i.e. electrical current) provides the information about the surface state. The unmodified conductive interfaces are generally demonstrating high electron transfer kinetics giving a high current density when the electrochemical reaction occurs. When the large biological molecules are attached to the interface, the electron transfer kinetics decreases diminishing the measured current in return. The change in current is proportional to the number of molecules adsorbed on the surface providing the biosensing information. The electrochemical biosensors take advantages from being label free, independent of ionic strength of the medium and widely used and commercialized due to its point-of-care (PoC) application potential.

In an electrochemical biosensing system, three electrodes configuration is commonly used. A typical electrochemical cell consists of working, counter, and reference electrodes (**Figure 1.8a**). The working electrode acts as the transducer in the bioelectrochemical or biochemical reaction, whereas the counter electrode (usually made of Pt) immersed into the electrolyte solution controls the possibility of applying currents to the working electrode. The potential applied to the working electrode is usually referenced against the silver/silver chloride (Ag/AgCl) electrode. The advances made in microtechnology and bioelectronics have made it possible to miniaturize and

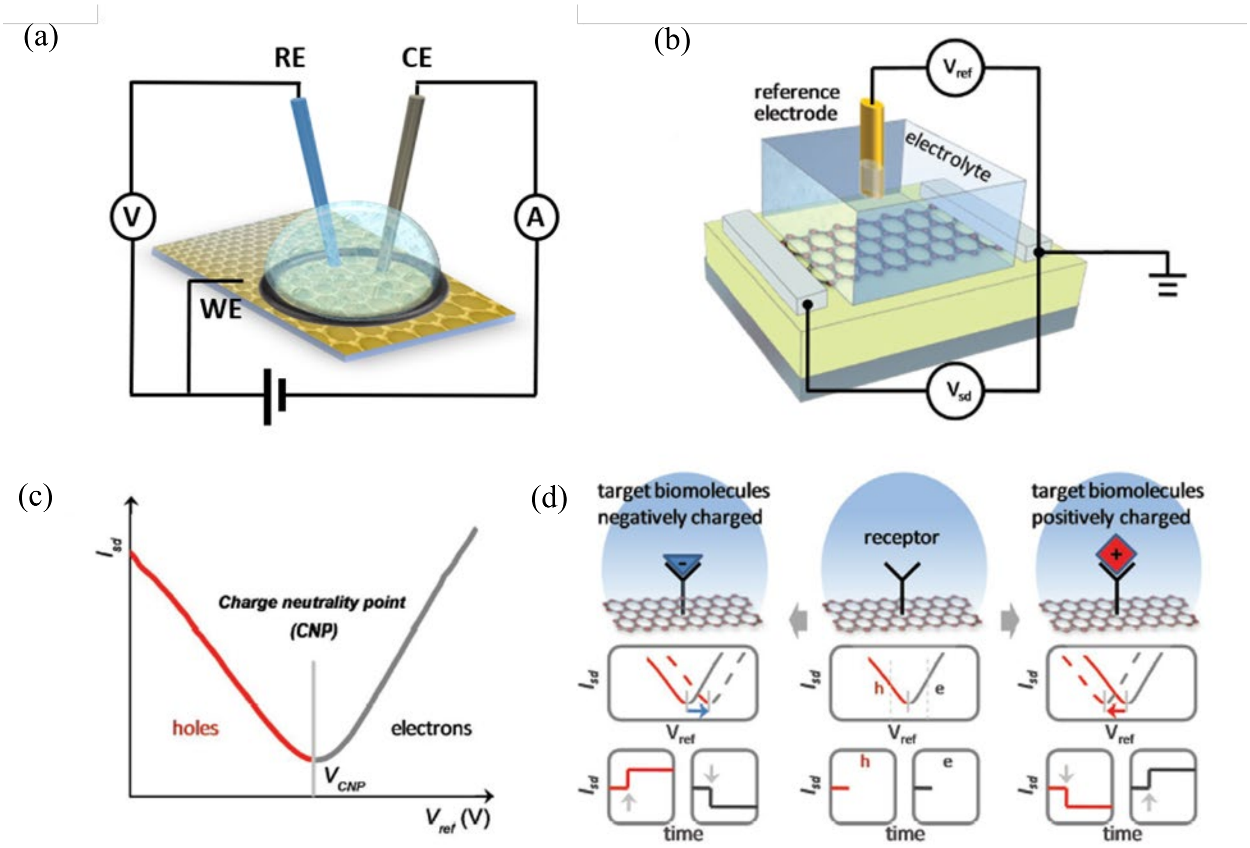

Figure 1.8: Electrochemical and electrical detection techniques in biosensor applications: (a) schematic of a classical three electrodes electrochemical setup with graphene interface acting as a working electrode; (b) schematic of a liquid-gated GFET biosensor; (c) typical ambipolar transfer characteristics showing that the type of carriers in graphene can continuously be modulated from holes (on the left, in red) to electrons (on the right, in gray) using the field effect. The charge-neutrality point (CNP) co-called Dirac point is located at the transition between the electron and hole regime, where the current is minimized; (d) in the upper central figure is a receptor molecule immobilized on the graphene surface. The plots of I_{DS} versus V_G and I_{DS} versus the time t are shown in the middle and lower panels, respectively. The abbreviation 'h' in red refers a measurement carried in the hole regime and 'e' for the electron regime in gray. Upon the binding of a charged biomolecule (as indicated by the arrows), the field effect resulting from the binding of positively or negatively charged target biomolecule on the receptor causes a shift of CNP and consequently yields the analytical response in I_{DS} versus the time t (adapted from [42]).

integrate the electrodes in a single device. The electrochemical devices and integrated all-in-one electrodes benefit from the possibility for making portable instruments at relatively low costs.

The vast variety of ways in which potential may be changed leads to different types of voltammetric methods used in the biosensing field, such as linear swipe voltammetry (LSV),[90] square wave voltammetry (SWV),[91] differential pulse voltammetry (DPV)[92] and cyclic voltammetry (CV).[93] The last two are of the most common methods used to obtain useful information on redox potentials and to investigate the mechanisms and kinetic parameters (e.g. electrochemical rate constant,[94] electrochemical active surface area,[95] number of redox species linked to the surface[96-97]) involved in the reactions with electroactive species.

Field-effect transistor (FET) is a kind of electrochemical device that uses an electric field to control the electrical behavior and the resistance of a channel between two electrodes in semiconductor materials.[98] There have been already reported different types of field-effect transistors in the biosensing field such as carbon nanotubes[99] and silicon nanowires.[100] Although these devices have been used as transducers for biosensing of the enzyme Cathepsin E[101] and a complimentary DNA detection,[102] they suffer from very limited surface area for bioreceptor immobilization and the current detection signal corresponds to nanoamps making the readout challenging. In contrast, graphene-based interfaces offer one-atom thick large surface area interfaced where bioreceptor loading is higher and the current read-out is usually in microamps range. The graphene-based liquid-gated FET (GFET) consists of a source and a drain electrodes connected with a graphene material with the gate electrode separated from the source and the gate by ionic liquid (**Figure 1.8b**).[42] In this configuration, the current path between the source and the drain is called the graphene channel. The device behaves as an on/off switch by changing the gate-to-source bias with a negligibly low leakage current between them. GFET demonstrates ambipolar nature in $I_{DS}V_G$ characteristic due to the charge motion in the graphene channel: electrons as the negative carrier for the n-type channel for high gate voltages (on the right) and the holes as the positive carrier for the p-type channel for low gate voltages (on the left) (**Figure 1.8c**). The charge-neutrality point (CNP) co-called Dirac point is located at the transition between the electron and hole regime, where the current is minimized. Changes in the electric field potential at the gate electrode and at the graphene surface are used in conjunction to modulate the source-drain current giving the information of surface charge redistribution events (**Figure 1.8d**).[97] The device is integrated into a microfluidic cell where the continuous flow introduces an analyte to the interface. Taking a receptor-modified graphene interfaces as a reference, the binding process of a negatively or positively charged analyte will cause a local change in the electric field close to the GFET surface changing the $I_{DS}V_G$ characteristics. In the time dependent measurement, the current I_{DS} is monitored at a fixed reference potential V_G. The binding/unbinding of a target molecule provides the information about the analyte concentration proportional to the current change induced but also allows to obtain kinetics of the reaction without using labeled molecules and external redox probe. This current and its modulation in the graphene channel can be expressed as a function of the change in the carrier density Δn, which is induced by and is proportional to the total number N of charged biomolecules adsorbing on the graphene surface:[42, 103]

$$I_{SD} = \mu\ C_i \frac{W}{L} (V_G - V_T)\ V_{SD} \qquad Equation\ 1.5$$

$$\Delta I_{SD} = \frac{W}{L}\ V_{SD}\ e\ \mu\ \Delta n\ \propto N \qquad Equation\ 1.6$$

where μ the carrier mobility; V_G, V_{SD} and V_T the gate, the source-drain and threshold voltages respectively; W and L are the width and length of the graphene channel respectively; C_i the gate capacitance and e is the electron charge. However, the quantitative monitoring of biomolecules in not always linear and straightforward. The sensing current also depends on many factors such as the change in the shape of $I_{DS}V_G$ characteristics, the number of charges each biomolecules carry, ionic strength of the medium, the surface chemistry functionalization. [80, 104-106] In the **Equation 1.6** it is approximated that graphene has a constant carrier mobility μ upon the adsorption of biomolecules. This is correct in most cases where the adsorbed biomolecules bind to the receptors and interact weakly with the graphene lattice. However, the molecules that directly bind on a graphene surface or the influence of the ionic strength resulting in a change of $I_{DS}V_G$ curve.[105, 107]

In order to evaluate and compare the resulting device performance with different graphene sources and fabrication methods, an intrinsic parameter, the mobility μ of the material can be calculated. It can be expressed as:

$$\mu_{eff} = \frac{dI_{DS}}{dV_G} \frac{L}{W\ V_{DS}\ C_i} \qquad Equation\ 1.7$$

where dV_{DS}/dV_G is the slope from the linear fit, L and W the channel length and width, respectively, V_{DS} the applied drain-source voltage and C_i the gate capacitance.[108] The mobility values vary a lot in different sources in the literature, some of them reaching the values as high as 200,000 $cm^2\ V^{-1}\ s^{-1}$,[109] but it strongly depends on many parameters such as graphene material type and quality, substrate, experimental conditions, dopants etc.

Chapter 2: Electrochemical biosensors based on reduced graphene oxide

2.1. Introduction

Accurate analysis of the presence of disease-specific biomarkers in biological fluids remains of great importance in clinical settings and electrical and electrochemical sensors can reach that goal by converting a chemical or a biological response into a processable and quantifiable electrical signal. Highly reduced graphene oxide has generated great expectations as a transducing platform in biosensing, due to its high surface area accompanied by biocompatibility, electrical conductivity and fast charge transfer kinetics. Along with these unique properties, reduced graphene oxide takes advantage of being cost-effective and simple to manipulate material giving the functionalities close to the pristine graphene.

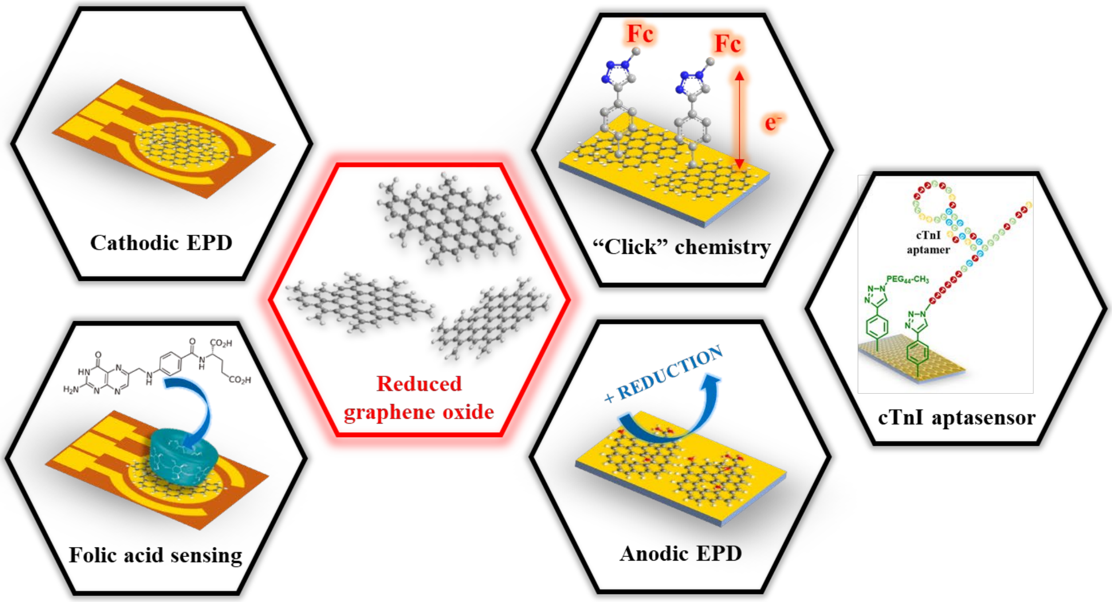

Figure 2.1: Electrochemical sensor development using reduced graphene oxide: Cathodic and anodic electrophoretic deposition approaches, "click" chemistry to link surface receptors, sensing of folic and cTnI biomarker on the obtained interfaces.

A mandatory step in the production of graphene-based electrochemical biosensors is the graphene transfer technology with the consequent modification of the interface with biorecognition elements and antifouling agents. In this chapter, the development of electrochemical sensing platforms where the working electrode in an integrated system can be selectively modified with rGO will be presented and the results discussed (**Figure 2.1)**.

Indeed, such integrated electrode systems play an essential role in determining the device performance, which requires to conserve all functionalities of a classical electrochemical cell along with emerging new properties such as light-weight and conformable for flexible and wearable applications. This can be notably achieved electrophoretic deposition (EPD). In this chapter, the process was first optimized on planer gold electrodes and then later applied to a home-made integrated system on Kapton. After a full characterization of the electrochemical system, surface modification approaches will be discussed, notably in the light of folic acid (FA) sensing as the analyte is eliminated by the human body and regular intake and control are indispensable. The deficiency in FA may cause a number of health problems such as anemia, neural tube defects and malformation of the fetus during pregnancy. On the other hand, the excess of FA may mask vitamin B_{12} deficiency symptoms. The normal FA levels are between 4 and 45 nM which defines the target sensing range of the device.

Furthermore, we validate the possibility of controlled covalent functionalization of rGO interfaces based on the electroreduction of the triisopropylsilyl-protected ethynyl diazonium salt.[65, 81] Using a protection–deprotection technique, the immobilization of a functional monolayer which can be further functionalized by Cu(I) catalyzed “click” chemistry will be demonstrated. The surface chemistry results in a densely packed ferrocenenyl monolayer which can be efficiently integrated on these rGO-modified surfaces with the outlook for sensing-related applications.

Such closely packed interfaces were used for biodetection of cardiac biomarker troponin I (cTnI) *via* linking the specific aptamer to the interface. The biomarker detection on an early onset with a higher risk of acute myocardial infarction (AMI) can reduce the risk from death from heart attack. The sensor is required to differentiate patients with myocardial ischemia onset and healthy individuals which corresponds to 1.05 pM (26 pg mL^{-1}) of cTnI in serum. The level of cTnI of patients in risk is usually 100-1000 times higher with a clear positive test for AMI, corresponding to serum levels of cTnI in the 202-2020 pM (5-50 ng mL^{-1}). Therefore, we opted to develop an electrochemical label-free aptasensor for cTnI biomarker which could differentiate the samples in this concentration range.

2.2. Electrophoretic deposition of graphene oxide and reduction on planar gold electrodes

Electrophoretic deposition of reduced graphene oxide is a simple and cost-effective technology for depositing graphene material onto the electrode surface based on electrostatic attraction between negatively charged surface of cathode and positively charged composites of rGO flakes from the colloidal solution. Along with the controlled deposition thickness, EPD would be the preferential approach, as it allows the simultaneous deposition and partial reduction of oxygen-containing groups. rGO sheet carry net negative charge due to the numerous oxygen-containing groups still present in their structure despite the reduction used. This is one of the reasons why rGO is often charged with a cationic polymer (e.g., polyethyleneimine) or metallic cations (Ni^{2+}, Cu^{2+}, etc.) to achieve a positively charged graphene nanomaterial, which can be deposited by cathodic EPD. This is an interesting approach to directly deposit rGO on a conductive surface *via* EPD process without any further reduction step.

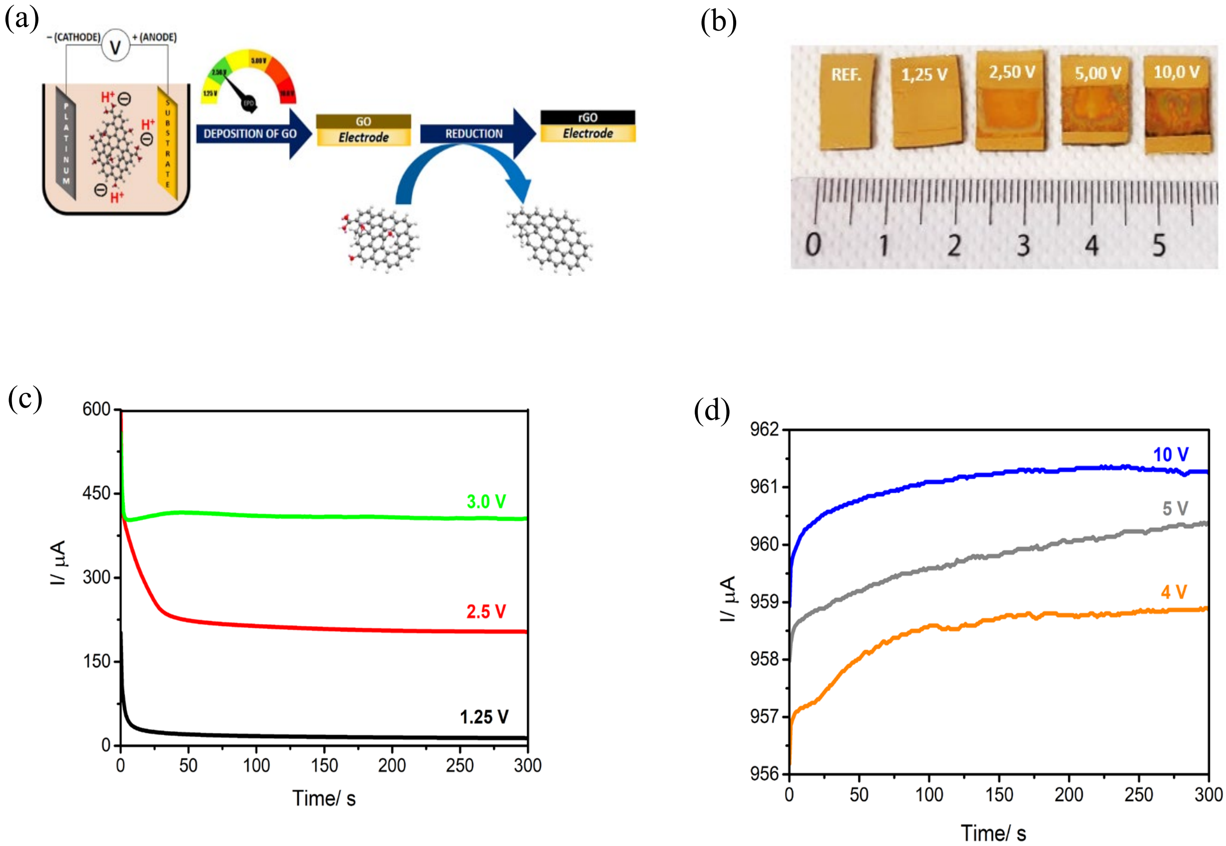

Figure 2.2: Electrophoretic deposition of GO: (a) Schematic illustration of the formation of an electrochemically rGO thin film by anodic EPD from an aqueous graphene oxide suspensions (GO, 1 mg mL^{-1}) at a potential bias from 1.25 V to 10V for 5 min, followed by chemical treatment in hydrazine vapor; (b) Optical images of gold thin film electrodes before (0.00 V) and after anodic EPD (without reduction) for 5 min at 1.25, 2.50, 5.00 and 10.00 V; Change of current as a function of deposition time using different applied potentials: (c) low potentials 1.25, 2.50 and 3.00V, (d) high potentials 4, 5 and 10V.

The other approach is based in anodic deposition followed by thermal and/or chemical reductions to restore more complete the aromatic network in order to obtain a material with good electron transfer properties. The presence of carboxyl and hydroxyl functions on GO results in an overall negatively charged material of about −41.3 ± 0.8 mV for aqueous GO suspensions The anodic EPD process with the consequent reduction is demonstrated in **Figure 2.2a** and used in this work. The deposition took place in a two-electrode system with a platinum foil as the cathode and the cleaned gold surface as the anode. An aqueous GO solution of 1 mg mL^{-1} was used for the EPD. Voltage biases of 1.25 V, 2.5 V, 5 V or 10 V were applied for 5 min. Due to the negatively charged nature of GO, cathodic EPD of GO results in GO films with an extremely low deposition rates and a low degree of reduction during the deposition process. The interfaces obtained at different potentials are shown in **Figure 2.2b**. After the deposition, the modified electrodes were chemically reduced in hydrazine vapor at 80 ºC during 4 h. The interfaces were washed with water and dried under the nitrogen flow.

For EPD at voltages lower than 3 V, the electrical current decreases during the deposition time due to the insulating nature of GO (**Figure 2.2c**). The decrease of current is then stabilized indicating the termination of the process as well as the system is reached equilibrium under given conditions. The current drop at 2.5 V is slower than that at 1.25 V. The reason for this is not well understood, but could be due to a partial electrochemical reduction of GO under these conditions. In contrast to low voltages deposition, the EPD bias greater than 5 V induces not only the graphene deposition, but an electrochemical reaction, delaying the passivation (**Figure 2.2d**). Along with the current increase, the formation of bubbles was observed during the process, suggesting that water electrolysis occurs along with the GO film formation. As a result, it is shown that the use of a voltage bias of 2.5 V for 5 min results in GO thin films of good electrochemical behavior. These films can also be submitted to further reduction and surface modification using diazonium electrochemistry without altering their adhesion characteristics.

Scanning electron and atomic force microscopies were used to demonstrate the morphology of the obtained surfaces (**Figure 2.3a-b**). Furthermore, XPS and Raman analysis were applied to reveal the chemical composition of the graphene modified electrodes (**Figure 2.3c-d**).

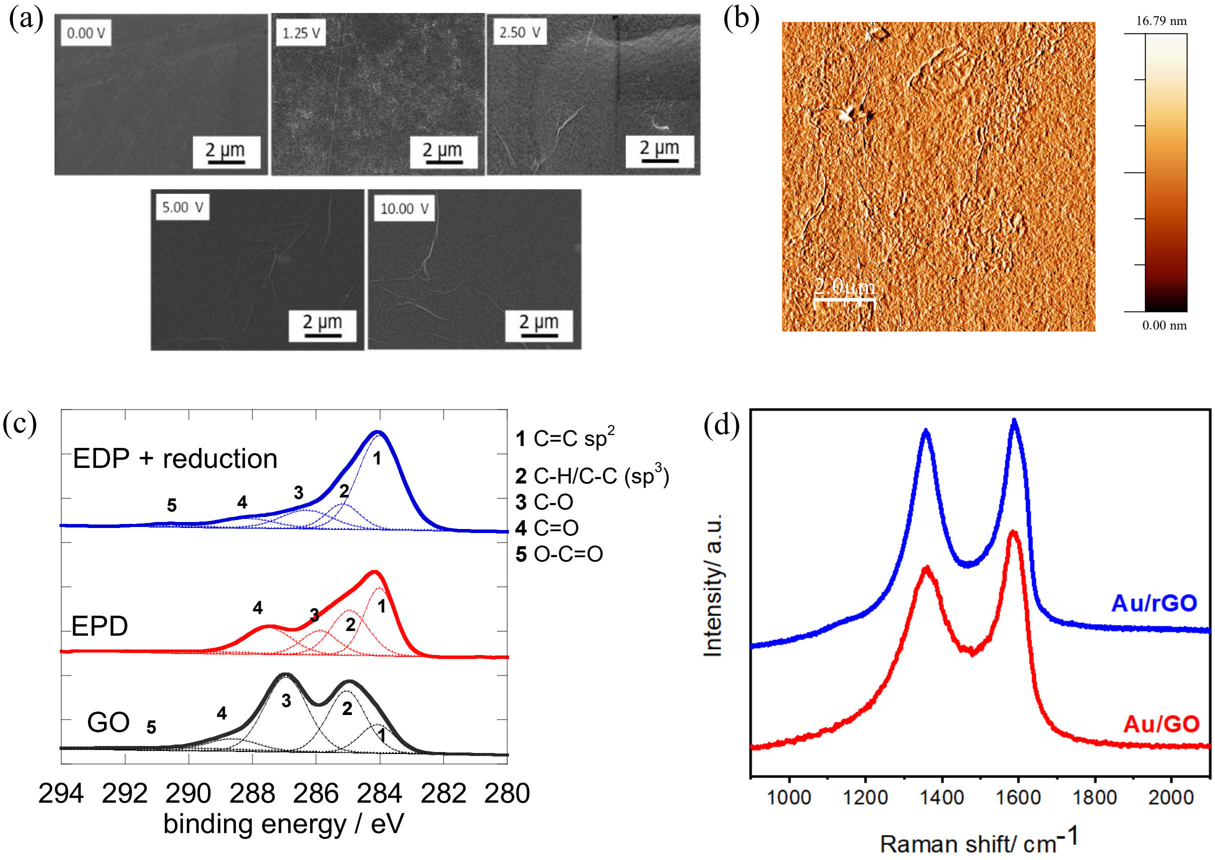

Figure 2.3: Surface characterization of electrophoretically obtained rGO films: (a) SEM images of gold covered electrodes before and after EPD from an aqueous graphene oxide suspension (GO, 1 mg mL^{-1}) at different potential biases for 5 min; (b) AFM image of the interface obtained at 2.5 V EPD process after the hydrazine reduction; (c) C_{1s} high-resolution XPS spectra of initial GO (black), EPD GO (red) and rGO interface (blue); (d) Raman spectra of the EPD film formed at 2.5 V before (red) and after hydrazine reduction (blue).

Surface inspection on Au/rGO interfaces by SEM reveals that the roughness and the quality of the deposited films depend on the deposition voltage (**Figure 2.3a**). The deposition at 1.25 V produces the interface with a poor coverage by granular-like material. The rGO film produced at 2.5 V has homogeneous, smooth and completely covered by rGO surface. Some wrinkles of the graphene layer are observed, which is typical for this material. For the higher voltages, the surface morphology is similar to the one at 2.5 V, except some macro discontinuities and material detachments (not shown) were observed due to excessive deposition and water electrolysis.

The AFM image was obtained for 2.5 V deposition interface after the reduction as this voltage demonstrates the best quality interface (**Figure 2.3b**). The interface has 3.5 nm average surface roughness compared to 4.1 nm for the bare gold electrodes. Considering the average GO flake size 10 µm, the obtained roughness value suggests that the graphene flakes are stuck on the surface and oriented in parallel to the gold electrode surface.

The chemical composition of the interfaces before and after reduction were evaluated using XPS analysis and compared to the XPS spectrum of the bulk GO material (**Figure 2.3c**). The high resolution C_{1s} core level spectrum of the initial GO suspensions showed contributions at 284.2 (C=C sp^2), 285.0 (C–H/C–Csp^3), 286.7 (C–O) 288.7 (C=O) and a small contribution at 291.0 (O–C=O). The C_{1s} XPS core spectra of GO-coated gold interfaces showed similar contributions with different intensities. Particularly, the band at 284.2 eV due to C=C sp^2 increased compared to the GO solution, indicating the partial restoration of the sp^2 lattice of the deposited graphene material. The XPS of GO-coated gold showed additional bands at 285.0 and 286.7 eV with a large band at 288.0 eV due to C=O. The hydrazine reduction of the GO–gold interfaces resulted in a significant decrease of the epoxy/ether functions at 286.7 eV, in accordance with a partial reduction of GO mostly likely due to the elimination of CO by a Kolb-like mechanism. The ketone groups remained preserved.

The Raman spectra of the GO interfaces before and after hydrazine treatment are shown in **Figure 2.3d**. There are two main bands at 1593 and 1340 cm^{-1} related to G and D peaks respectively. The D/G ratio has increased from 0.86 to 0.97 after the hydrazine chemical reduction.

2.3. Covalent modification of reduced graphene oxide surface by the aryldiazonium salt

To validate the possibility of controlled covalent functionalization, efficient modification based on the electroreduction of a triisopropylsilyl-protected ethynyl diazonium salt was performed (**Figure 2.4a**). Covalent surface modification of graphene-based materials using the electroreduction of aryldiazonium salts is a popular approach as it allows the introduction of different chemical groups. The major drawback of this approach is the difficulty to control the extent of the reaction—notably, to limit the reaction to the formation of a functional monolayer. The highly reactive nature of the formed aryl radical results in the formation of disordered polyaryl multilayers, which in the case of a sensor might limit the dynamic range of sensing. The introduction of bulky substitutions on the ArN_2^+ moieties limits radical addition reactions and allows the formation of ultrathin functional monolayers. On the basis of this concept, the precursor 4-((triisopropylsilyl)ethylenyl)benzenediazonium tetrafluoroborate (TIPS-Eth-ArN_2^+) was used for the formation of an organic thin film on anodic EPD formed Au/rGO interfaces.

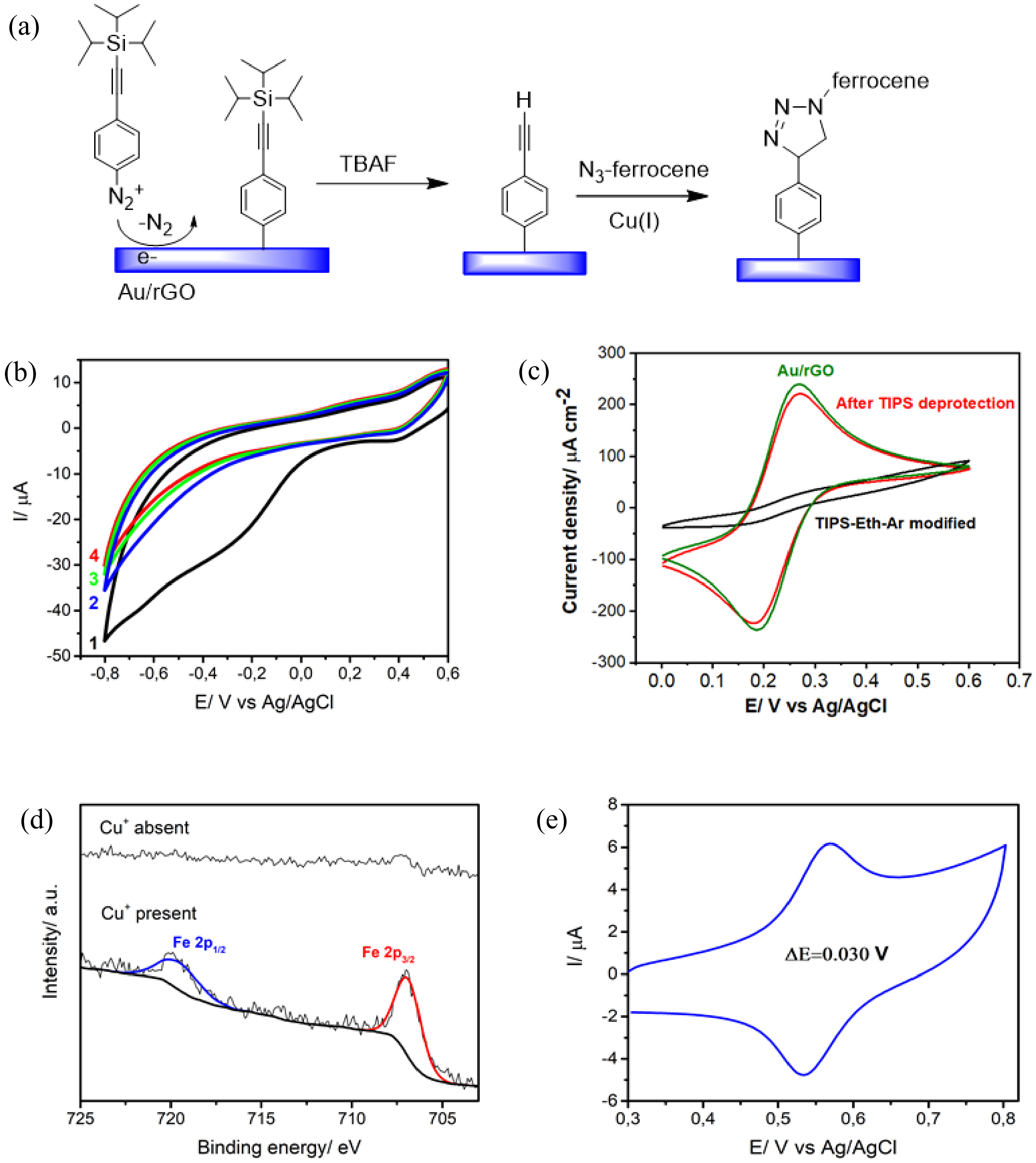

Figure 2.4: Electrochemical grafting of rGO with TIPS and "click" chemistry of ferrocene azide: (a) covalent grafting of EPD rGO electrodes by a silyl-protected diazonium salt followed by tetrabutylammonium fluoride (TBAF)-based deprotection and 1,3-dipolar cycloaddition reaction using azidomethylferrocene as a model compound; (b) electrical reduction of 4-((triisopropylsilyl) ethylenyl)benzenediazonium tetrafluoroborate (TIPS-Eth-ArN_2^+) with simultaneous rGO surface grafting using cyclic voltammetry from 0.6 to -0.8 V vs Ag/AgCl, scan rate 50 mV s^{-1}; (c) cyclic voltammograms in 1 mM ferrocenemethanol in 1xPBS of the Au/rGO interfaces before (green), after diazonium treatment (black) and after the cleavage of the protective group using TBAF (red), scan rate 100 mV s^{-1}; (d) high-resolution Fe_{2p} XPS core-level spectra of ferrocene modified Au/rGO surfaces with and without Cu(I) catalyst during the "click" chemistry reaction; (d) cyclic voltammogram of Au/rGO/Ferrocene modified electrode in acetonitrile/ NBu_4PF_6 (0.1 M), scan rate 100 mV s^{-1}.

The layer was obtained by potential cycling in 10mM solution containing TIPS-Eth-ArN$_2^+$ in 0.1M TBAPF$_6$ (**Figure 2.4b**). As observed by cyclic voltammetry, the reduction peak of TIPS-Eth-ArN$_2^+$ at −0.2 V decreased rapidly after five cycles, indicating the blocking of the Au/rGO electrode. The blocking properties of the layer was further investigated by recording the cyclic voltammogram of 1 mM ferrocenemethanol in 1xPBS before and after the electrografting process and was found to be typical of a totally blocked electrode. In order to have the access to the acetylene function, the sample was submersed in 0.05M solution of tetrabutylammonium fluoride (TBAF) in tetrahydrofuran (THF) for 1 hour at ambient conditions. Then the surface was copiously washed in THF for 1 hour to remove the residues of TBAF. The success of the deprotection reaction was confirmed by cyclic voltammetry (**Figure 2.4c**). The deprotected interface gives almost the same signal as on Au/rGO interface.

Huisgen 1,3-dipolar cyclization ("click" chemistry reaction) with azidomethylferrocene was carried out on the deprotected interface using Cu(I) as a catalyst. The interface was immersed into an aqueous solution of CuSO$_4$ (10 mM) and L-ascorbic acid (20 mM) in the presence of azidomethylferrocene (0.83 mM in THF) and left for 1h under an argon atmosphere. The interface was then treated with an aqueous solution of 10 mM EDTA for 10 min to chelate any remaining Cu^{2+} residues and finally washed copiously with acetone and water and left to dry. From the presence of the Fe$_{2p}$ component in the XPS survey spectrum (**Figure 2.4d**) when the catalyst was added, the covalent linkage of the ferrocene derivative to the surface can be concluded. As a control experiment, when no Cu(I) ions were present, the Fe$_{2p}$ component in the XPS spectrum is not observed, indicating that no reaction took place.

In order to quantify the number of redox molecules bound to the surface, the cyclic voltammogram of the ferrocene-modified electrode was obtained in 0.1M TBAPF$_6$/CH$_3$CN solution (**Figure 2.4e**). A surface concentration of $\Gamma = 2.5\ 10^{-10}$ mol cm^{-2} of ferrocene molecules was found from the measurement using the **Equation 2.1:**

$$\boldsymbol{\Gamma} = \frac{\boldsymbol{Q}}{\boldsymbol{nFA}} \quad \textit{Equation 2.1}$$

where Q is the integral of the oxidation peak, n is the number of exchanged electrons (n = 1), F is the Faraday constant and A is the electroactive surface area of the electrode determined as 0.136 cm^2. Considering the ferrocene molecules as spheres with a diameter of 6.6 Å, the theoretical maximum coverage for a closely packed ferrocene monolayer can be estimated as $\Gamma = 4.4\ 10^{-10}$ mol cm^{-2}. In our case, about half of the full coverage was achieved.

2.4. cTnI electrochemical sensing

To perform biodetection of cTnI, directly correlating biomarker to Acute Myocardial Infarction (AMI), the mixture of 5’-N_3 terminated troponin-specific aptamer (5’-N_3-TTT-TTT-CGT GCA GTA CGC CAA CCT TTC TCA TGC GCT GCC CCT CTT A-3’) with azido-PEG$_{44}$-CH_3 chain acting as antifouling agent were linked to ethynyl-terminated interfaces using the same protocol as for azidomethylferrocene (**Figure 2.5**). We expect that the aptamer and the antifouling agents will interact with the modified graphene surface in a similar manner as the model compound containing ferrocene derivative.

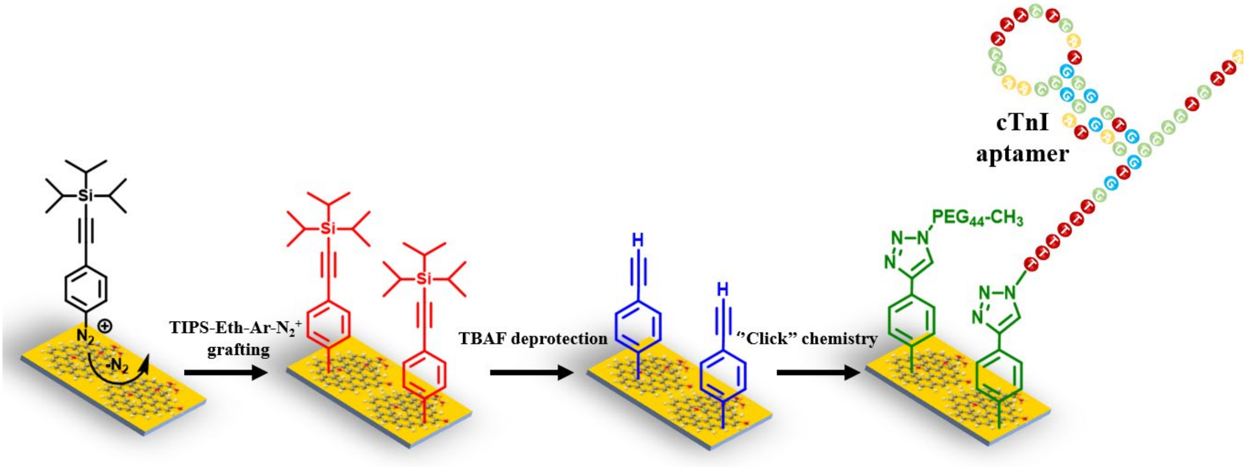

Figure 2.5: Development of cTnI electrical aptasensor on EDP rGO interfaces: covalent grafting of the electrodes by a silyl-protected diazonium salt followed by tetrabutylammonium fluoride (TBAF)-based deprotection and “click” chemistry reaction using 5’-N_3-terminated cTnI specific aptamer and azido-PEG$_{44}$-CH_3 chain.

To understand if such a controlled surface architecture allows cTnI sensing, DPV using ferrocenemethanol as redox mediator was applied for sensing the cTnI-aptamer interactions. The different concentrations of cTnI protein in 1xPBS buffer (0.001, 0.01, 0.1 1, 100 and 380 ng mL^{-1}) were incubated on the modified surface for 20 minutes to let the protein bind to the aptamer. Then the interface was washed with the buffer and the redox probe was introduced. When cTnI binds to the aptamer-modified electrode, a reduction in current (**Figure 2.6a**) was observed, as previously reported on other aptamer-functionalized interfaces.[41] To underline the specificity of this interaction, the change in electrochemical signal upon binding to BNP-32, another cardiac biomarker, was recorded at comparable concentrations (0.001, 0.01 and 0.1 ng mL^{-1}) under the identical conditions as for cTnI sensing. It can be observed in **Figure 2.6b** that the incubation of BNP-32 causes minor current change response proving the specificity of the interface.

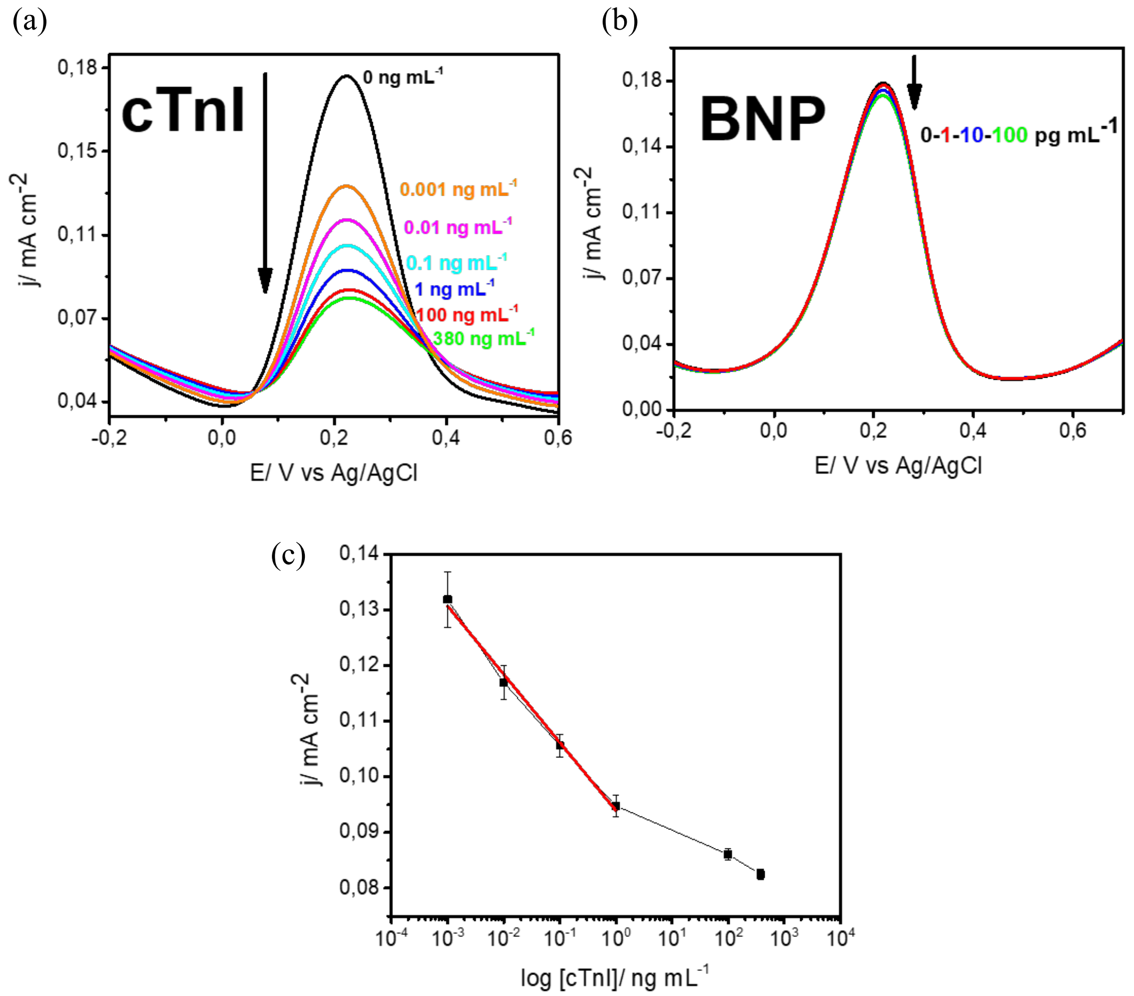

Figure 2.6: Electrical sensing of cTnI on EPD rGO covalently modified aptasensor: (a) differential pulse voltammograms recorded on rGO/aptamer interface using ferrocenemethanol as a redox probe for different cTnI concentrations (0.001, 0.01, 0.1, 1, 100 and 380 ng mL^{-1}) in 1× PBS (pH 7.4) after 20 min of incubation time; (b) differential pulse voltammograms of control experiment incubating different concentration of BNP-32 protein (0.001, 0.01 and 0.1 ng mL^{-1}). The conditions are identical to cTnI measurements. (c) current change as a logarithm of cTnI concentration extracted from Figure 2.6a. Linear range is indicated in red.

Tracing the current change as a function of cTnI concentration from **Figure 2.6a**, the linear range from 1 pg mL^{-1} to 1 ng mL^{-1} can be observed (slope: -0.0125; R^2=0.99) shown in **Figure 2.6c**. The current saturates for the high concentrations most likely due to the occupancy of all active site. Taking into account the troponin I level of healthy individuals as low as 26 pg mL^{-1} and the patients with a clear positive test for AMI, with serum levels of cTnI in the 5-50 ng mL^{-1}, it can be concluded that the obtained EPD rGO electrochemical aptasensor can specifically distinguish the concentrations of these two groups. Compared to other electrochemical aptasensors, the sensor sensitivity is in line with the one reported using N-prGO on GCE and more sensitive compared to others allowing to distinguish between the healthy individuals and the patients at risk (**Table 2.1**). Along with that, the sensor is very stable over the time due to the covalent chemistry applied and not sensitive to the ions present in the medium, which has great importance for the real biological samples.

Table 2.1: Compilation of electrochemical aptasensor performances for the detection of cTnI

Electrode architecture	**Method**	**Ligand attachement**	**LOD [pg mL^{-1}]**	**Linear range [ng mL^{-1}]**	**Ref.**
Au/ P1-P2-TdT/ apta	DPV	thiol	40	0.5–100	[110]
SPCE/ AuNPs/ TTCA/ apta	CA	NHS/EDC coupling	24	0.024–2.4	[111]
GCE/ MoS_2-apta	EIS	physisorption	22.8	0.24-24000	[112]
SPGE/MCH/DNA-NTH-apta/MMOF	DPV	thiol	16	0.05–100	[113]
Au/Au-ND/apta	DPV	thiol	8	0.05–500	[114]
Au/G-apta	**DPV**	**“click”**	**0.001**	**0.001-1**	**This work**
GCE/ N-prGO/ apta	DPV	π-π stacking	1	0.001-100	[115]
SPGE/ rGO-PEI-apta	DPV	π-π stacking	1	0.001-10	[116]

Apta: aptamer; CA: chronoamperometry; SPCE: screen-printed carbon electrode; SPGE: screen-printed gold electrode; TTCA: 5,2′:5′2″-terthiophene-3′-carboxylic acid; GCE: glassy carbon electrode; N-prGO: nitrogen-doped reduced graphene oxide; MCH: 6-Mercapto-1-hexanol; Au-ND: gold nanodumbbells; DNA-NTH: deoxyribonucleic acid nanotetrahedron; MMOF: magnetic metal organic framework; P1: 30-T CAT GCG GTT GGA AAG AG; P2: 50-CGC CAA CCT TTC TC-TTT-(CH2)6-SH; TdT: terminal deoxynucleotidyl transferase; MB-poly A: Methylene blue-AAA AAA AAA AAA; rGO: reduced graphene oxide; PEI: polyethylenimine; IDE: interdigitated electrodes.

2.5. Modification of gold working electrode in integrated electrochemical array with reduced graphene oxide

Being cost-effective and simple, the EPD process takes advantage over a drop-casting process due a very localized area where rGO should be deposited. The deposition occurs only on the area where an electrical potential is applied. In our case, only working electrode in an integrated system should modified with the graphene material, while the counter and reference electrodes have to remain intact. Additionally, chemical reduction is not compatible with the most of organic substrates (such as Kapton) due to its aggressive nature which damages the substrate. In order to overcome the limitation, cathodic EPD was used on the integrated electrodes as this approach allows direct deposition of rGO onto the surface without any further treatment of the interface.

The integrated electrodes system consists of three electrodes: 1 mm in diameter round working electrode placed in the center and two side electrodes (reference and counter) spaced 0.1 mm from the working electrode. The design is adjusted to perform classical electrochemical measurements such as chronoamperometry (for EPD) and differential pulse voltammetry as a detection technique. The polyimide substrate was used a substrate material due to its high dielectric constant, flexibility and chemical inertness. The electrodes are made of gold as a classical metal for electrochemistry purposes. The process has five main steps and depicted in the **Figure 2.7a.**

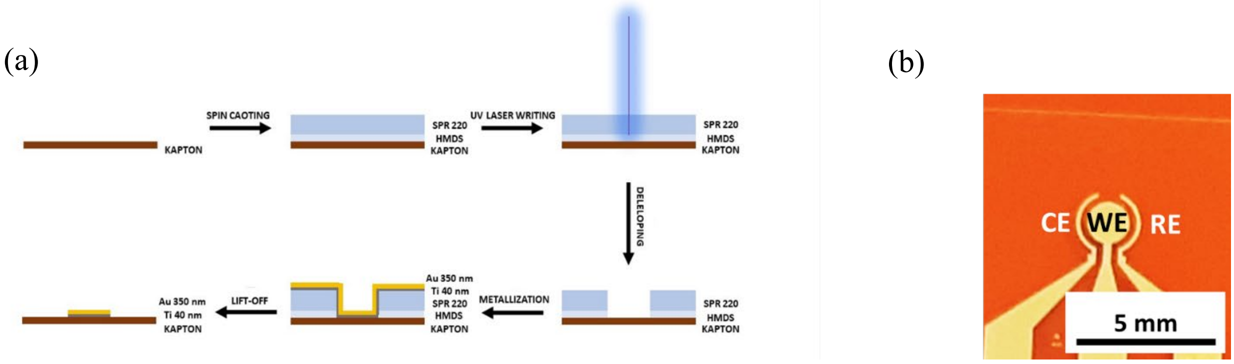

Figure 2.7: Manufacturing of the electrodes in integrated electrochemical array: (a) Optical lithography process on the flexible substrate; (b) three electrodes integrated device printed on the flexible substrate.

The substrate is primarily cleaned by rinsing with acetone and isopropanol copiously, dried under the nitrogen flow. Before spin coating of hexamethyldisilazane (HDMS), baking at 115 ºC for 10 min is required to remove the residues of the solvents. First HDMS solution is spin coated to enhance the adhesion of SPR 220® photoresist to the surface. Then the positive photoresist is deposited onto HDMS surface to achieve the final thickness of 2 µm. The 375 nm laser writing was carried on out with 11 mW of the laser power and 30 mm s^{-1} writing velocity. The duration of the writing was approximately 3 hours.

After the UV exposure, the wafer was immersed in MF-319® developing solution for 45 seconds to remove the exposed photoresist. At this step, the channels are created and ready for the metallization. Before the metallization, the surface was washed by water, dried under the nitrogen and baked at 115 ºC for 10 min. The wafer was metallized with the simple primary oxygen plasma etching to increase the adhesion. Then 20 nm of Ti and 350 nm of Au were deposited with the deposition rate 1 nm s^{-1} *via* electron-beam physical vapor deposition. For the lift-off of the metal which has been deposited to the unexposed photoresist, the sample was placed in a 60 ºC bath of SCV-14® stripper for 1.5 hours. In the end, the surface was successively washed with acetone and dried under the nitrogen flow. The integrated electrodes system with a planar gold working electrode, depicted on the **Figure 2.7b**, is ready for the modification and electrochemical applications.

2.6. Non-covalent surface modification and sensing of folic acid

The concept of cathodic EPD process was successfully implied in sensing of folic acid. Cyclodextrins have been widely used to host a various organic molecule due to their hydrophilic shell and hydrophobic cavity. To trap a folic acid molecule as a guest and transfer these interactions into a measurable electrochemical response, the integrated electrodes were functionalized with β-cyclodextrin-modified dopamine (dopa-CD) ligands on the EPD rGO interfaces *via* π-π stacking between dopamine aromatic stricture and sp^2 honeycomb lattice of rGO (**Figure 2.8**).

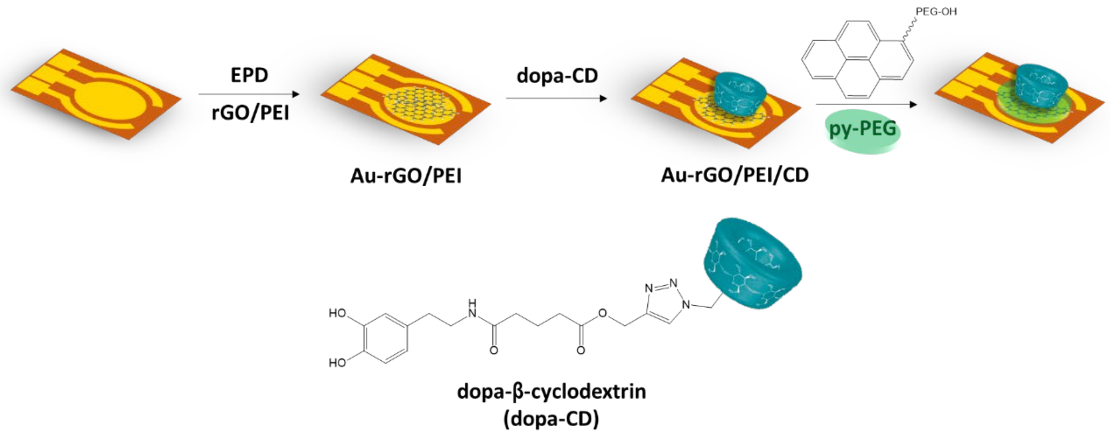

Figure 2.8: Modification of an integrated electrochemical system with reduced graphene oxide (rGO) by cathodic electrophoretic deposition (EPD) followed by modification with dopamine-modified β-cyclodextrin (dopa-CD) and O-(2-aminoethyl)polyethylene glycol modified pyrene (py-PEG). CD: cyclodextrin, rGO: reduced graphene oxide, PEI: polyethyleneimine.

For the purpose of direct cathodic deposition of reduced graphene oxide, a colloidal solution of rGO (1 mg mL^{-1}) was mixed with polyethyleneimine (1 mg mL^{-1}) at 1:1 v:v ration to achieve a positively charged nanomaterial ($\zeta = 40.3 \pm 2$ mV). The mixture was stirred for 48 h before EPD. The EPD was carried out in the configuration described above for the anodic EPD with the reversed polarity of the electrodes (e.g. gold planar electrode was used as a cathode and the platinum foil – as an anode). The deposition occurred by applying a DC voltage (5V) for 2 min. The interfaces were gently rinsed with water and dried under the nitrogen flow.

Optical images of unmodified and rGO/PEI interfaces are shown in **Figure 2.9a**. The roughness increase can be observed after the deposition process. From the SEM image of the modifies interface zooming on the working electrode (**Figure 2.9b**), one can observed the formation of a film of with a sheet-like structure. The morphology is similar to the one of 2.5 V EPD of GO with the reduction. The chemical composition of the formed rGO/PEI film was determined from the X-ray photoelectron (**Figure 2.9c**) and Raman (**Figure 2.9d**) spectroscopies. The C_{1s} spectrum can be deconvoluted into four bands, at 284.6 eV (C–C sp^2), 285.4 eV (C–C sp^3/C–H, C–N), 286.3 eV (C–O) and 287.8 eV (C=O). The XPS spectrum reveals the presence of the N-containing groups from PEI. Raman spectrum indicates two main bands at 1595 and 1350 cm^{-1} related to G and D peaks respectively. The D/G ratio is 0.71 due to decreased oxygen functionalities and fewer amounts of defects compared to GO.

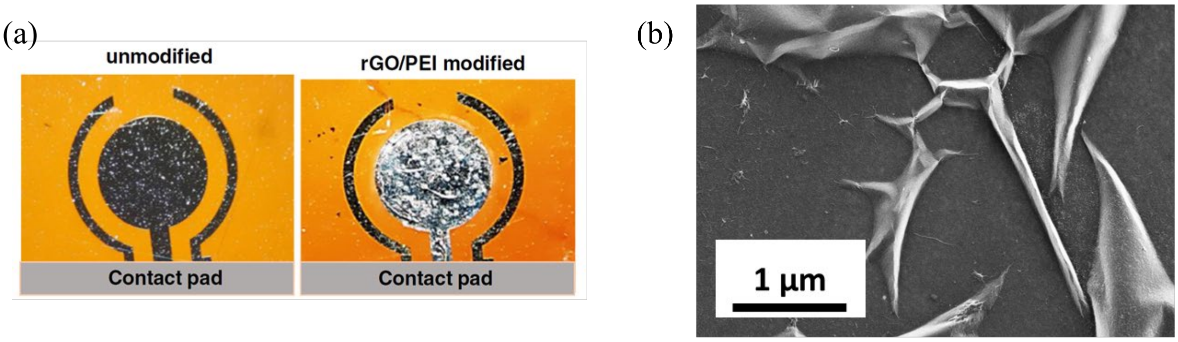

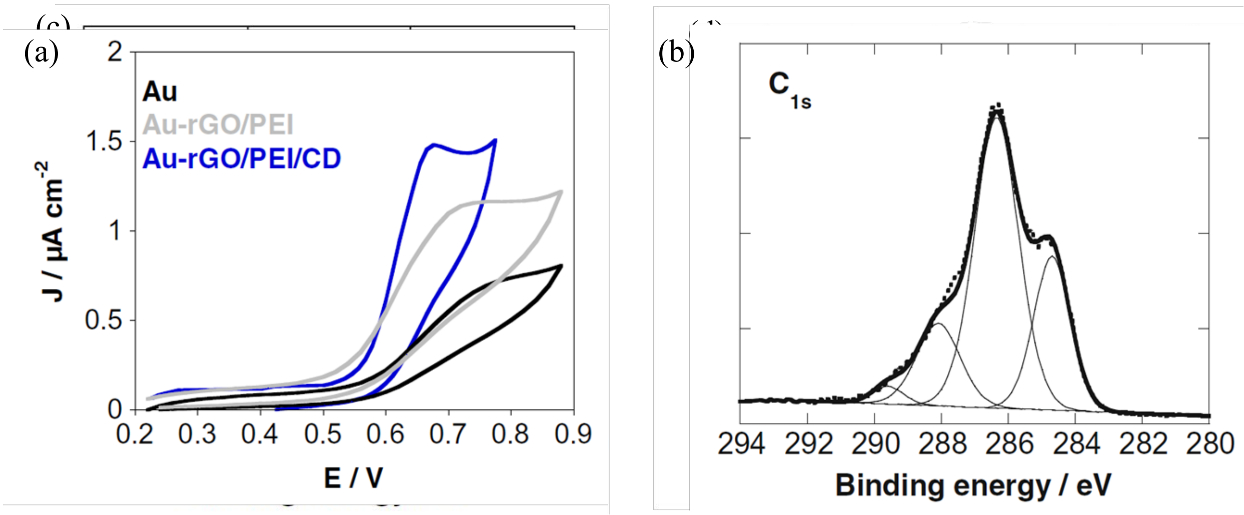

Figure 2.10: Characterization of β-cyclodextrin modified electrodes: (a) cyclic voltammetry response of folic acid (30 µM) in 1xPBS on Au (black), rGO/PEI modified surface (grey) and after dopa-CD functionalization (blue) with the scan rate 100 mV s^{-1}; (b) C_{1s} X-ray photoelectron spectrum of the rGO-PEI/CD-modified electrode

The surface of rGO/PEI was further functionalized with β-cyclodextrin-modified dopamine (**Figure 2.8**) synthetized according to the method in [6]. The aqueous solution of dopa-CD (120 mM) was drop casted on the graphene modified interface and let to bind for 2 h. Then the surface was washed three times with water. Aiming to get antifouling properties to the interface, the electrodes were immersed in PyPEG (1 mM) for 2 h. Finally, the device is washed in water and dried in air.

Electrochemical investigation *via* cyclic voltammetry demonstrates that folic acid can form a stable complex with β-cyclodextrin due to a high association constant $K_a = 14.81\ 10^3\ M^{-1}$ altering the electrochemical behavior of the interface upon the interaction. The cyclic voltammograms were recorded in 1xPBS solution after adding 30 µM of folic acid on the interfaces (**Figure 2.10a**). In case of bare gold electrode, a single anodic peak at 0.78 V is observed. The oxidation peak is shifted to 0.71 V for rGO/PEI modified surface. The shift can be explained due to π-π stacking between rGO and the aromatic structure of folic acid when no antifouling agent is used. Further, the interface modified with dopa-CD shows cathodic shift along with the increased current of the oxidation peak. This is observed due to the insertion of pteridine and glutamic acid groups of folic acid into the structure of the cyclodextrin.

The success of the surface modification was validated by XPS. The integration of β-CD results in a significant change in the high-resolution C_{1s} XPS spectrum (**Figure 2.10b**), with a strong band at 286.3 eV due to the presence of abundant OH functions of the β-CD ring. In addition, bands at 284.6 eV (sp^2-hybridized carbon), 288.2 eV (C=O, N–C=O, C=N), and 289.7 eV (O–C=O) are observed.

Differential pulse voltammetry (DPV) was used as a detection technique to determine the analytical response of Au-rGO/PEI/CD interface to the different concentration of folic acid (**Figure 2.11a-d**). The data were collected after the immersion of the electrodes in folic acid for 10 min. The measurements were carried out in 1xPBS with a modulation amplitude 5 mV, a step potential of 80 mV, a step height of 15 mV and a step time of 250 ms.

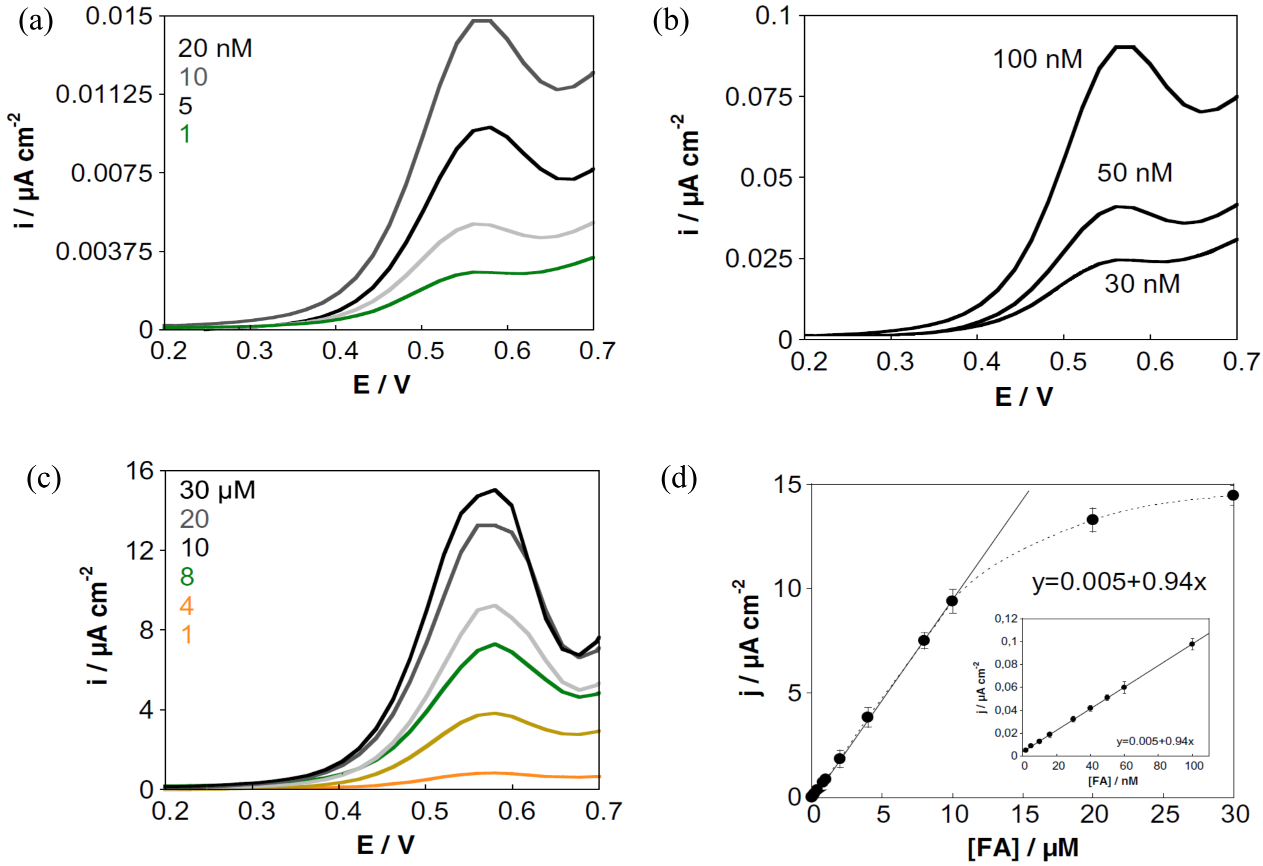

Figure 2.11: Electrochemical sensing of folic acid: (a)-(c) differential pulse voltammograms of dopa-CD modified reduced graphene oxide interfaces in 1xPBS upon addition of folic acid from 1 nM to 30 µM; (d) peak intensity as a function of folic acid concentration (inset shows the zoomed linear range of the lowest concentrations).

The lowest limit of detection was 1 nM when the signal was five time higher than the blank noise level (not shown). The sensor works in the linear regime between 5 nM and 10 µM (r^2 = 0.99) as shown in **Figure 2.11d**. The electrical response for the higher concentrations is saturated and reaches its plateau. Although, there are reported sensors with lower detection limits,[117] the Au-rGO/PEI/CD sensor demonstrated here can adequately distinguish between normal (4 to 25 nM in blood) and abnormal values of folic acid.

2.7. Conclusions

In conclusion, we have demonstrated the advantages of low potential electrophoretic deposition of graphene material on the planar gold electrodes as a deposition technique. The integrated electrodes on the flexible substrate were locally modified with rGO to obtain homogenous, mechanically and chemically stable interfaces with the excellent electron transfer characteristics.

To validate the possibility of controlled covalent functionalization, the electroreduction of the aryldiazonium salt on the EPD rGO surface was demonstrated aiming to obtain a functional monolayer which can be further functionalized by Cu(I) catalyzed "click" chemistry. We have demonstrated that a densely packed ferrocenenyl monolayer can be efficiently integrated on these rGO-modified surfaces as a model reaction. To conclude, the robust approach of the rGO surface modification with an organic monolayer which can be further functionalized by Cu(I) catalyzed "click" chemistry has been demonstrated. It has been proved that a closely oriented ferrocenenyl monolayer can be efficiently coupled on the rGO-modified surfaces. Due to the high kinetic rates and mild conditions of the "click" chemistry reactions, a wide range of functional groups can be immobilized on such surfaces. These results pave the way for the use of this technology for the modification of more complex electrode configuration such as graphene-based field-effect transistors and the integration of surface ligands for sensing-related applications.

Such rGO-modified surfaces were covalently modified with cTnI aptamer to perform electrochemical biosensing. The obtained aptasensor allowed cTnI sensing below the clinically relevant 26 pg mL^{-1} cut off level and enabled to determine the onset of moderate AMI. The sensor works in the linear range from 1 pg mL^{-1} to 1 ng mL^{-1}. The control experiment with another cardiac biomarker BNP-32 demonstrated a negligible low cross reactivity and proves the selective nature to cTnI biomarker.

The cathodic EPD rGO interfaces were further coupled with β-CD and pyrene-PEG for sensing of folic acid. The device demonstrates folic acid oxidation at 0.68 V with improved election transfer kinetics. Employing differential pulse voltammetry as a detection technique, the interface demonstrates a good electrocatalytic activity toward the oxidation of folic acid. Considering high association constant between folic acid and β-CD, the detection limit of 1 nM was achieved with a liner sensing regime from 5 nM to 10 μM.

Before proceeding to the next section, the publications summarizing the folic acid sensing on the flexible electrodes with electrophoretically modified interface by the graphene material and the covalent surface chemistry based on the diazonium grafting are attached, herein referred as [6] and [[118]] respectively:

Chekin, F.; Mishyn, V.; Barras, A.; Lyskawa, J.; Ye, R.; Melinte, S. et al. **Dopamine-functionalized cyclodextrins: modification of reduced graphene oxide based electrodes and sensing of folic acid in human serum.** *Anal Bioanal Chem.* 2019;411(20):5149-57.

Mishyn, V.; Aspermair, P.; Leroux, Y.; Happy, H.; Knoll, W.; Boukherroub, R. et al. **"Click" Chemistry on Gold Electrodes Modified with Reduced Graphene Oxide by Electrophoretic Deposition.** *Surfaces.* 2019;2(1).

Chapter 3: Electrical sensors based on reduced graphene oxide

3.1. Introduction

Next to the classical electrochemical biosensors, this chapter introduces a different way of signal processing using electrolyte-gated reduced graphene oxide-based field-effect transistors (rGO FETs). This electrical detection method allows not only to take advantages of the graphene properties and increase the sensitivity, but also *in situ* obtain kinetics from the surface ligand/receptor interactions. The surface of interdigitated electrodes is modified by graphene oxide (GO) *via* drop-casting method with the consequent chemical and thermal reductions and the properties of the device will be discussed (**Figure 3.1**).

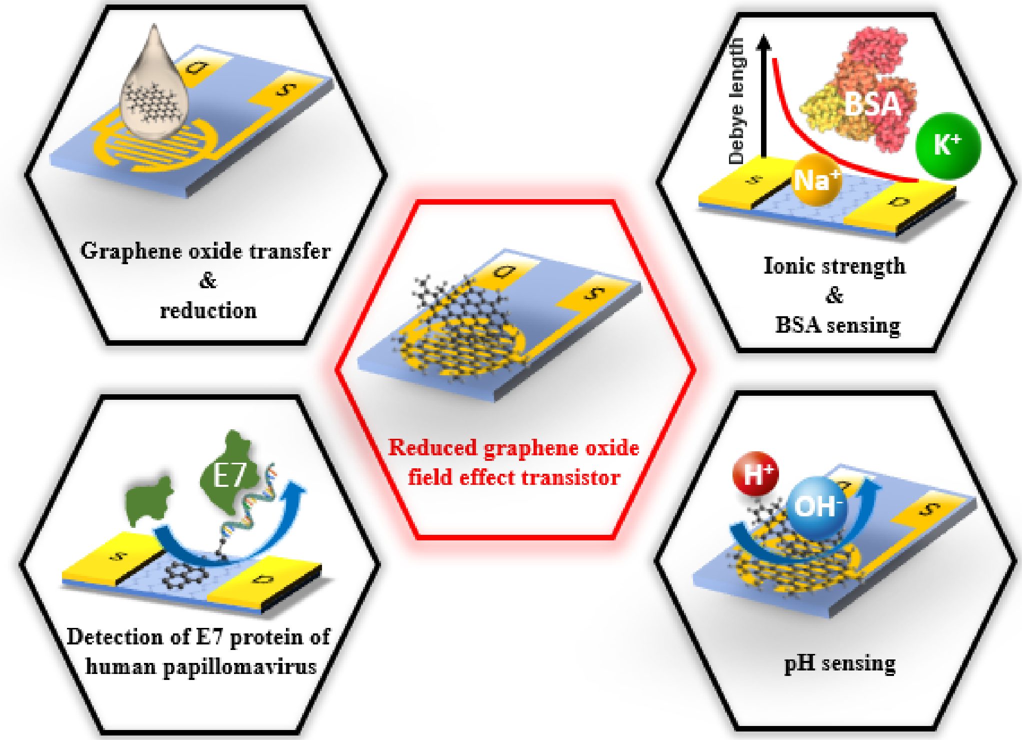

Figure 3.1: Electrical sensor development using reduced graphene oxide: Drop casting of graphene oxide as a deposition technique with the consequent chemical reduction, the influence of the ionic strength of liquid medium on non-specific sensing distance of BSA protein and pH sensing, non-covalent surface chemistry to anchor the aptamer receptor for sensing of E7 protein of human papillomavirus.

The effect of ionic strength on the performance of the transistor as well as on the Debye sensing length will be experimentally demonstrated employing Bovine Serum Albumin (BSA) as a model protein in different concentrations of commonly used phosphate buffered saline (PBS). The dependence on the Debye length will be confirmed theoretically and experimentally by calculating the Debye length as a working parameter and thus defining the limits of applicability for the presented rGO FETs.[105] In addition, the oxygen-containing groups on the interface can be used for revealing the surface pK_a *via* titration experiments to demonstrate the response of device to the different pH values.

Finally, the interest of rGO FET for the sensing of human papillomavirus (HPV), as one of the most common sexually transmitted viruses and a necessary factor for cervical carcinogenesis, will be demonstrated. The rGO FET sensor takes advantage over the standard viral detection in clinical settings (e.g. PCR or qRT-PCR) due to its close sensitivity to the classical methods, a lower cost and minimized investments and personal trainings. Non-covalent modification by the biorecognition elements will show the ability of the rGO FETs for the detection of E7 protein of human papillomavirus.

3.2. Manufacturing of liquid-gated reduced graphene oxide-based field-effect transistor

The interdigitated microelectrodes (90 pairs of 10 μm gold electrodes with 10 μm gap, Micrux Technologies) are cleaned in the UV-Ozone chamber (Jelight, USA) for 10 min and copiously washed before the modification. For the purpose of enhancing the adhesion between a GO sheet and the chip, the glass surface between the microelectrodes was covalently modified with (3-aminopropyl)triethoxysilane (APTES, 300 µL of APTES in 15 mL of ethanol) in a plastic falcon tube for 1 h. Subsequently, the chips were placed on a hot plate at 120 °C at ambient pressure for 2 h to anneal the self-assembled monolayer (SAM) of APTES and provide complete removal of the solvents from the interface.

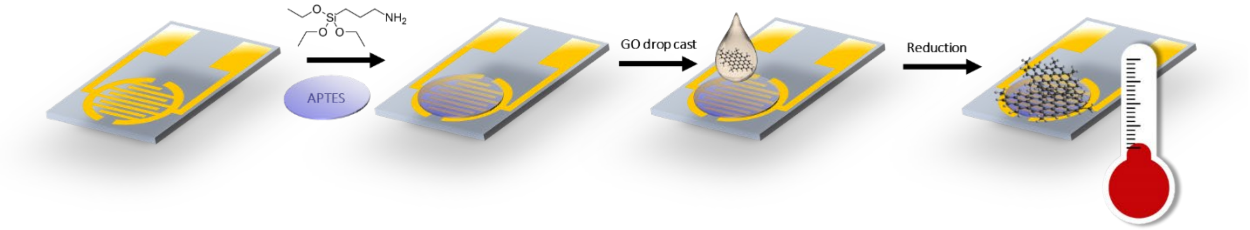

Figure 3.2: Manufacturing of rGO FETs: deposition process of GO onto the APTES modified surface of the interdigitated electrodes with consequent chemical and thermal reduction to rGO.

Following the surface cleaning and modification by APTES, the GO (12.5 µg mL^{-1}) solution was drop-casted on the surface of the device. The drop of 15 µL was incubated for 2 h at ambient conditions to allow the graphene flakes to bind to the surface. Subsequently, the excess of GO flakes was washed out from the surface by rinsing the chip with water.

Due to poor conductivity and the presence of the oxygen containing groups in the structure of GO, reduction is required. To reduce oxygen containing groups of GO structure and restore the properties close to the pristine graphene, the chips were places in a glass Petri dish and 1 mL of hydrazine was spread around the chips. The dish was placed in an oven at 80 °C for 4 h. The interfaces were furthermore annealed at 200 °C under vacuum for 2 h, resulting in stable and highly conducting electrical interfaces. The manufacturing process is summarized and depicted in **Figure 3.2.** After the chemical and chemical and thermal reductions, the source and the drain electrodes were linked by the conductive bridge of rGO flakes. The resistance drops after the reduction steps and usually has values between 20 and 30 Ohm for the device.

The surface characterization to validate the presence of sp^2 graphenic carbon is demonstrated in **Figure 3.3a-b**, which shows a series of C$_{1s}$ high-resolution X-ray photoelectron spectroscopy spectra of the transferred GO films before and after hydrazine/thermal annealing. The initial scan of GO-deposited films displays strong bands at 284.2, 285.0, and 286.6 eV, indicating the presence of sp^2 C–C, sp^3 C–C/C–H and C–O bonds respectively. The broad band at 288.2 eV indicates the presence of C=O groups. After the reduction, a relative decrease in the intensity of the sp^3 C–C/C-H bonds is observed, along with a strong removal of the C–O component as would be expected as the graphene structure is restored. Nevertheless, even after the reduction process, the relative amount of the oxygen-containing groups in rGO remains higher that in pristine graphene lattice, which also explains the difference in the properties and Raman spectra.

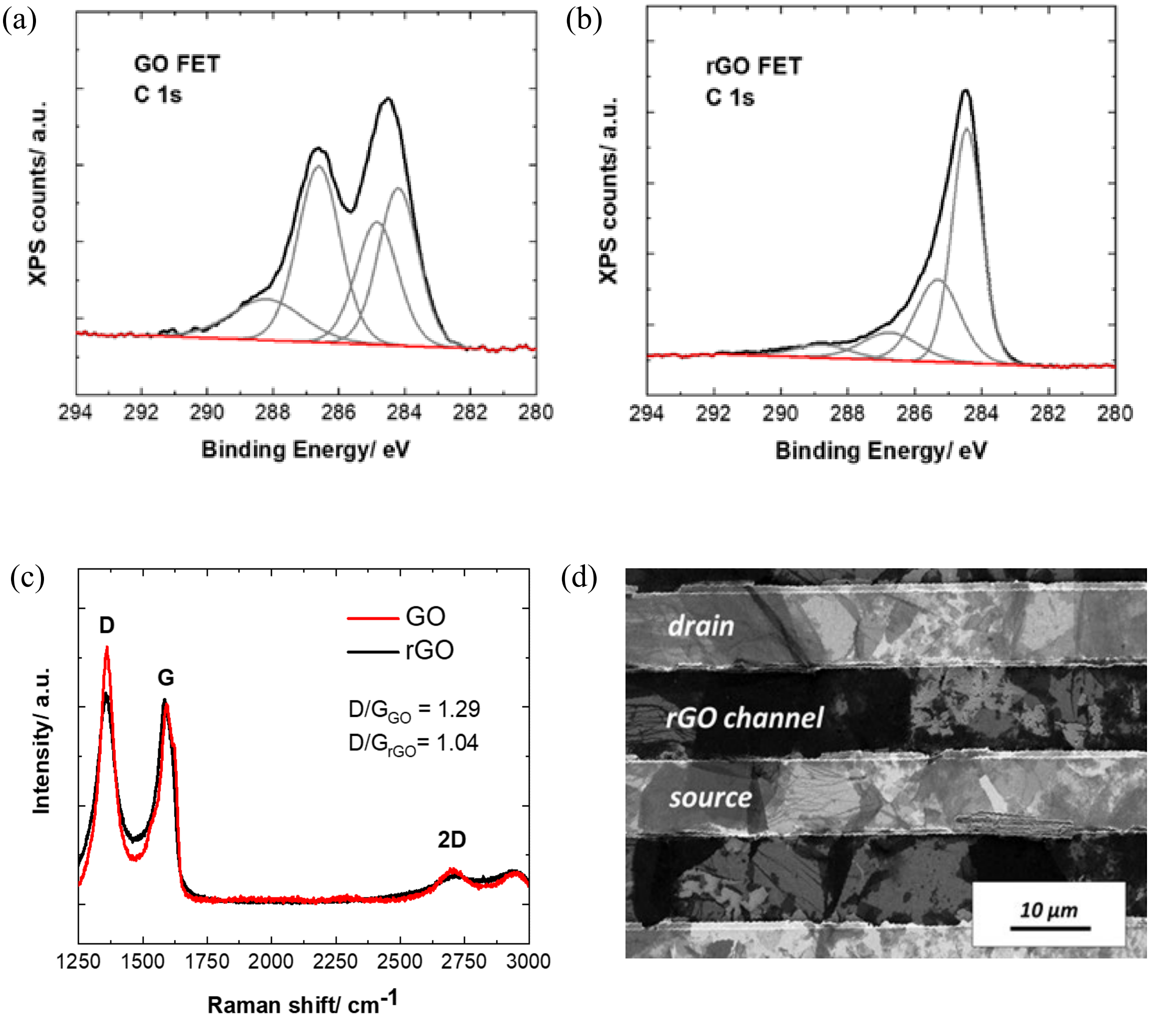

Figure 3.3: Characterization of rGO FETs: high-resolution C$_{1s}$ XPS spectra of (a) initial GO FET and (b) after the reduction to rGO; (c) Raman spectra of the GO (red) and rGO (black) transistors; (d) SEM image of the drain-source channel of the interdigitated electrodes upon coating with GO (12.5 µg mL^{-1}) followed by reduction to rGO for 4 h in hydrazine vapor and post-annealing at 200 °C for 2 h.

The transistor based on rGO exhibits two main bands at 1591 and 1345 cm^{-1} related to G and D peaks respectively (**Figure 3.3c**). Since rGO often consists of multi-layers of graphene with a smaller sheets size, the 2D band appears with a lower intensity compared to graphene monolayer. The low D+G contribution at ∼2940 cm^{-1} appears due to the impurities of rGO. The intensity ratio between G and D band has changes from 1.29 for GO to 1.04 for rGO indicating the reduction of oxygen-containing groups in the structure. However, the high intensity of the D peak indicates a significant content of defects in the rGO structure, which leads to different from pristine graphene electrical and chemical behaviors of the transistors. In order to get information about the morphology of the interfaces and surface coverage of the source-drain channel with graphene, SEM was applied. The result is shown in **Figure 3.3d**. The transistor based on GO, measured after the reduction process, exhibits non-homogeneous and random distribution of the graphene flakes. Nevertheless, due to the optimized parameters of GO deposition, the surface coverage remains high without graphitic particles. The size of the graphene sheets is sufficient to link the electrodes; as a result, the source-drain current can pass through the graphene channel.

3.3. Transistor properties

In order to measure the electrical properties of the transistors, the liquid-gated cell depicted in **Figure 3.4a** was used. The IDEs covered by the graphene material act as the source and drain electrodes with 50 mV bias applied, while the gate electrode made of Ag/AgCl is inserted in the lid of the cell and the electrical field applied through the liquid ionic medium (**Figure 3.4b**).

The $I_{DS}V_G$ curve was measured for the rGO FET to calculate the mobility of charges. The value has great importance on the sensor sensitivity, as the electrical readout is easier for the greater slope of $I_{DS}V_G$'s. The curve was obtained in -0.8 to +0.8 V gate potential window with the constant flow rate at 50 µL min^{-1} using 1xPBS ionic solution (**Figure 3.4c**). The obtained $I_{DS}V_G$ curve demonstrates ambipolar transistor properties with the slopes -385 and 473 µA V^{-1} for p- and n-types respectively which corresponds to 944 cm^2 V^{-1} s^{-1} and 1006 cm^2 V^{-1} s^{-1} mobility. The Dirac point lies at the value 0 V.

The stability was recorded by constantly applying -0.2 V of the gate voltage, where the slope has the highest value. For the given constant value of the gate potential, $I_{DS}(t)$ curve demonstrates the electrical stability of the interface under the constant conditions **(Figure 3.4d)**. It can be observed that the baseline linearly drifts with time with the rate of 12 μA h^{-1}. This can be explained due to the nature of rGO flakes. As it was demonstrated above, the structure and morphology of the surface suffer from the particles size distribution (inhomogeneity) and multilayered structure. Because of these factors, the graphene sheets can be washed out or displaced from the interface causing the electrical instabilities. However, the baseline is linear and drifts significantly only on the hours-scale measurements. This allows to predict a base line drift and subsequently helps to extract bioresponse signal.

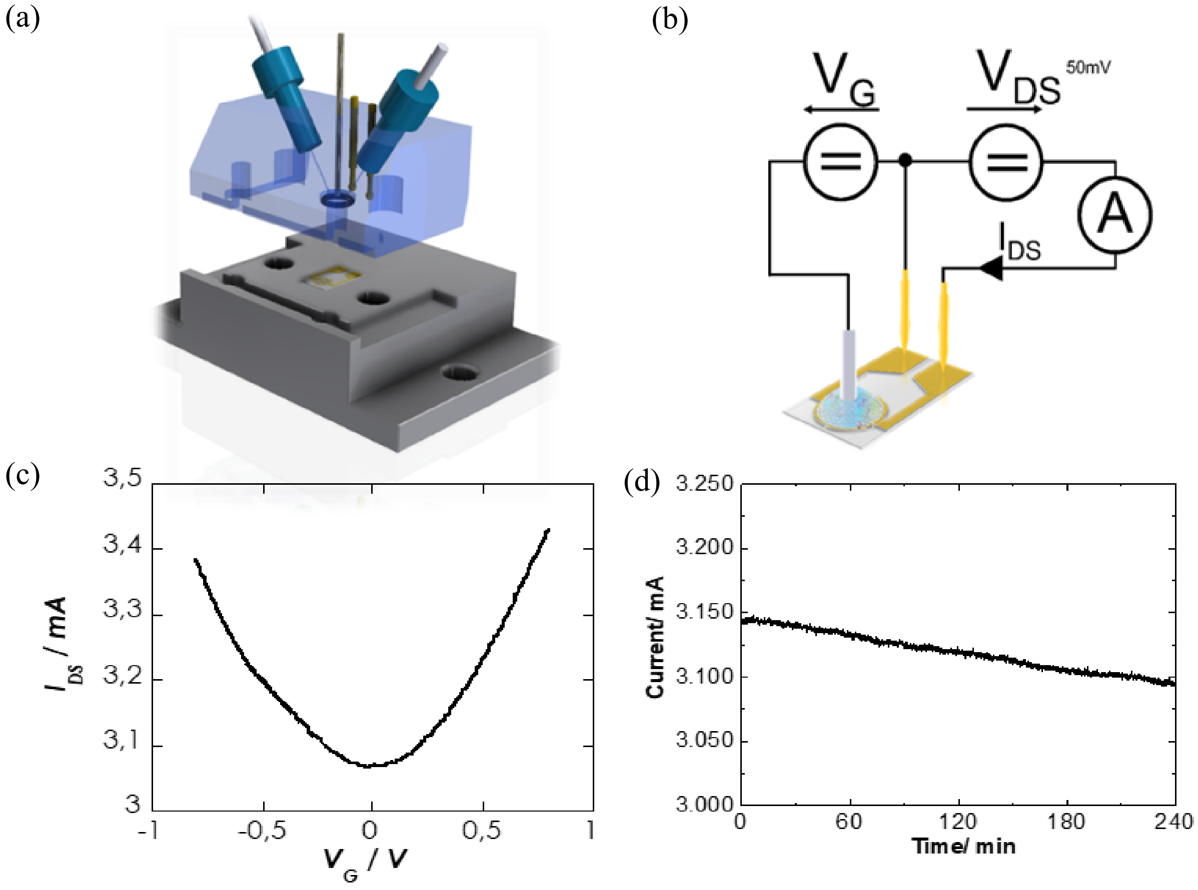

Figure 3.4: Electrical measurements of rGO FETs: (a) schematic representation of the liquid-gated cell; (b) electrical measurement setup to register the GFET readout in the liquid gate setup; (c) $I_{DS}V_G$ characteristic of unmodified solution-gated rGO FET in 1xBPS medium with the source-drain potential is 50 mV; (d) $I_D(t)$ stability graph of the rGO FET transistor obtained in 1xPBS with the flow rate 50 μL min^{-1} and the gate voltage -200 mV.

3.4. Change in source-drain current upon pH sensing

Generally, the biological analytes (e.g. saliva or serum) consist of aqueous medium where the electrolytes have higher concentration than a target biomarker. Due to the full charge of the ions, they cause charge redistribution on the graphene-based FET surface resulting in the change of the electrical properties of the transistor. As the structure of rGO has the oxygen-containing groups, including carboxyl group, the rGO-based transistor is susceptible to the pH change. This happens due to the proton exchange between the functional groups on the graphene surface and injected acid or base (**Figure 3.5a**). As the analytes have different pH values, caused by change in the concentration of H$^+$ or OH$^-$ ions, it is important to estimate how the change in the pH affects the sensor response.

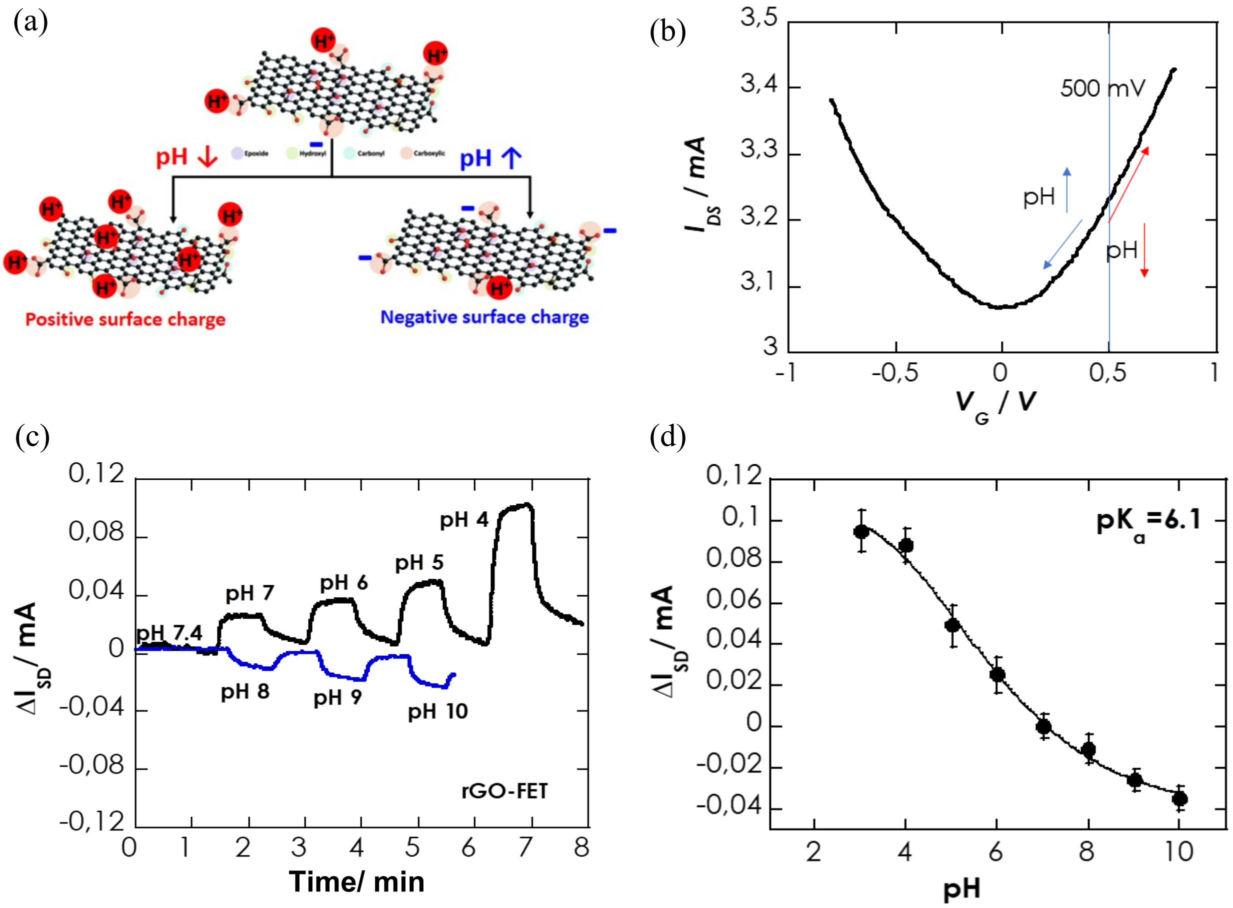

Figure 3.5: pH sensing on rGO FETs: (a) schematic representation of rGO flake demonstrating the surface polarization depending on pH value; (b) charge transfer characteristic as a function of gate potential of unmodified solution-gated rGO FET in 1xBPS medium with the source-drain potential is 50 mV. Blue line indicates the gate voltage of 500 mV selected for the $I_D(t)$ measurement and the arrows are showing the current change depending on the solution's pH. (c) $I_D(t)$ curve of pH value; (d) the change in the source-drain current as a function of pH.

To measure the source-drain current as a function of pH change, the solutions with different pH values but constant ionic strength were injected. The pH values were adjusted by adding HCl (Brønsted-Lowry acid) for the pH values less or equal than 7 or KOH (Brønsted-Lowry base) for the pH values greater than 7.4 to 1xPBS aqueous medium. Prior injecting the solution, the gate voltage was defined as +0.5 V in 1xPBS as the slope for n-type transistor is the steepest (**Figure 3.5b**). Then the solutions were injected on the rGO FET surface with the flow rate of 50 µL min^{-1} for 1 min following 1.5 min washing step with 1xPBS between each pH solution. The current change as a function of time is shown in **Figure 3.5c**.

For the constant gate bias, the source-drain current is modulated by the different pH as a decrease in pH means a higher concentration of H^+ ions in the system which shifts the equilibrium to the protonated forms of the functional groups on the graphene surface (**Figure 3.5a**). This results in accumulation of positive charges on the interface. Therefore, the current of the channel is modulated as it is the gate bias increased. In other words, the source-drain current increases as the surface charge is increased. The opposite is valid for the basic conditions, where the removal of the surface H^+ ions results in the negative surface polarization and the current decrease.

From the titration curve, one can derive the surface pK_a of 6.1 by plotting the current response as a function of pH (**Figure 3.5d**). The value is important for consideration, because the surface acidity has an influence on the surface reactivity. For instance, the acidity of the surface is favorable for linkage of a biorecognition element to the carboxyl groups present on the graphene surface as the activation reaction with EDC and Sulfo-NHS is the most efficient at pH 4.5-7.2.

3.5. Influence of the ionic strength of the medium on nonspecific detection of BSA

To evaluate the influence of the ionic strength of the solution on the transistor performance, different concentration of phosphate buffered saline were used. Being commonly used in biological research, PBS solution allows to keep the constant pH at 7.4 and the ion concentration of the solution matches those of the human body (isotonic). This aqueous medium was used in this work to perform sensing of biomolecules and calibration curves of their electrical response as it closely mimics the ionic strength of real biological analytes.

The ionic strengths (I) of different PBS dilutions with the component concentration c_i and the ion charge x_i were calculated using the **Equation 3.1**. The Debye length (λ_D) is a measure of how far into the conductor the potential of an electrode or probe is observed. The corresponding

Debye length λ_D was estimated employing the **Equation 3.2** with permittivity $\varepsilon = \varepsilon_r\varepsilon_o$ where ε_o is vacuum permittivity ($8.85\ 10^{-12}$ C V^{-1} m^{-1}) and ε_r is water relative permittivity (78.4), k is Boltzmann constant ($1.38\ 10^{-23}$ eV K^{-1}), T is the temperature (298 K), e is the charge of electron ($1.60\ 10^{-19}$ C), N_a is the Avogadro constant ($6.02\ 10^{-23}$ mol^{-1}) and I is the ionic strength of the solution of the buffer in mol m^3.

$$\mathbf{I = \frac{1}{2}\sum_{n=1}^{i} c_i x_i^2} \quad \textit{Equation 3.1}$$

$$\boldsymbol{\lambda_D = \left(\frac{\varepsilon kT}{e^2 N_a 2I}\right)^{\frac{1}{2}}} \quad \textit{Equation 3.2}$$

The composition of different dilutions of PBS as well as their ionic strengths and corresponding Debye lengths are summarized in the **Table 3.1**. It can be observed that for the low ionic strength solutions the Debye length has the highest values, which is preferable for liquid-gated FETs. The high screening length allows sensing of a charged target on a longer distance from the interface making the electrical read-out measurable.

Table 3.1: Phosphate buffered saline composition, total ionic strength and corresponding Debye length for different dilutions.

	NaCl/ mM	KCl/ mM	Na_2HPO_4/ mM	KH_2PO_4/ mM	Ionic strength/ mM	Debye length/ nm
1x	137	2.7	10	1.8	151.5	0.79
0.5x	68.5	1.35	5	0.9	75.75	1.10
0.1x	13.7	0.27	1	0.18	15.15	2.46
0.01x	1.37	0.027	0.1	0.018	1.51	7.80
0.001x	0.137	0.0027	0.01	0.0018	0.15	24.75
0.0001x	0.014	0.0003	0.001	0.0002	0.015	78.28

$I_{DS}V_G$ curves as well as $I_D(t)$ sensorgram were measured to demonstrate a change in the source-drain current induced by the electrolyte's ionic strength. Primarily, different dilutions (1xPBS, 0.1xPBS and 0.01xPBS corresponding to dilution factor 10 respectively) were injected in order of increasing ionic strength over the surface of unmodified rGO FET with the flow rate of 50 µL min^{-1} with the constant gate bias of -0.1 V (**Figure 3.6a**). During the injection of each ionic solution, the $I_D(t)$ curve was paused and $I_{DS}V_G$ characteristics were recorded in -0.8 to +0.8 V gate potential window (**Figure 3.6b**). Then the surface was rinsed with the lowest concentration of PBS to regenerate the interface.

The Dirac point moves to the negative values with the increase of the ion concentration. Along with this phenomenon, it can be observed that for high ion concentrations the slope of electron and hole regimes increase and the slope for $I_{DS}V_G$ curves has the highest values for 1xPBS. The effect is favorable for the biosensing as the bioanalyses usually dissolved in a high ion concentration medium and the slope values for the high ion solvents has higher values facilitating the electrical read-out. On the other hand, with the higher ion concentrations the Debye length is decreasing. This reduces the distance at which the charged molecules can be screened. Thus, it is important to demonstrate the influence of ionic strength on the Debye sensing length.

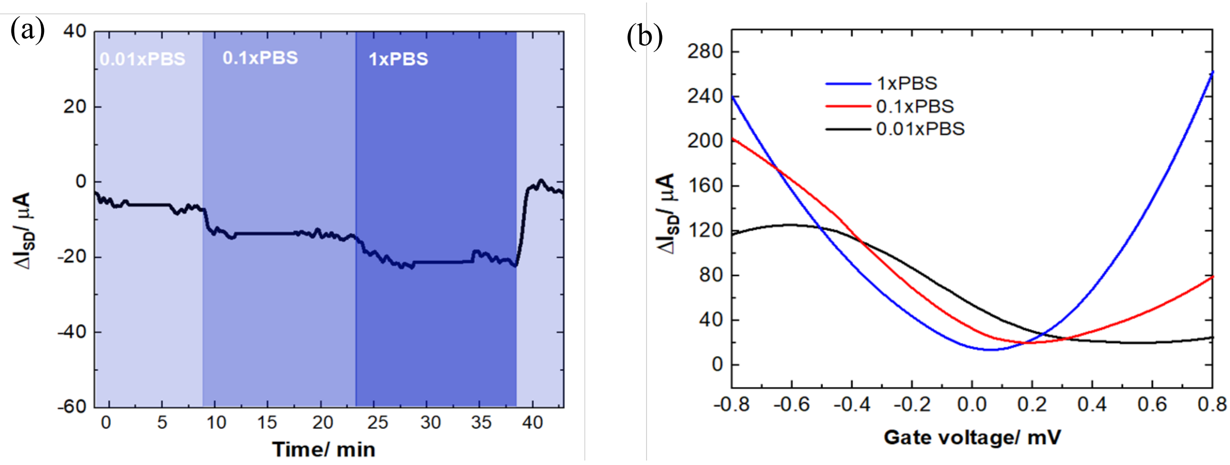

Figure 3.6: The influence of ionic strength on rGO FET electrical performance: (a) electrical response of rGO FET to gradually increasing the ionic strength (showed by background color change) from 0.001x to 1xPBS at gate voltage -100 mV. (b) $I_{DS}V_G$ characteristics recorded during the current saturation when the different concentrations of buffer were injected.

The protein sensing deepens on different parameters, e.g. charge carrier mobility and Debye screening length induced by the total amount of ions in the system. To validate the intensity of the electrical signal caused by nonspecific interaction, BSA protein (molecular weight 66.4 kDa) at the constant concentration of 50 μM was used. The protein was dissolved in 0.001x, 0.01x, 0.1x, 0.5x and 1xPBS and injected in the cell with the flow rate of 50 μL min^{-1}. Each injection was followed by stabilization and washing steps with the corresponding solution before and after the protein introduction. For the $I_D(t)$ curve, the source-drain voltage was 50 mV, and the gate potential was set to 0.5 V.

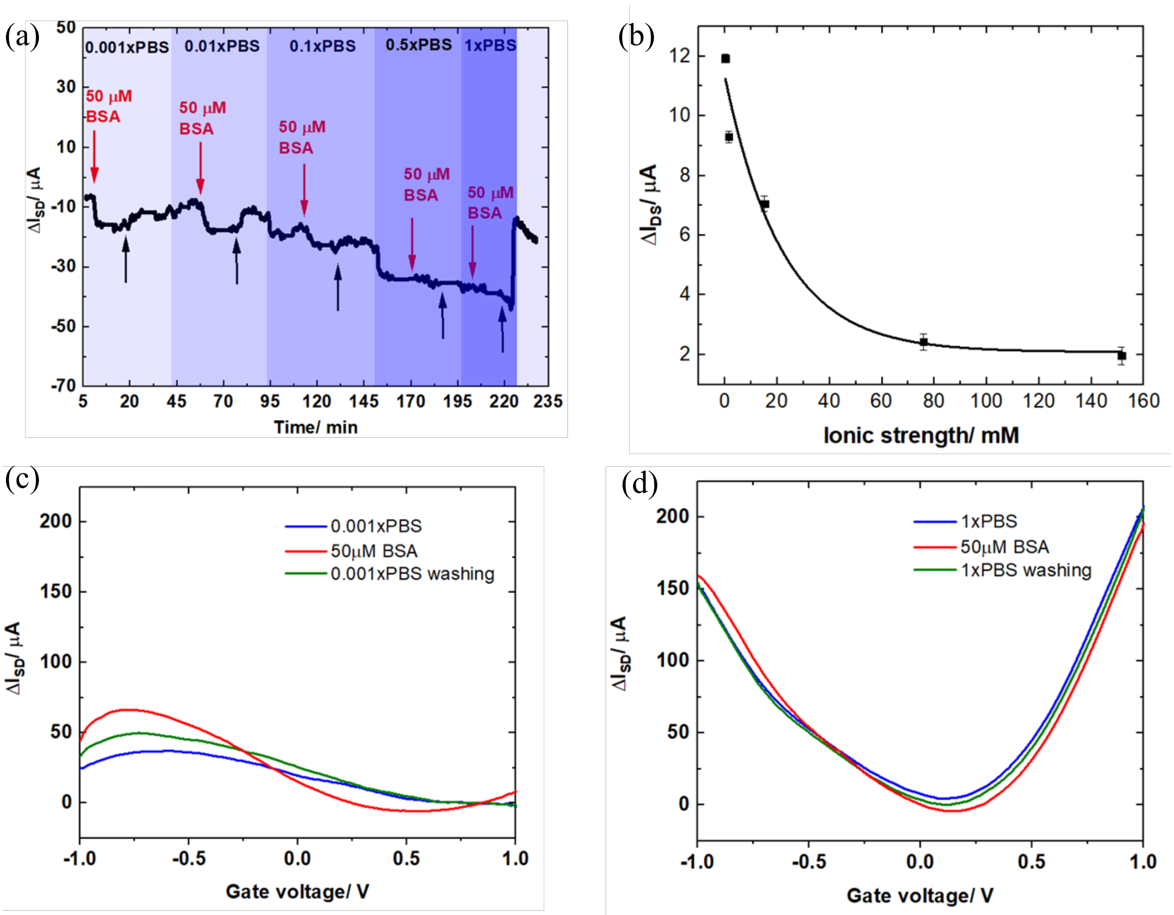

Figure 3.7: BSA non-specific sensing: (a) electrical response of rGO FET to 50 µM BSA, gradually increasing the ionic strength (showed by background color change) from 0.001x to 1xPBS at gate voltage 500 mV. Black arrows indicate the washing step with the same buffer medium for corresponding BSA injection. (b) The current changed induced by BSA injection as a function of total ion concentration of the solution. $I_{DS}V_G$ characteristics recorded during the equilibration, injection of BSA and wash-off steps in (c) 0.001x and (d) 1x PBS medium.

As expected, shown in **Figure 3.7a**, the highest measured electrical response of 50µm BSA was observed in the lowest ionic medium. As the pH value of PBS buffer is significantly higher than the isoelectric point of BSA (pI=4.7), the protein molecules are negatively charged causing the negative response in $I_D(t)$ curve. The intensity of the signal is decreasing with the decrease of the Debye-length induced by high concentration of ions in the system (**Figure 3.7b** and **Table 3.1**). This can be associated with the change of in the electrical double layer interface (capacitance) and the charge carrier density on the surface of graphene. For low ion concentration, the charge mobility decreases, but the sensor is more sensitive to BSA charged molecules. This causes an evident change in $I_{DS}V_G$ characteristic when the protein is injected (**Figure 3.7c**). In contrast, the charge mobility increases for high ion concentration with the decrease of the sensitivity of the device. The $I_{DS}V_G$ curve has almost no variation when the analyte is injected (**Figure 3.7d**).

In conclusion, the experiment demonstrates the combination of two effects: the improved transistor characteristics and the decrease of Debye screening length for high ion concentration. This paves the way to the importance of the ion medium on graphene sensors. It is crucial to find an equilibrium between an enhanced signal read-out and the working screening distance of the sensor. The solution could be found in either desalting of an analyte or a special surface chemistry can be applied to detect biomolecules in a high ion medium.

3.6. Non-covalent modification of rGO FET for the detection of E7 protein of human papillomavirus

In order to create a functional surface for selective binding of HPV-16 E7 biomarker, the rGO FET was first modified with 1-pyrenebutyric acid (PBA) followed by NHS/EDC activation of carboxyl groups to create a covalent bond between NH_2 terminal group of the aptamer and the carboxyl groups on the transistor (**Figure 3.8a**).

First, the device was submersed into 0.5 mM solution of PBA with 5 mM of pre-conjugated pyrene-PEG_{12} molecules in dry DMSO for 12 hours to form π-π stacking bond between the aromatic rings of the pyrene-based molecules and graphene surface. This step aims to create surface carboxyl groups spaced with PEG chain in 1:10 ration. The ration has been experimentally validated to be optimal for having anti-fouling properties and good for biosensing. Then the surface was gently washed with dry DMSO to avoid multilayered stacking and wash the excess of the molecules from the surface. The interface was dried under the nitrogen flow.

To validate the presence of PBA/PyPEG on the surface, $I_{DS}V_G$ characteristics were recorded before and after the surface modification. The Dirac point is observed at 130 mV for unmodified rGO FET and at 80 mV after the modification with PBA/PyPEG (**Figure 3.8b**). The interfaces exhibit an ambipolar transistor nature with a linear regime for both charge carrier types below ± 1 V_G. From the linear fit of the slopes both of n- and p-type transistors, the charge carrier mobility was found in the range of 725 $cm^2\ V^{-1}\ s^{-1}$ for electrons and 680 $cm^2\ V^{-1}\ s^{-1}$ for holes mobility of the modified device.

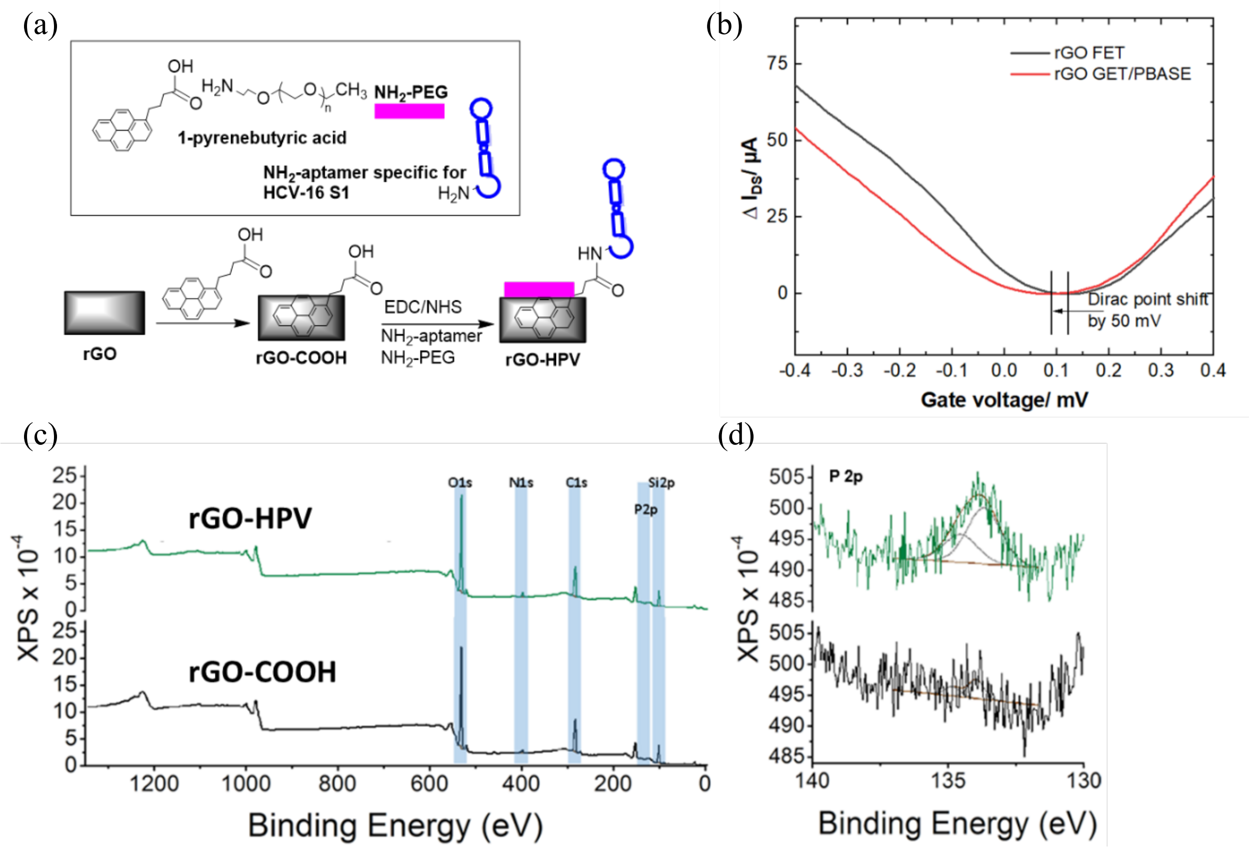

Figure 3.8: Modification of rGO FET with PCA linker and the aptamer for sensing of HPV-16 E7 protein of human papillomavirus: (a) modification scheme of the rGO FET with RNA HVP-16 E7 aptamer and antifouling PEG chain; (b) transfer characteristics of a solution-gated rGO FET before and after surface modification with a PBA linker, leading to a Dirac point shift of 50 mV; (c) XPS spectra of the rGO surface before and after modification with a pyrene linker for aptamer immobilization. Green represents the XPS spectrum of the aptamer-modified rGO surface, while the black spectrum corresponds to the surface functionalized with only PyPEG/PBA molecules. (d) High-resolution XPS spectra in the P_{2p} region of the rGO surface before and after aptamer immobilization to investigate the uptake of phosphate, present in the aptamer backbone.

Next to PBA/Py-PEG immobilization, the carboxyl groups were activated by immersion into a solution of NHS (15 mM)/ EDC (15 mM) in 1xPBS for 30 min, following the amide bond formation with 5’-NH_2-terminated aptamer with eight repetition TTT units acting as a spacer between the aptamer binding side and the interface of the transistor. The aptamer sequence was NH_2-5′-$(TTT)_8$ GGG AGG ACG AUG CGG AAG CAT CAA GGG TGA TCG TTT GAC CCT CCC CAG ACG ACU CGC CCG A-3’. The modification was carried out by drop casting of 15 µL, 100 nM of the apatamer solution for 40 min at ambient conditions. The surface was then gently washed with 1xPBS buffer and used for the biosensing immediately.

The success of the aptamer surface modification was confirmed by XPS analysis of the interfaced with PBA only and after the aptamer linkage (**Figure 3.8c**). After the aptamer modification, high-resolution XPS spectrum in the P_{2p} region shows the appearance of the signal caused by the uptake of phosphate, present in the aptamer backbone (**Figure 3.8d**).

The modified interface was used to electrically monitor aptamer-binding interactions in real time by injecting the increasing concentrations of HPV-16 E7 recombinant protein in 0.01xPBS (**Figure 3.9a**). As the target protein binds to the aptamer specific sides, a source-drain current change proportional to a concentration is observed (**Figure 3.9b**).

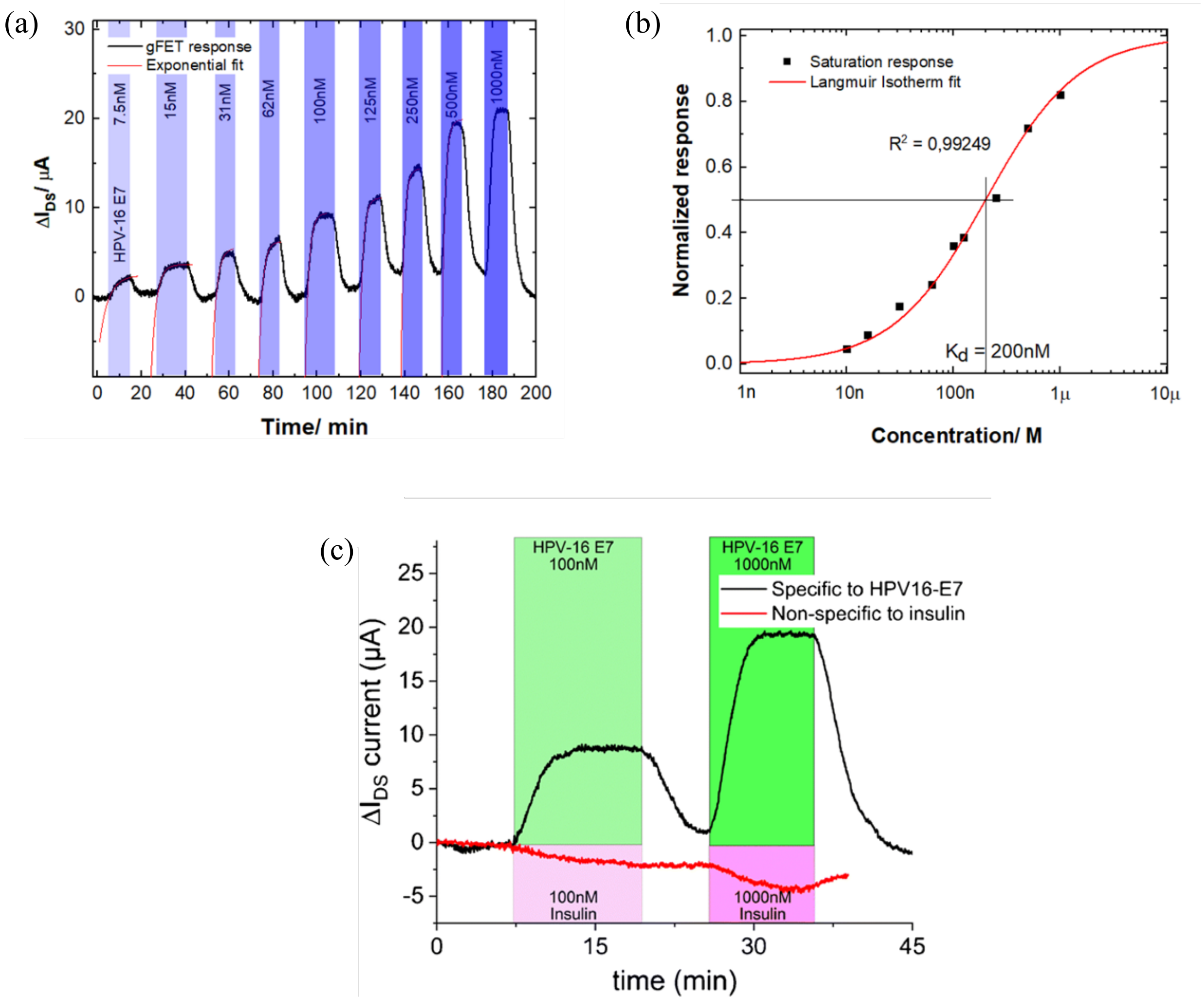

Figure 3.9: Electrical sensing of HPV-16 E7 protein of human papillomavirus (a) FET-based sensing of HPV-16 E7 protein in real time using aptamer-modified rGO FET when the interface is exposed to increasing concentrations of HPV-16 E7 proteins (7.5, 15, 31, 62, 100, 125, 250, 500, and 1000 nM) in PBS (0.1xPBS, pH 7.4). (b) Normalized response obtained from the I_{DS} current, generated by different HPV-16 E7 protein concentrations and fitted to a Langmuir isotherm. The K_D at half saturation equals 200 nM. (c) $I_{DS}(t)$ signal of aptamer-modified rGO FET upon specific binding to HPV-16 E7 (black) compared with non-specific binding of insulin (red) to the surface.

The equilibrium current values and the kinetic of on- and off-rates were used to determine the dissociation constant (K_D) of the binding reaction. **Figure 3.9b** shows the normalized to maximum current saturation value of the aptasensor as a function of the protein concentration. The curve was fitted using a Langmuir isotherm model **(Equation 3.3**).

$$\Delta \mathbf{I}_{\mathbf{SD}}^{\mathbf{equ}} = \Delta \mathbf{I}_{\mathbf{SD}}^{\mathbf{max}} \times \frac{[\mathbf{HPV-16\ E7}]}{[\mathbf{HPV-16\ E7}]+\mathbf{K_D}} \quad \textit{Equation 3.3}$$

The equation yields K_D value of 200 nM at half saturation, which agrees with previous reports of aptamer-protein binding reaction.[119] The detection limit (LOD) for the E7 protein was determined to be about 1.75 nM (100 pg mL^{-1}) from five blank noise signals (95% confidence level) with the working sensing range from 7.5 – 1000 nM (**Figure 3.9b**). To underline specific binding, the change in electrical signal upon binding to insulin, a protein of comparable size, was recorded at comparable concentrations (**Figure 3.9c**). The sensor had a minor negative current response not significant for the detection of the target analyte. Chekin et al. has reported an electrochemical aptasensor based on graphene/MoS_2 electrode with the linear range 3.5 pM – 35.3 pM to the same targeted protein.[120] Compared to the reported results, the rGO FET aptasensor presented in this work has higher sensing range to the capsid protein. However, to our best knowledge, this is the first aptamer-based label and redox-free HPV biosensor utilizing graphene field-effect transistor as a transducer.

3.7. Conclusions

In contrast to the classical electrochemical detection techniques, rGO-based liquid gated field-effect transistors were introduced as an electrical platform for biosensing. The interface was characterized by utilizing XPS, Raman and SEM analyses. The electrical properties as well as the influence of the ionic strength and pH on the device performance has been shown. We have demonstrated by using non-specific interactions of BSA protein with the device surface that at high ionic strength the transistor characteristics have the electrical improvement but the high concentration of ions shortens the Debye length and makes the sensing infeasible. In our case, an electrical response of BSA protein was measurable up to 0.1xPBS concentration.

Sensing of HPV-16 E7 protein in 0.01xPBS medium was demonstrated on rGO FET. In order to attach the ligand, the surface was pre-modified with PBA/pyrene-PEG in a ration 1:10. The aptamer was then covalently coupled to carboxyl group of PBA *via* NHS/EDC protocol. The protein binding in real time revealed preferential binding of HPV-16 E7 in 7.5 nM - 1000 nM range. The dissociation constant was found as 200 nM, which agrees with previous reports of aptamer-protein binding reactions.

Before proceeding, the results of the device manufacturing of the rGO-based liquid-gated field-effect transistors for sensing of HPV-16 E7 biomarker of human papillomavirus are summarized in the attached publication, herein referred as [26]:

Aspermair, P.; Mishyn, V.; Bintinger, J.; Happy, H.; Bagga, K.; Subramanian, P. et al. **Reduced graphene oxide–based field effect transistors for the detection of E7 protein of human papillomavirus in saliva.** *Anal Bioanal Chem*. 2020.

Chapter 4: Liquid-gated electrical sensors based on CVD graphene field-effect transistors

4.1. Introduction

This chapter is dedicated to the manufacturing of liquid-gated field-effect transistors based on chemical vapor deposited (CVD) graphene (**Figure 4.1**). The full process from the graphene growth on a copper substrate to the final device characteristics where the graphene is transferred by the means of wet transfer will be reported. We investigate the graphene surface morphology, electrical and Raman characteristics to compare unmodified devices with the ones where the surface modification was applied.

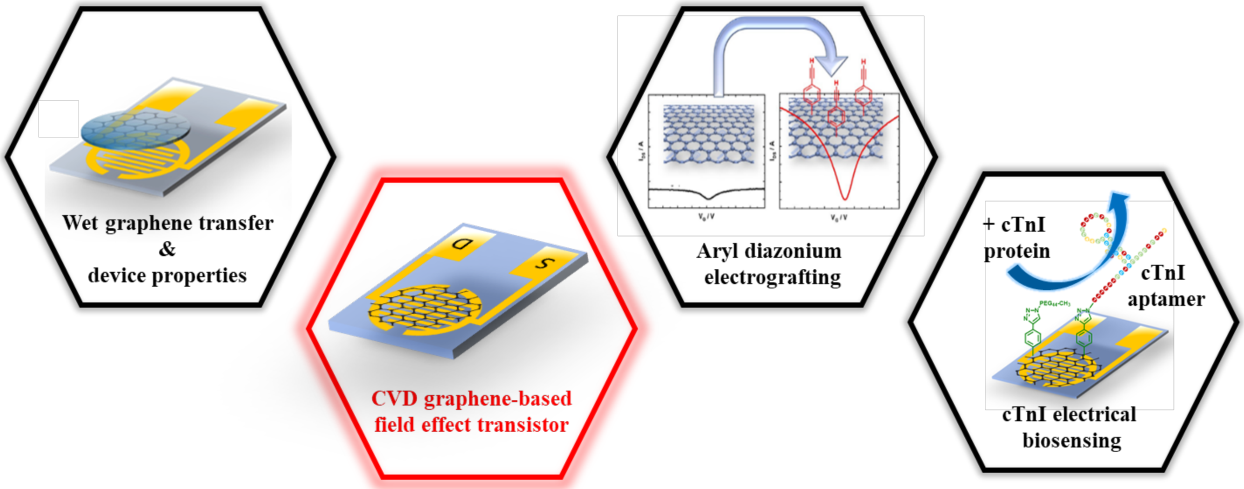

Figure 4.1: Electrical sensor development using CVD graphene: wet transfer of CVD graphene onto the interdigitated electrodes surface; covalent graphene surface modification *via* electrochemical reduction of diazonium salt with the improved transistor properties; electrical aptasensor for sensing of cardiac cTnI biomarker.

Further we demonstrate here the possibility of electrochemical surface grafting using a triisopropylsilyl protected ethynylphenyl diazonium salt, 4-[(triisopropylsilyl) ethynyl]benzenediazonium tetrafluoroborate (TIPS-Eth-ArN$_2^+$), known for its surface limiting grafting capabilities to a monolayer due to the presence of the bulky triisopropylsilyl (TIPS) group.[65, 81] It is demonstrated that during optimized conditions, the formed alkynyl-terminated GFET (**Figure 4.1**) keeps a charge mobility above 1000 cm^2 V^{-1} s^{-1} outperforming GFETs modified with other aryl diazonium salts, such as the well-known 4-nitrobenzene diazonium tetrafluoroborate. The formation of functional monolayer on the graphene sheet and high charge mobility together with the possibility to integrate ligands further *via* "click" chemistry are large steps further to the development of highly sensitive sensing interfaces.

Indeed, these alkynyl-terminated GFET can be used as a platform for biomodification. The enormous clinical importance of developing reliable methods and devices for testing levels of cardiac Troponin I (cTnI), which are directly correlated to Acute Myocardial Infarction (AMI), has spurred an unmatched race among researchers for the development of highly-sensitive and cost-effective sensing formats to be able to differentiate patients with early onset of cardiac injury from healthy individuals with a mean cTnI level of 26 pg mL^{-1}. In consequence, the interfaces were coupled with cTnI specific aptamer *via* "click" chemistry to specifically detect corresponding cardiac biomarker in PBS solution. The electrical read out has the advantage of being label-free with a sensing limitation due to ionic strength effects, which can be limited using poly(ethylene) glycol surface ligands.[121]

4.2. Manufacturing of CVD graphene-based field-effect transistors

In order to create FET, chemical vapor deposition (CVD) graphene is used to connect the source and the drain. The monolayer graphene is grown by CVD, on commercial Cu foil from Alpha Aesar (high purity - 99,9999%). Graphene growth has been carried out in a Jipelec JetFirst Rapid Thermal CVD (RTCVD) which allows to heat and cool at high rates (10°C s^{-1}). The growth itself is decomposed as a heating, an annealing, a growth and a cooling. We used a mixture of 100 sccm of argon and 5 sccm of dihydrogen during all the steps and 20 scccm of methane as a precursor during the growth phase. We first cut the Cu foil in small pieces (2.5 × 2.5 cm), clean them with acetic acid for 5 min, acetone for 5min and IPA for 5min under ultrasound in order to remove all possible copper oxide and to have the cleanest surface possible. We then put the pieces onto a Si wafer in the chamber. We proceed to a high vacuum ($<5 \times 10^{-5}$ bar) before starting and then we start the heating for 5 min from room temperature to 300°C and then 2 min from 300°C

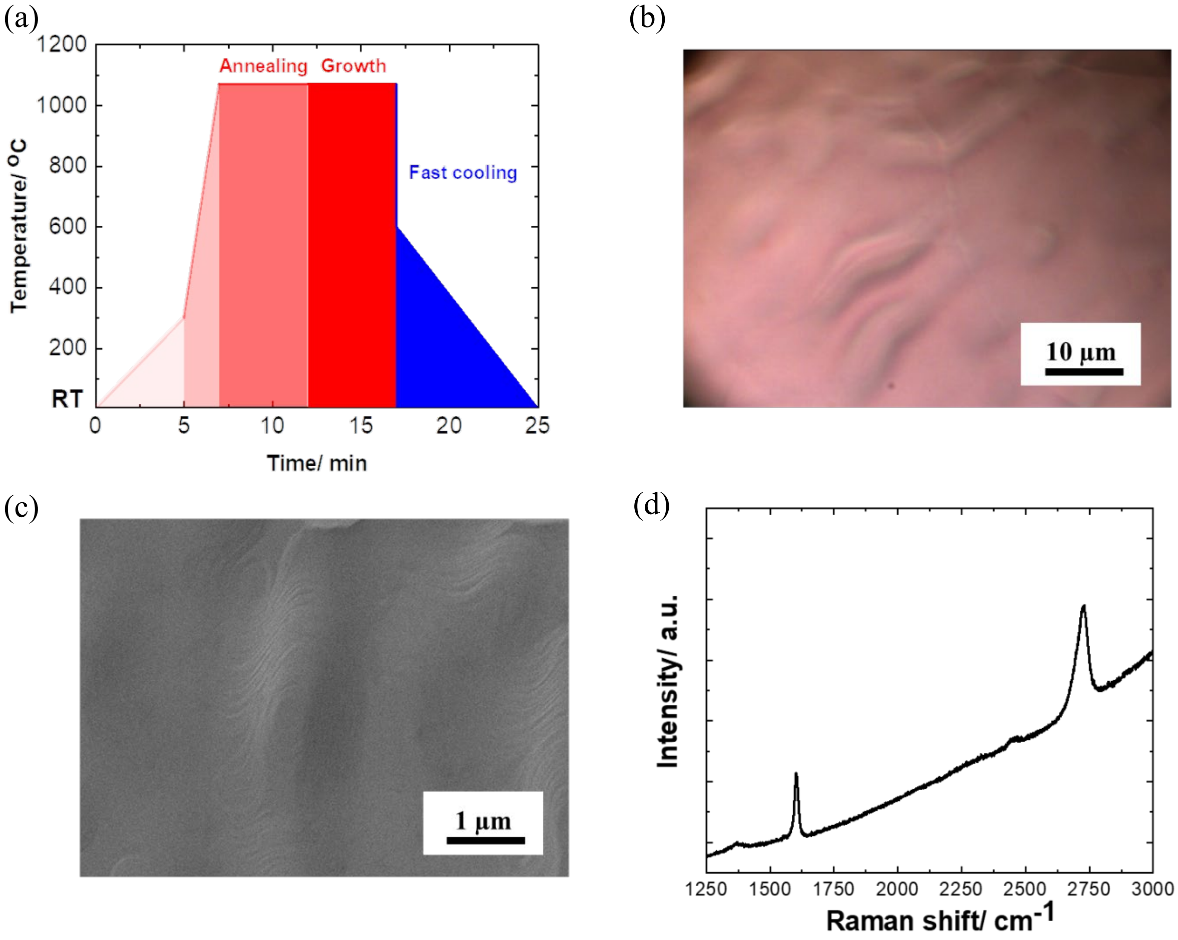

Figure 4.2: CVD graphene growth and characterization on copper foil: (a) temperature profile for the chemical vapor deposition of graphene; (b) optical and (c) SEM images of CVD graphene grown on the copper substrate; (d) Raman spectrum of the obtained CVD graphene on Cu foil.

to 1070°C, then the annealing for 5 min, we continue with the growth for 5 min and we finish with a quick cooling of the chamber using a water flow (with a decrease rate of 60°C s^{-1} from 1000 to 600°C), then around 10 min to reach room temperature (**Figure 4.2a**). The obtained material was first investigated for the presence of the defects and imperfections using optical microscopy. **Figure 4.2b** shows the copper foil with CVD graphene. A very flat and homogeneous surface can be observed. SEM was applied to verify the surface homogeneity on a higher magnification (**Figure 4.2c**). The analysis has confirmed a high quality of obtained graphene without visible multilayers and graphitic particles. In order to estimate the number of graphene layers, Raman spectroscopy was used. The spectrum of CVD graphene on Cu foil is depicted in **Figure 4.2d**. Three main bands can be observed at 1580, 1350 cm^{-1} and 2710 related to G, D and 2D peaks respectively. The intensity ration between the 2D and G bands is 1.97 indicating high-quality graphene monolayer. The intensity ratio between the D and G peaks is 0.07 revealing low disorder in the obtained material. The spectral background observed for the graphene is caused by the copper substrate and can be removed by transferring the graphene to another surface.

Before the graphene transfer, the interdigitated electrodes with 10/10 μm electrode/gap structure are cleaned in UV-Ozone chamber for 10 min followed by submersion for 15 min sequentially in 10 mL of acetone, isopropanol and water. Finally, each chip is copiously washed with large amount of water and dried under the nitrogen flow. The cleaned IDE were modified with trimethoxyphenylsilane (TMPS, 300 μL of TMPS in 15 mL of ethanol) in a plastic falcon tube for 1 h. Afterwards, the electrodes are bathed for 15 min in ethanol to remove the excess of the silane compounds form the surface. Subsequently, the modified interfaces are nitrogen blow dried and stored under the vacuum. The chips are placed on a hot plate at 120 °C at ambient pressure for 2 hours to anneal the formed monolayer and provide complete removal of the solvents from the interface. After the surface modification by TMPS, the CVD graphene is transferred on the surface of the device using the wet-transfer process depicted in **Figure 4.3.** Briefly, a polymethyl methacrylate (PMMA) film of 200 nm in thickness is spin-coated onto the graphene/Cu foil and annealed at 110 °C with a very slow heating and cooling rate (1 °C min^{-1}) in order to prevent cracks in the graphene due to the difference of the thermal expansion coefficient between copper and graphene. The graphene on the back side of the Cu foil was removed by reactive ion etching (RIE) in O_2 plasma (50 W/100 mT/25 sccm/1 min). Copper foil etching was achieved in 0.2 M ammonium persulfate ($(NH_4)_2S_2O_8$) for 4 h and the floating PMMA/graphene sample was put in a DI water. This operation was repeated about 10 times in order to rinse the graphene from the etchant solution. Graphene transfer onto the IDE was achieved by submerging the IDE under the floating graphene/PMMA film. To remove traces of trapped water between graphene and IDE and to increase the adhesion of graphene to the IDE, the substrate was placed on a hot plate and annealed at 90 °C for 30 min using a slow heating and cooling rate (1 °C min^{-1}). The PMMA layer was effectively removed by UV/ozone cleaning at 28-35 mW cm^{-2} for 5 min followed by a hot acetone rinse (50 °C for 180 min).

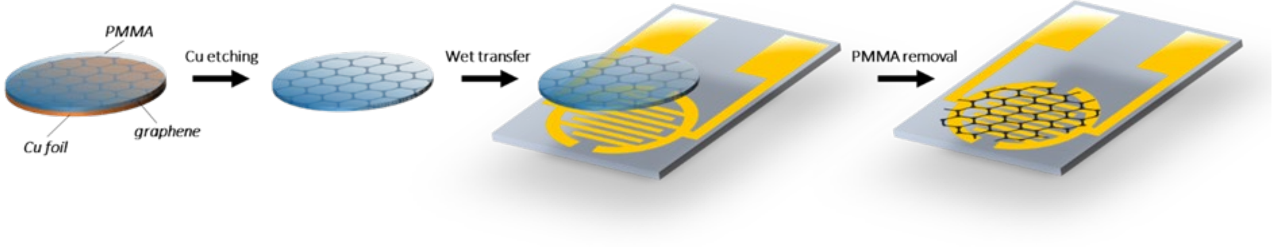

Figure 4.3: Process of deposition of CVD graphene on gold-based interdigitated electrodes. First the backside of the Cu substrate is plasma etched to remove the residual backside graphene, followed by copper foil etching in 0.2 M peroxydisulfate aqueous solution. The remaining floating graphene sheet, supported on a PMMA layer, is transferred to the chip and annealed for 30 min at 90 ºC. The PMMA is then removed in the final step in a hot acetone bath during 3 h.

Recording SEM images of the graphene coated IDEs before and after the wet transfer (**Figure 4.4a**) validates the complete coverage of the drain-source channel with graphene sheet with the quality of a monolayer graphene. XPS analysis of the C_{1s} core level spectrum (**Figure 4.4b**) is dominated by the band with binding energy BE=284.7 eV ascribed to the carbon in sp^2 hybridization state. Additional band with BE=285.0 eV is due to C-sp^3 components mostly present at the grain boundaries of the large graphene sheets and associated with edge functions such as C-O and C=O with higher BE=286.4 and 288.6 eV respectively. **Figure 4.4c** shows three-dimensional AFM image of IDEs covered with CVD graphene. In can be observed that the interface has a smooth homogeneous surface with the electrode's step height of 180 nm. The surface root mean square average (RMS) roughness, estimated from AFM image profile depicted in **Figure 4.4d**, is found around at approximately 1 nm. The low surface roughness is in line with an efficient removal of the PMMA protection layer.

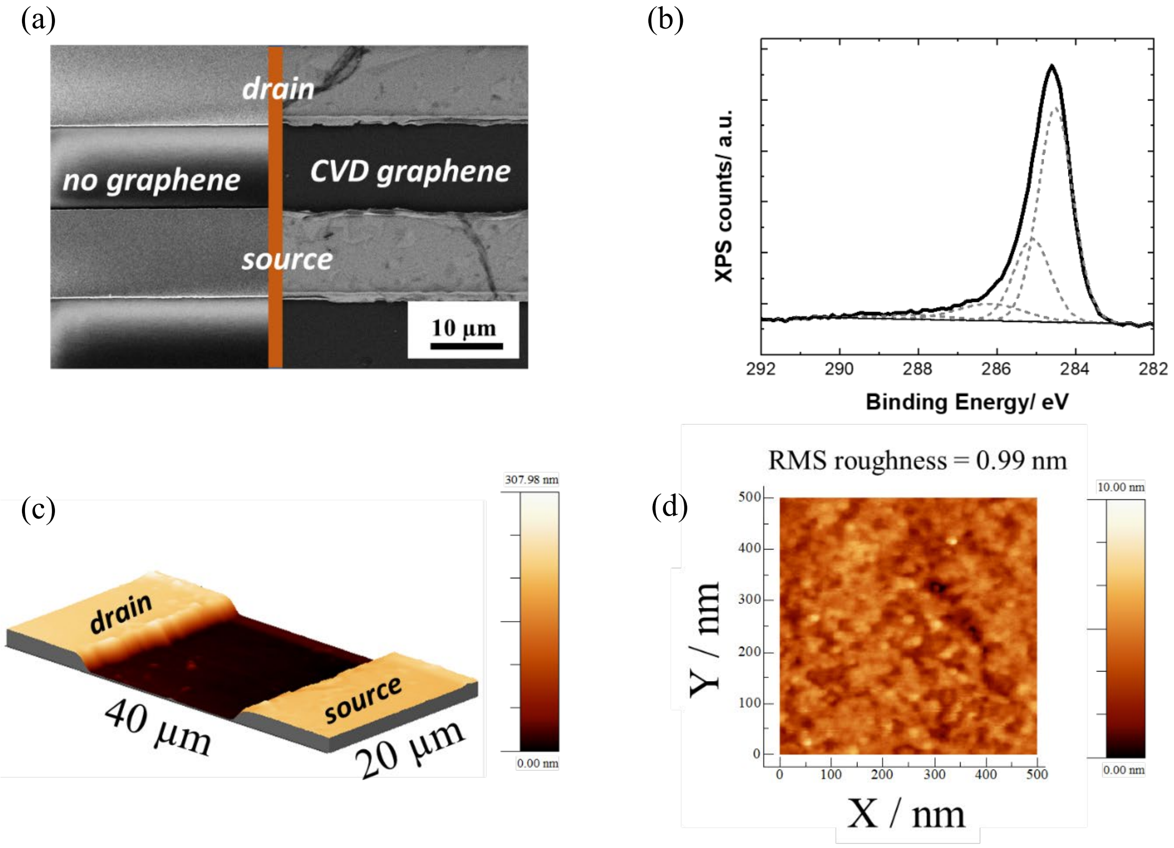

Figure 4.4: Surface characterization of unmodified CVD graphene-based FETs: (a) SEM image of CVD graphene coated IDEs showing full coverage of drain-source channel after the wet transfer and PMMA removal; (b) XPS C_{1s} core level spectrum of the graphene channel; (c) 3D AFM image on the IDEs covered with graphene; (d) 2D AFM image of the graphene channel.

In order to ensure the high-quality graphene monolayer with minor defects is obtained, Raman imaging was applied. First, the Raman spectra of 11×10 array data points with the lateral distance of 2 µm were recorded (**Figure 4.5a**). Raman spectra obtained from the four arbitrarily chosen points in the array (indicated with numbers 1-4 in **Figure 4.5a**) are demonstrated in **Figure 4.5b**. These spectra all show a signal at 1583 cm^{-1} (G band due to graphene sp^2 carbon) with low contributions at 1352 cm^{-1} (D band associated with the defects in the graphene lattice) and a dominant band 2704 cm^{-1} (2D secondary D band). The intensity ratio between the 2D and G bands are I_{2D}/I_G= 2.7±0.08. A $I_{2D}/I_G > 2$ with a $I_D/I_G < 0.35$ indicates high-quality graphene monolayer of low disorder. To illustrate the obtained results, the data set was converted to the images where each pixel represents I_{2D}/I_G and I_D/I_G ratios and shown in **Figure 4.5c** and **Figure 4.5d** respectively. It can be seen that the graphene covers the electrodes homogeneously with minor defects randomly distributed on the surface of device.

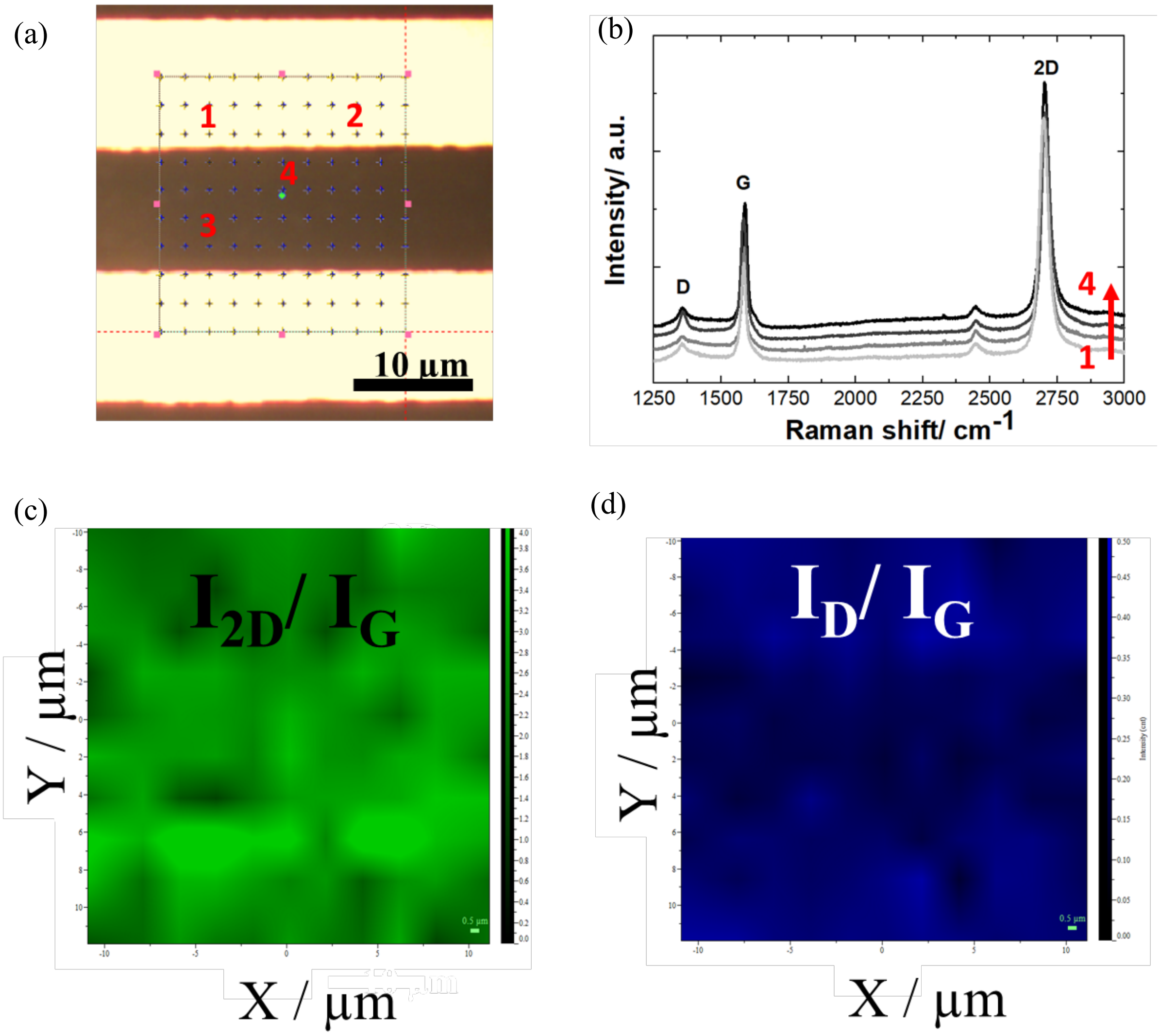

Figure 4.5: Raman analysis of CVD graphene-based FETs: (a) optical image of 11×10 data array with 2 µm spacing between the points where Raman spectra were recorded; (b) Raman spectra of four different points in the array (marked in Figure 4.5a); Raman images representing (c) I_{2D}/I_G and (d) I_D/I_G ratios.

4.3. Electrical properties of GFET

For the purpose of evaluating the electrochemically active surface area and measuring the transistor properties, the surface of IDEs was used as a working electrode for the electrochemical experiments and as the source-drain electrodes for the electrical measurements (**Figure 4.6a**). Both types of experiments were conducted in the cell depicted in the **Figure 3.4a** from the Chapter 3. **Figure 4.6b** inset summarizes the electrochemical behavior of a neutral redox species, 1mM ferrocene methanol in 1xPBS, on unmodified GFET with the different scan rates: 25, 50, 75, 100, 150 and 200 mV s^{-1}. The electrochemical surface area of the electrode was determined by plotting the peak current as a function of the square root of the scan rate (**Figure 4.6b**), according to:

$$A = \frac{slope}{268600\, n^{3/2}\, D^{1/2}\, C} \qquad Equation\ 4.1$$

where n is the number of electrons transferred in the redox event (n = 1), D is the diffusion coefficient of ferrocene methanol (7.5 × 10^{-6} cm^2 s^{-1}) and C is the concentration of ferrocene methanol (1 10^{-6} mol cm^{-3}). The experimentally determined slope (7.209 × 10^{-5} AV$^{1/2}$ s$^{-1/2}$) gives the active surfaces of 0.10 cm^2. The value is important for consideration and will be further used to quantify the number of redox species linked to the surface.

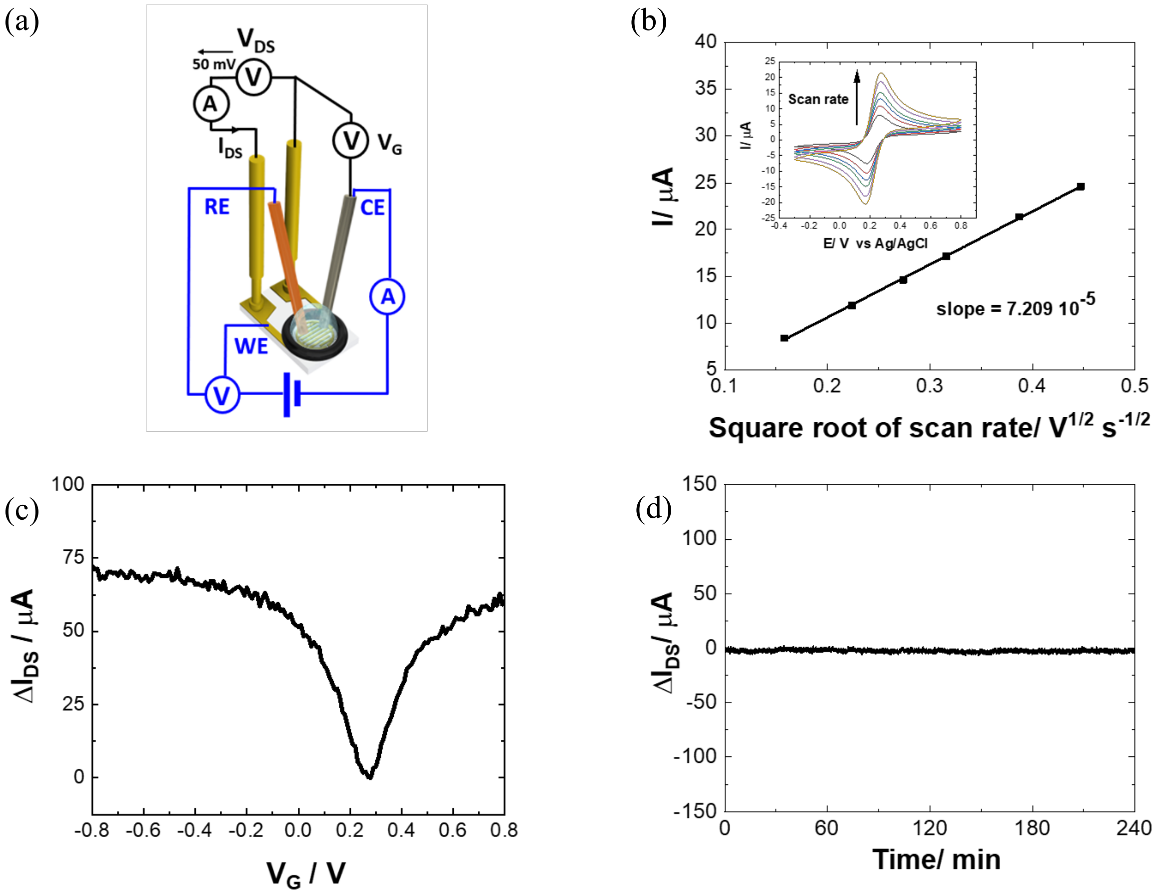

Figure 4.6: Electrochemical and electrical properties of GFETs: (a) electrical measurement setup (in black) to register the GFET readout in the liquid-gated configuration and electrochemical thee electrodes cell (in blue) to record CV and DPV experiments; (b) cyclic voltammograms recorded on GFET (inset) with 25, 50, 75, 100, 150 and 200 mV s^{-1} of scan rate using ferrocene methanol (1 mM)/1xPBS and the anodic peak current as a function of the square root of the scan rate; (c) $I_{DS}V_G$ characteristic of unmodified solution-gated GFET in 1xPBS medium with the source-drain potential of 50 mV; (d) $I_D(t)$ stability graph of the GFET transistor obtained in 1xPBS with the flow rate 50 µL min^{-1} and the gate voltage 200 mV.

In order to demonstrate the ambipolar transistor properties and calculate the mobility of charges, the source-drain current was recorded as a function of the gate potential (**Figure 4.6c**). The experiment was performed using 1xPBS as ionic medium with the flow rate 50 µL min^{-1} and applying 50 mV potential between the source and drain electrodes. From the linear fit of the slopes for p- and n-types of transistors (-253 and 264 µA V^{-1} respectively), the mobility of charges of 225 and 206 cm^2 V^{-1} s^{-1} were derived. The stability of interface was measured under the same conditions with the gate voltage fixed to 200 mV. The stability curve in the **Figure 4.6d** demonstrates a flat line where no current drift was observed. This superior electrical stability is beneficial for the biosensing experiments as no additional base-line correction is needed.

4.4. The effect of ionic strength and pH of the electrical properties of GFET

The effect of ionic strength on the GFET performance was evaluated by injecting the different concentrations of PBS (from 0.001x to 1xPBS by increasing the ion concentration by 10 folds) with 50 µL min^{-1} flow rate, 50 mV source-drain bias and -100 mV gate voltage. The obtained graph demonstrates the current response caused by the ionic strength of solution as a function of time (**Figure 4.7a)**. Despite the sequential injection of the increasing buffer concentrations, the response demonstrates an increase in drain current for 0.001x-0.01xPBS solutions and then decreases for 0.1x-1xPBS injections. This non-proportional to the ionic strength signal can be explained by recording $I_{DS}V_G$ curves corresponding to each injection (**Figure 4.7b)**. Fixing the vertical line on -100 mV of gate bias, it can be observed that the response current "direction" (to positive or negative drain current values) depends on two factors: the change in the $I_{DS}V_G$ curve shape and the position of the Dirac point. As it was demonstrated for rGO FET, the Dirac point depends on the ion concentration. With the increase of ionic strength, the neutrality point moves to the negative values (**Figure 4.7c)**. The value changes drastically for low concentrations and nearly saturates after 0.1xPBS. Along with this phenomenon, the slop of $I_{DS}V_G$ linear fit shows a similar reversed tendency: it sharply increases from 0.0001x-0.1xPBS and saturates for the higher values of ionic strength (**Figure 4.7c)**. As the steepest slope of $I_{DS}V_G$ curve is beneficial for electrical read-outs, the data suggest the optimal working conditions for biosensing at the concentrations higher than 0.01xPBS where the slope value is higher than at half saturation. This corresponds to 7.80 nm of Debye length acceptable for electrical sensing of big biomolecules.

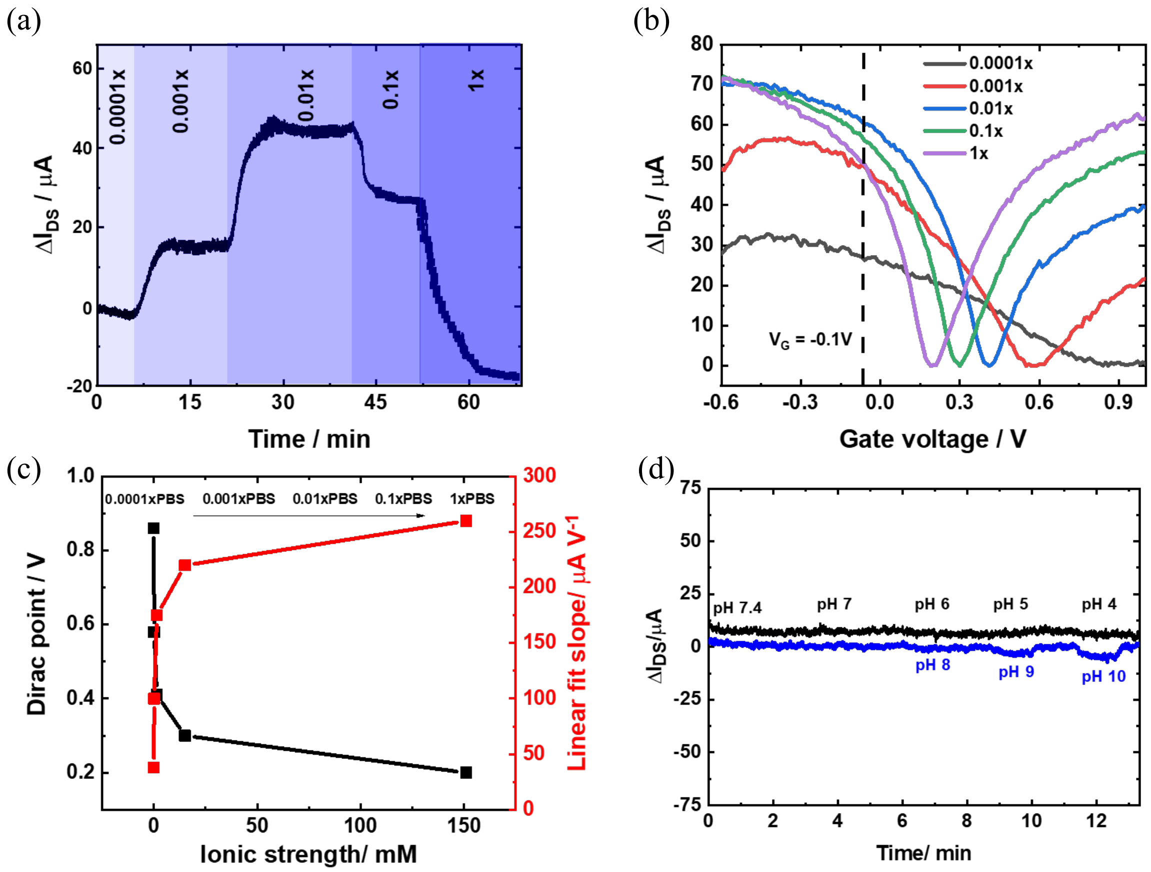

Figure 4.7: Ionic strength and pH sending on GFETs: (a) I_D(t) curve of unmodified GFET dependent of different PBS dilutions: 0.0001x, 0.001x, 0.01x, 0.1x and 1x corresponding to the ionic strength 0.015, 0.15, 1.51, 15.1 and 151 mM respectively, gate voltage -100 mV vs Ag/AgCl, flow rate 50 µL min^{-1}; (b) $I_{DS}V_G$ curves recorded during the injection of corresponding PBS concentration; (c) Dirac point and the slope of linear fit as a function of ionic strength; (d) GFET I_D(t) sensogram obtained by introducing different pH solutions, gate voltage 100 mV vs Ag/AgCl and the flow rate 50 µL min^{-1}.

To measure the source-drain current as a function of pH change, the solutions with different pH values were injected. The solutions with pH from 4-10 were prepared in 1xPBS as described in the Chapter 3. The gate voltage was defined as 100 mV as the slope for p-type transistor is the steepest. Then the solutions were injected on the GFET surface with the flow rate of 50 µL min^{-1} for 1.5 min following 1.5 min washing step with 1xPBS between each pH solution. The current change as a function of time is shown in **Figure 4.7d**. In contrast to rGO FETs, GFETs have low sensitivity to pH change in the medium. The CVD graphene-based transistor shows no signal to acidic solutions (pH 4-7) and a little response to the bases (pH 8-10). As the structure of CVD graphene has no functional groups in the basal plane and very few of them on the edges, the H$^+$ or

OH^- ion exchange occurs less evident compared to rGO. The small response to pH higher than 9 can be neglected as the bio-samples have generally pH around 7. This is beneficial for the biosensing as variation in pH of real biological samples will not interfere with the electrical signal caused by surface charge reorganization induced by ligand-analyte interactions.

4.5. Covalent modification of GFET interfaces using diazonium chemistry

As reported in the Chapter 2, the graphene-based interfaces can be covalently modified using diazonium electrografting technique where $-N^+{\equiv}N$ group is directly reduced on the surface of electrode and eliminated as a neutral molecule along with the radical formation and attachment to the graphene lattice changing carbon hybridization state from sp^2 to sp^3. We thus opted for the electrochemical grafting of a triisopropylsilyl protected ethynylphenyl diazonium salt, 4-[(triisopropylsilyl)ethynyl]benzenediazonium tetrafluoroborate (TIPS-Eth-ArN_2^+), known for its surface limiting grafting capabilities due to the presence of the bulky triisopropylsilyl (TIPS) group (**Figure 4.8a**). Cyclic voltammetry is a powerful technique to monitor *in situ* electron-transfer processes during the electrochemical reactions. A broad monoelectronic cathodic peak is observed at -0.2 V (vs. Ag/AgCl) by scanning the potential from +0.2 V to -0.6 V (vs. Ag/AgCl) at a scan rate of 50 mV s^{-1} (**Figure 4.8b**). This peak, present only in the first scan, is ascribed to the grafting of the aryl diazonium to the basal plane of graphene. The electrochemical reduction current of TIPS-Eth-ArN_2^+ at -0.2 V decreases already after the first cycle, indicating a successful surface anchoring to the graphene channel. The success of the surface grafting was additionally validated by XPS analysis (**Figure 4.8c**). The change in the C_{1s} core level of 4-(tri(isopropyl)silyl)ethynylphenyl (TIPS-Eth-Ar) modified GFET (**Figure 4.8c**) compared to unmodified GFET (**Figure 4.4b**) is in line with a change in the chemical environment after graphene functionalization. After TIPS-Eth-Ar grafting, the presence of the bulky TIPS groups is confirmed by the presence of Si-C band at 283.7 eV. An increase in the intensity of the C-sp^2 component is ascribed to the contribution of C-sp^2 signal from the carbon atoms of the phenyl rings of the diazonium salt. The highly reactive nature of aryl radicals' results, in most cases, in the formation of disordered polyaryl layers, which in the case of field-effect transistors will reduce the dynamic range of sensing as it might be as thick as the Debye screening length. The use of the bulky TIPS-Eth-ArN_2^+ precursor limits the surface modification to a functional monolayer.[65, 81] An increase in surface roughness to 1.87 nm was determined by AFM measurements (**Figure 4.8d**). With a theoretical height of 4-[(triisopropylsilyl)ethynyl]benzene of 1.01 nm,[81] the coating thickness is in agreement with a controlled surface grafting of the 4-

[(triisopropylsilyl)ethynyl]benzene radical on graphene and the prevention of the formation of multilayer branched structures. The success of the integration of TIPS-Eth-ArN_2^+ onto graphene

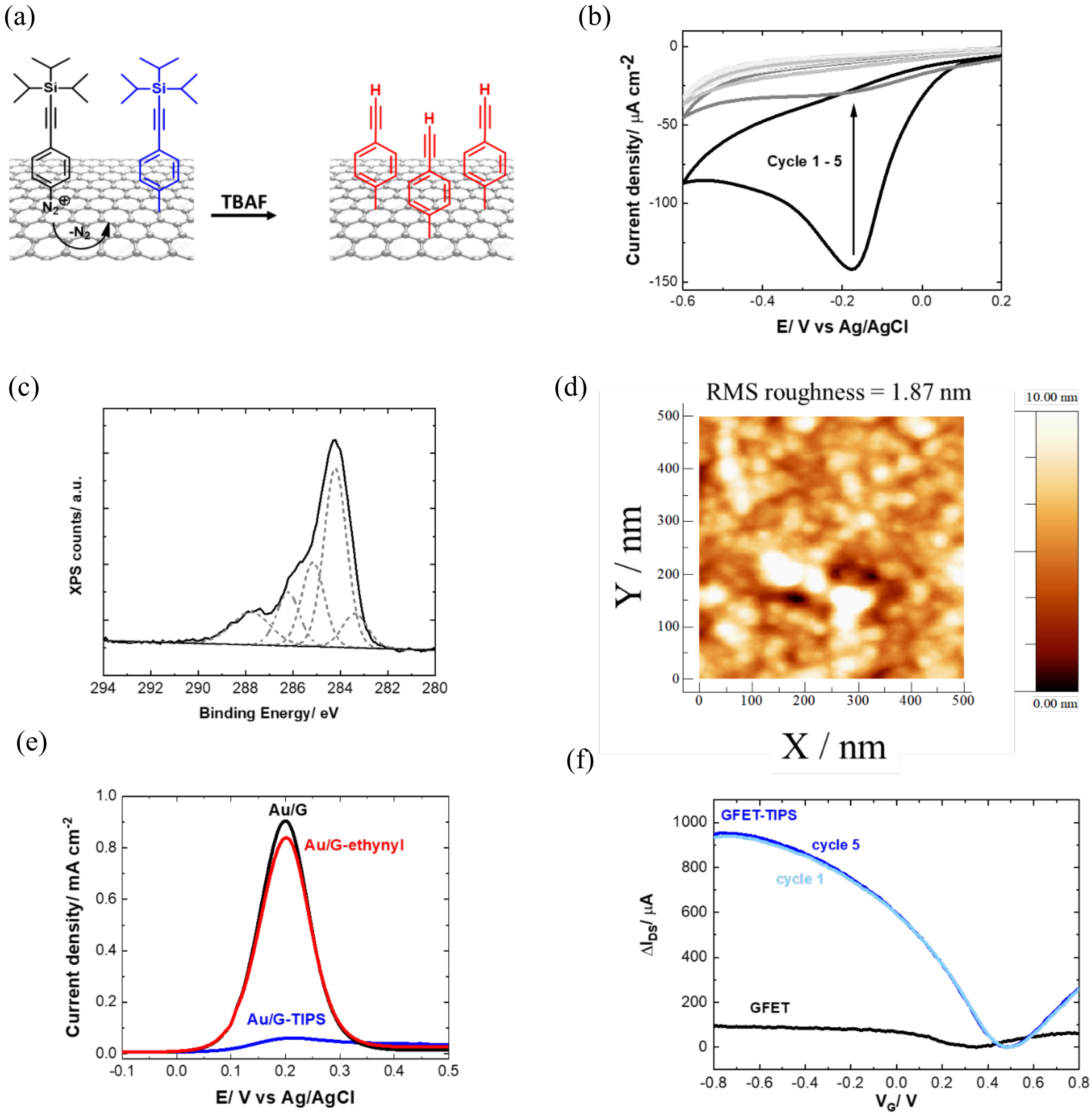

Figure 4.8: Electrografting of the diazonium salts on GFET and surface characterization: (a) electrochemical driven anchoring of 4-[(triisopropylsilyl)ethylenyl]benzenediazonium tetrafluoroborate diazonium salt, followed by chemical deprotection forming alkynyl-terminated GFET devices; (b) electrochemical reduction of a solution of TIPS-Eth-ArN_2^+ (5 mM) in 0.1 M n-tetrabutylammonium hexafluorophosphate (NBu_4PF_6) in acetonitrile *via* cycling between +0.2 V and -0.6 V (Ag/AgCl) at a scan rate of 50 mV s^{-1}. Reduction peak is visible at approximately -0.2 V vs. Ag/AgCl; (c) XPS C_{1s} core level spectrum and (d) AFM image of the GFET-TIPS channel; (e) Differential pulse voltammograms of ferrocenemethanol (1mM/ 1xPBS) on GFET (black), GFET-TIPS (blue) and GFET-TIPS after the deprotection (red); (f) transfer characteristics of GFET before and after modification with TIPS-Eth-ArN_2^+ for several cycles.

in one scan is further confirmed by the differential pulse voltammograms of ferrocenemethanol (1 mM/1xPBS) on GFET and GFET-TIPS (**Figure 4.8e**), whereas a strong signal is detected onto GFET, a complete blocking of the electron transfer from ferrocenemethanol to GFET-TIPS is observed.

Interestingly, the covalent surface modification results in strongly improved $I_{DS}V_G$ curve characteristics (**Figure 4.8f**) with slopes as steep as ~ 1750 µA V^{-1} observing a change on the hole mobility, μ_h, and electron mobility, μ_e, to 1240 and 1180 $cm^2 V^{-1} s^{-1}$, respectively, after TIPS-Eth-ArN_2^+ monolayer formation, which represents an increase by a factor of 5 in the effective mobility of our devices. One cycle is enough to achieve this mobility increase and the following cycles do not alter the overall behavior. The Dirac point shifted from +0.3 V (vs. Ag/AgCl) to +0.5 V (vs. Ag/AgCl) for GFET-TIPS. The change of the Dirac point to more positive values is in line with p-doping effect of the latter one. In order to confirm the p-doping effect and demonstrate an increase of defects in the graphene structure, Raman spectroscopy was applied. Comparison of the Raman spectra of transferred CVD graphene before (**Figure 4.5b**) and after electrografting (**Figure 4.9a**) of TIPS-Eth-ArN_2^+ indicates an increase in the ratio between D and G band intensity. The D peak is attributed to the transition from sp^2 to sp^3 hybridization of the graphene carbon atoms. It is an indication of the degree of covalent modification of graphene and as expected the I_D/I_G ratio increased from 0.35 (GFET) to 0.49 (GFET-TIPS), which demonstrates an increase in the disorder in the graphene lattice due to the covalent modification. Nevertheless I_{2D}/I_G ratio remains close to 2 indicating conservation of high-quality graphene monolayer. To visualize the obtained data, Raman imaging was carried out under the identical conditions described for the unmodified GFET. Raman images in **Figure 4.9b-c** show the conservation of homogeneity in the graphene layer with uniform increase in defects. Scatter plots of the Raman peak parameters for GFET and GFET-TIPS is shown in **Figure 4.9c**. The G and 2D peak positions (ω_G and ω_{2D}) are plotted against each other together with comparison data indicated by the arrow to distinguish p-doping trend. After functionalization, graphene Raman bands are further along the p-doping branch. The p-doping after the grafting has contributions from the covalent bond formation and electron withdrawing nature of TIPS-Eth-Ar substituent.

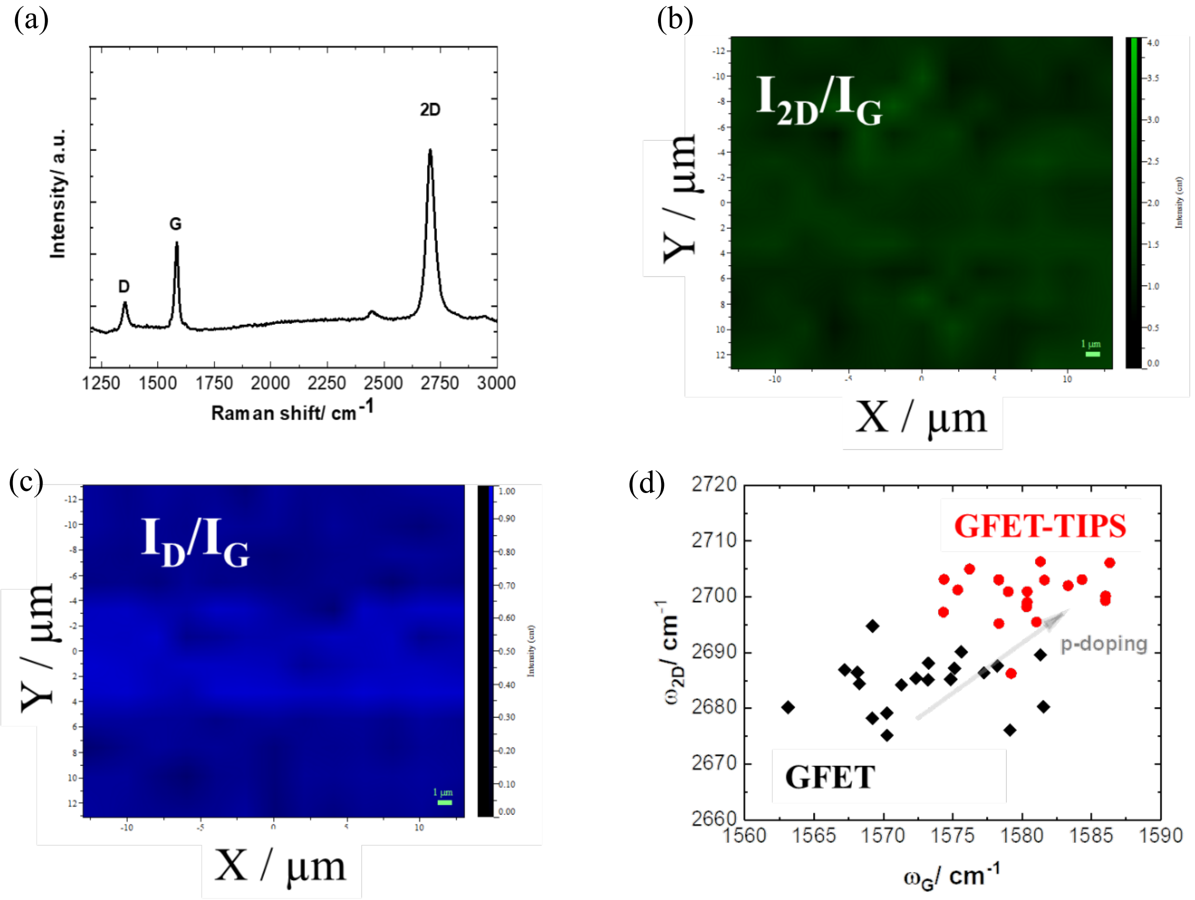

Figure 4.9: Raman spectroscopy on GFET-TIPS interfaces: (a) Raman spectrum of GFET-TIPS; Raman imaging of TIPS-modified interface representing (b) I_{2D}/I_G and (c) I_D/I_G peak intensity ratio; (d) scatter plot of Raman peak parameters with data points adapted from unmodified GFET and after the diazonium surface chemistry.

As a control experiment to ensure that applied electrical potential during the diazonium reduction does not alter the transistor properties, the surface of unmodified GET was cycled in 0.1M $TBAPF_6$/ acetonitrile solution with the same potential window as during the grafting. The obtained $I_{DS}V_G$ characteristics for unmodified and electrochemically cycled interfaces are shown in **Figure 4.10a**. It can be observed than the electrochemical potential brings nearly no effect on the transistor properties. In order to prove the effect of diazonium grafting on the change of $I_{DS}V_G$ curves, 4-nitrobenzene diazonium tetrafluoroborate was used to perform the same experiment as with TIPS-Eth-ArN_2^+. The deposition occurred in alike manner with an intense cathodic peak present during the first cycle and decreasing with the further steps (**Figure 4.10b**). The 4-nitrobenzene diazonium grafting was validated by cyclic voltammetry in 1 mM solution of ferrocenemethanol in 1xPBS (**Figure 4.10c**). The data demonstrate a stepwise decrease of the electrochemical signal. This suggests decreasing of electron transfer rates to the working electrode surface due to growing multilayers on the graphene surface. A similar change in $I_{DS}V_G$ was observed: an increase in graphene mobility after the first cycle, decreasing however with consecutives scans due to the formation of multilayered branched structures (**Figure 4.10d**).

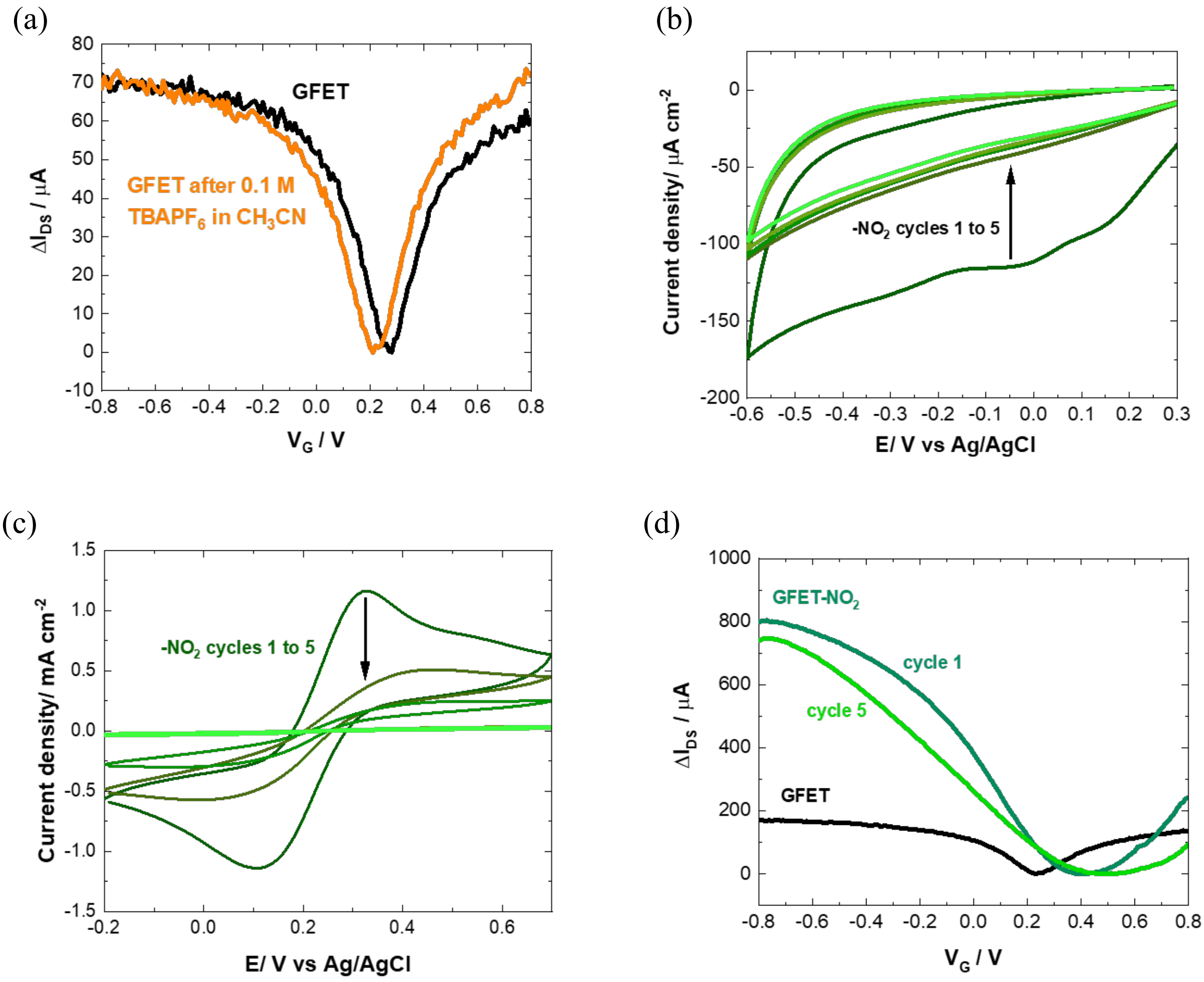

Figure 4.10: Control experiments of diazonium chemistry: (a) $I_{DS}V_G$ of GFET before (black) and after (orange) electrochemical cycling at scan rate of 50 mV s^{-1} in 0.1 M n-tetrabutylammonium hexafluorophosphate (NBu_4PF_6) in acetonitrile; (b) Electrochemical reduction of a solution of 4-nitrobenzene diazonium tetrafluoroborate (10 mM) in 0.1 M n-tetrabutylammonium hexafluorophosphate (NBu_4PF_6) in acetonitrile *via* cycling between +0.3 V and -0.6 V (vs. Ag/AgCl) at a scan rate of 50 mV s^{-1}. The reduction peak is visible at approximately -0.05 V vs. Ag/AgCl; (c) cyclic voltammograms of ferrocenemethanol (1mM/ 1xPBS) on GFET after each step of the electrochemical grafting of 4-nitrobenzene diazonium tetrafluoroborate; (d) $I_{DS}V_G$ of GFET-NO_2 after 1 and 5 cycles as compared to pristine GFET.

To have access to the alkynyl groups, the bulky TIPS protective groups were then removed by submersing the modified interfaces in 0.1 M TBAF/ THF solution for 1 hour (**Figure 4.11a**). The success of the TIPS cleavage was observed by recovering the DPV signal close to the bare GFET (**Figure 4.8e**). The cleavage of the TIPS group does not alter the transfer characteristics of the GFET as $I_{DS}V_G$ characteristics as well as the shape of the curve remain nearly unchanged

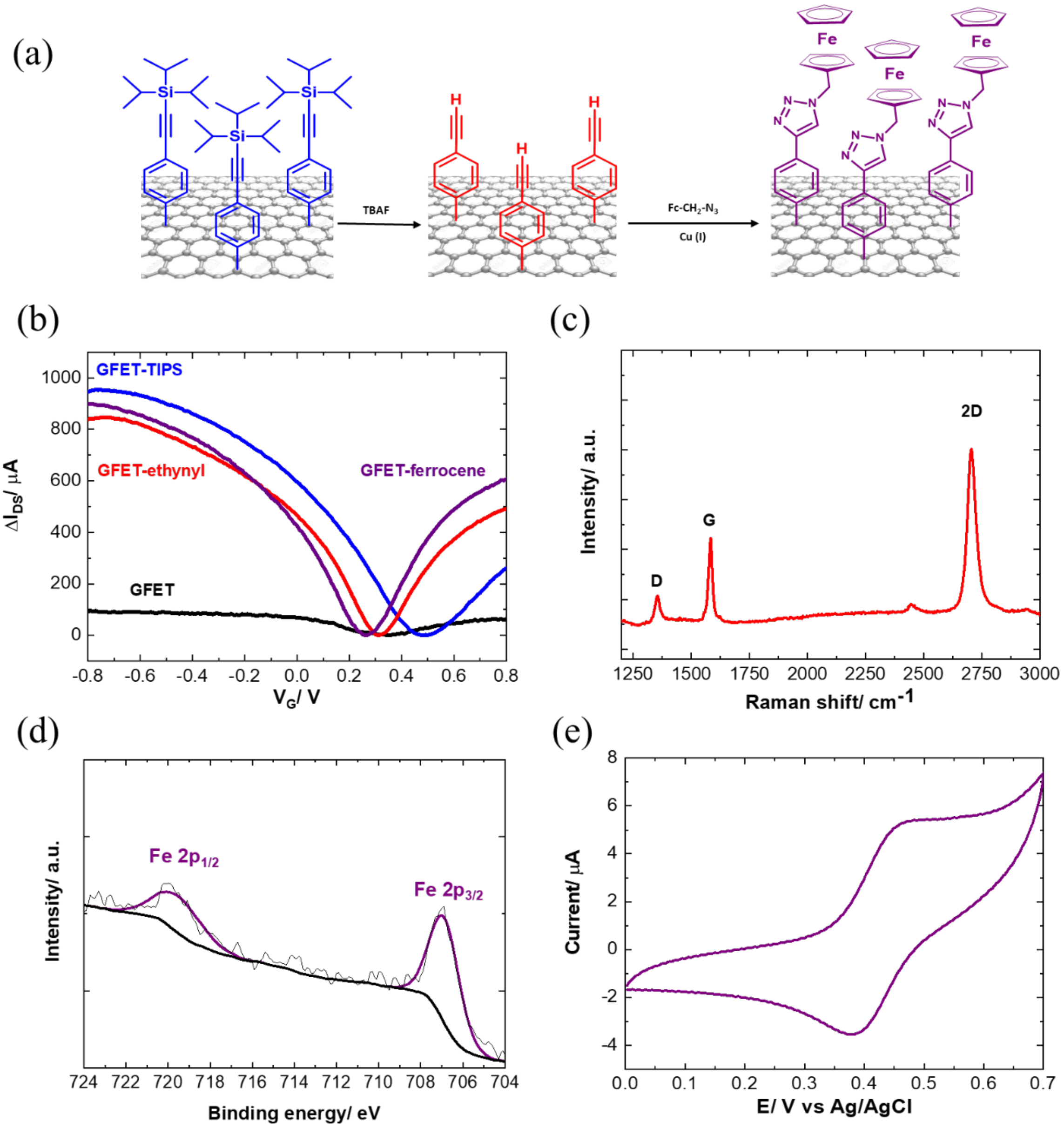

Figure 4.11: "Click" chemistry on the diazonium modified GFETs: (a) Formation of ethynyl-terminated GFET *via* deprotection of GFET-TIPS followed by integration of azide-terminated ferrocene through the Cu(I) "click" chemistry approach; (b) $I_{DS}V_G$ of GFET-ethynyl and GFET-ferrocene: (c) Raman spectrum of TIPS deprotected interface; (d) High resolution Fe_{2p} XPS core level spectrum of ferrocene-modified GFET interfaces; (e) Cyclic voltammogram of GFET-ferrocene in 0.1 M n-tetrabutylammonium hexafluorophosphate (NBu_4PF_6) in acetonitrile, scan rate = 100 mV s^{-1}.

(**Figure 4.11b**). The Dirac point shifted from +0.5 V back to +0.3 V after removal of the TIPS groups. Indeed, the formed ethynyl-terminated graphene channels with no particular electron donating or withdrawing group did not cause any obvious change in neither the *n* nor *p* type doping of the graphene. Raman spectrum of ethynyl-terminated device (**Figure 4.11c**) confirms no evident effect of the deprotection reaction on the graphene disorder, with comparable I_D/I_G ratio as for GFET-TIPS (**Figure 4.9a**), suggesting that the chemical treatment of the surface with TBAF only removed the TIPS groups without affecting the graphene structure.

The deprotected interface was further used for "click" chemistry reaction (Huisgen 1,3-dipolar cyclisation) with azidomethylferrocene (**Figure 4.11a**). The interface was submersed in 0.83 mM azidomethylferrocene in THF in the presence of an aqueous solution of $CuSO_4$ (10 mM) and L-ascorbic acid (20 mM) acting as a catalyst. The reaction time was 1 h under argon atmosphere. The surface was then treated with an aqueous solution of EDTA for 10 min to chelate any remaining Cu^{2+} residues and finally washed copiously with acetone and water and left for drying. The incorporation of ferrocene molecules onto the GFET surface is seen from the presence of the Fe_{2p} component in the XPS survey spectrum (**Figure 4.11d)**. The cyclic voltammogram of the ferrocene modified electrode examined in 0.1 M n-tetrabutylammonium hexafluorophosphate (NBu_4PF_6) in acetonitrile (**Figure 4.11e)**. A surface concentration of Γ=3.8 10^{-10} mol cm^{-2} of bound ferrocene groups was derived from these measurements using the **Equation 2.1** with previously defined the electrode surface area of 0.10 cm^2. The number of attached ferrocenyl groups here is determined (limited) by the size of the TIPS group which is bulkier than the size of ferrocene.[81] Considering the ferrocene molecules as spheres with a diameter of 6.6 Å, the theoretical maximum coverage for an idealized ferrocene monolayer can be estimated as Γ = 4.4 10^{-10} mol cm^{-2}. In our case, Γ = 3.8 10^{-10} mol cm^{-2} (86%) of the maximum surface coverage is achieved, in good agreement with previous observation and is close to the theoretical maximum coverage value.[81]

4.6. Field-effect transistors based on CVD graphene: are they better over rGO FETs?

There are two different graphene-based materials used in this work: reduced graphene oxide and chemically vapor deposited graphene. Though they share common chemical structure and have similar electrical properties, each of them has certain advantages and limitation in the biosensing field. The main characteristics are summarized in **Table 4.1**. The difference rises form the different approaches the material is obtained: top-down synthesis of GO using graphite and bottom-up process for CVD graphene. As it has been shown above, the graphene obtained from

CVD offers the highest quality material on a large scale. The basal honeycomb sp^2 lattices has no functional groups and usually consists of a monolayer making the CVD graphene-based transistors extremely stable and reproducible. On the other hand, because of the harsh conditions during the GO synthesis, the graphene flakes suffer from the presence of oxygen containing groups which usually cannot be completely removed after the reduction. The remaining functional groups in rGO structure can be used for the electrophoretic deposition or as a linker to directly attach bioreceptors. The graphite exfoliation also leads to the small graphene sheets with a size distribution. It is beneficial to use rGO due to a simple and fast deposition (e.g. EPD or drop casting) and cheap material cost.

Table 4.1: Comparison of CVD and rGO-based FETs.

	CVD GFET	rGO FET
Number of layers	Monolayer	Multilayers
Graphene flake size	Very large (> 1 cm)	Small (< 20 µm)
Surface	Homogeneous	Inhomogeneous
Manufacturing	Complex	Simple
Deposition technique	Wet transfer	Drop-casting
Commercial cost of graphene material	Expensive	Cheap
Oxygen containing groups and defects	Very low	High
Interface stability and reproducibility	Very high	Moderate
pH sensitivity	Very low	High
Ion sensitivity in FET configuration	High	High

In order to compare the electrical properties of rGO and CVD graphene covalently modified interfaces, the same TIPS-Eth-ArN_2^+ surface chemistry protocol was used on rGO FETs. The grafting on rGO surface occurs in the same manner as on CVD GFETs (**Figure 4.8a-b**). The electrochemical analysis after the modification confirms the success of complete surface graphing where no electron transfer takes place through the monolayer of TIPS-Eth-Ar (**Figure 4.12a**). In contrast to CVD GFET, the covalent surface modification on rGO FET does not result in improved $I_{DS}V_G$ curve (**Figure 4.12b)**. The shape of the curve after the modification is close to the initial one with a slight Dirac point shift to the positive values associated to p-doping effect on graphene. These data demonstrate better electrical properties of CVD graphene modified interfaces over rGO FETs making the modified GFET a promising transducer for the biosensing purposes. As a result, we opted covalent modification of CVD graphene surface for biosensing of cardiac biomarker Troponin I (cTnI).

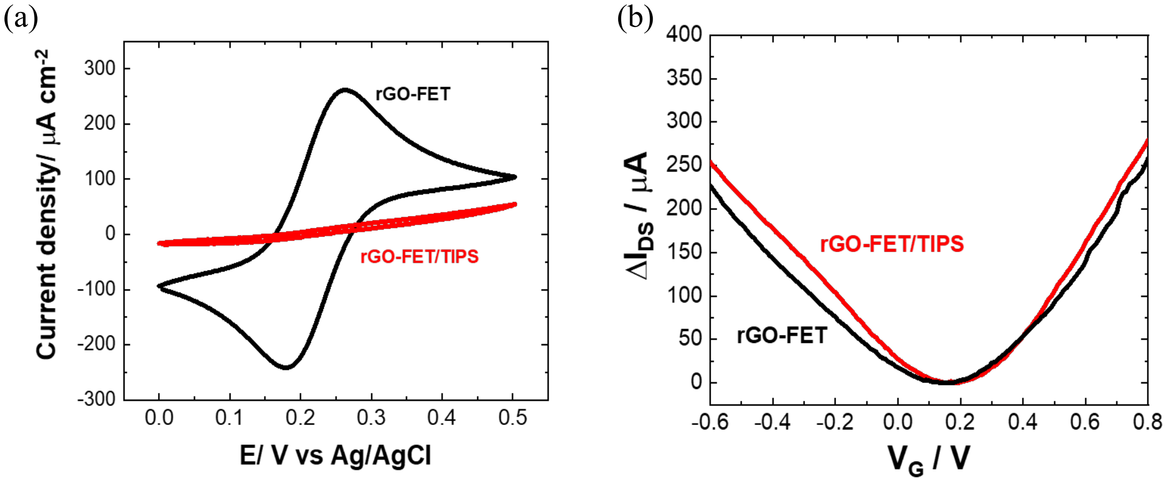

Figure 4.12: Electrochemical reduction of TIPS-Eth-ArN$_2^+$ on rGO FETs: (a) cyclic voltammograms of ferrocenemethanol (1mM/ 1xPBS) on rGO FET before (black) and after (red) the electrochemical grafting of TIPS-Eth-ArN$_2^+$, scan rate = 100 mV s^{-1}; (b) transfer characteristics in 1xPBS of rGO FET before (black) and after (red) modification with TIPS-Eth-ArN$_2^+$ for 5 cycles.

4.7. Sensing of cTnI biomarker on the covalently modified GFETs

In order to obtain cTnI specific biosensor, the surface of CVD graphene-based IDE was covalently modified with cTnI specific aptamer (**Figure 4.13a**). The aptamer was 5'-azide modified troponin I aptamer 5'-N$_3$-TTT-TTT-CGT GCA GTA CGC CAA CCT TTC TCA TGC GCT GCC CCT CTT A-3' adapted from the literature with K_D = 270 pM.[119] First, the graphene interface was grafted with 4-[(triisopropylsilyl)ethylenyl]benzenediazonium tetrafluoroborate (TIPS-Eth-ArN$_2^+$) salt *via* electrochemical reduction as demonstrated above (**Figure 4.8a-b**). After the modification, the DPV signal of ferrocene methanol as redox mediator was strongly decreased in line with the grafting of the bulky triisopropylsilyl (TIPS) group on the electrode surface. Giving the access to the ethynyl functionalities by chemical deprotection of the TIPS groups in TBAF resulted in the partial recovery of the ferrocenemethanol signal in the DPV (**Figure 4.13b**). As it was discussed before, the diazonium surface chemistry leads to the improved transistor properties

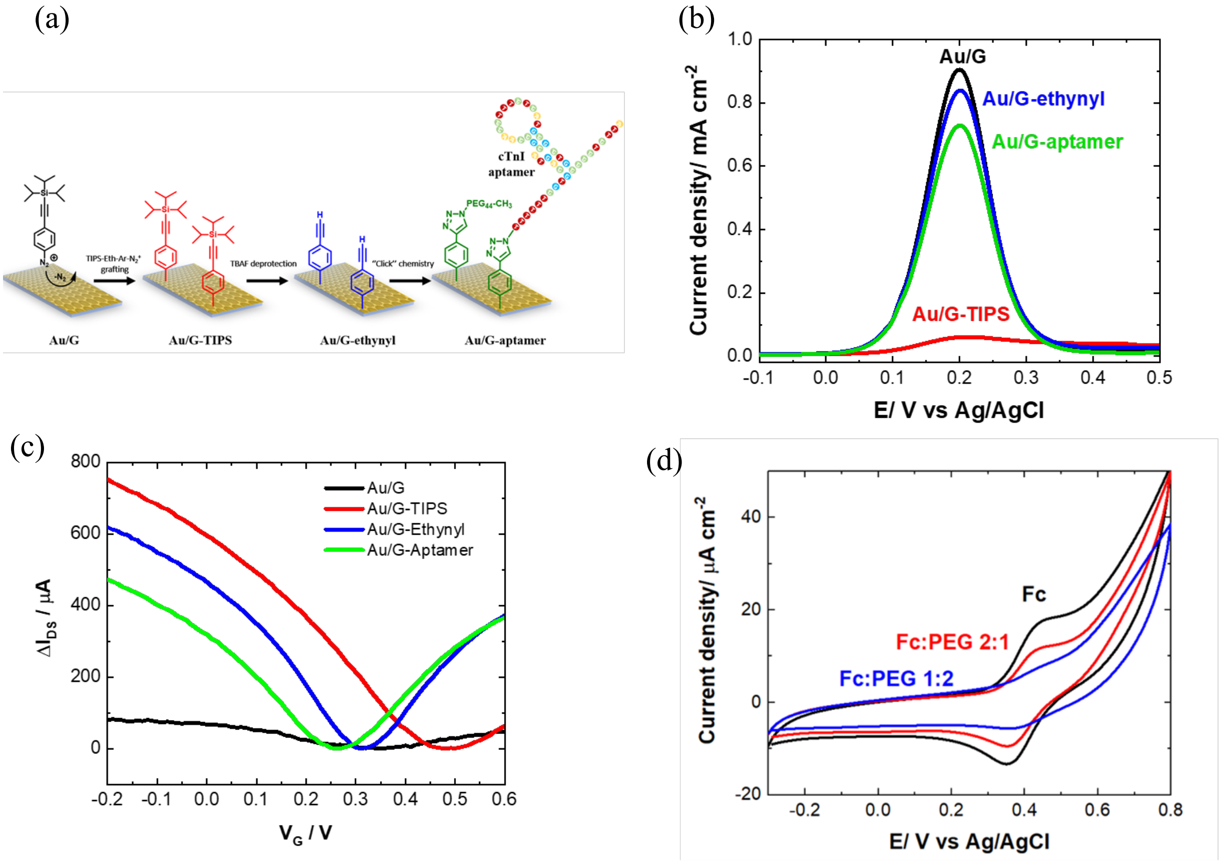

Figure 4.13: Covalent surface modification of CVD graphene-based transistors with cTnI aptamer: (a) formation of ethynyl-terminated electrodes (IDE/G-ethynyl) *via* electrochemical reduction of TIPS-Eth-ArN$_2^+$ forming Au/G-TIPS, followed by TIPS deprotection using TBAF. Immobilization of aptamer receptors using Cu(I)-catalyzed "click" chemistry; (b) Differential pulse voltammograms (DPV) of 1 mM ferrocenemethanol/ 1xPBS of bare graphene (Au/G in black), after TIPS-Eth-ArN$_2^+$ grafting (Au/G-TIPS in red), after 0.1 M TBAF cleavage of TIPS-protective groups (Au/G-ethynyl in blue), cTnI aptamer-modified interface (Au/G-aptamer in green); (c) $I_{DS}V_G$ characteristics in 0.01× PBS (pH 7.4) of Au /G (black), Au /G-TIPS (red), Au/G-ethynyl (blue) and Au /G-aptamer (green). Source drain bias is 50 mV; (d) Cyclic voltammograms (CV) of Au/G-ferrocene electrodes modified by "click" chemistry with N_3-ferrocene (Fc, 10 µM, black) and in the presence of N_3-terminated poly(ethylene glycol) (PEG) with Fc:PEG (ratio 2:1, red) and Fc:PEG (ratio 1:2, blue) in 0.1 M n-tetrabutylammonium hexafluorophosphate (NBu_4PF_6) in acetonitrile, scan rate = 100 mV s^{-1}.

demonstrated in **Figure 4.13c**. The transfer characteristics of the GFET (**Figure 4.13c**) as a function of the gate voltage (V_G) before and after electrografting of TIPS-Eth-ArN$_2^+$ revealed that electrochemical modification resulted in a positive shift of the Dirac point compared to the initial GFET, indicating a p-doping effect, with hole (μ_h) and electron (μ_e) mobilities reaching 1003 cm^2 V^{-1} s^{-1} and 829 cm^2 V^{-1} s^{-1}, respectively. Chemical deprotection of the TIPS group with tetrabutylammonium fluoride (TBAF) did not alter the transfer characteristics of the GFET, but shifted the Dirac point back to more negative values. "Clicking" ferrocene molecules onto the ethynyl-terminated GFET induced another negative shift of the Dirac point without altering the charge mobilities being μ_h = 1200 cm^2 V^{-1} s^{-1} and μ_e = 907 cm^2 V^{-1} s^{-1} which is important for a good sensing device. In order estimate the grafted density of the aptamer, cyclic voltammetry was used with ferrocene molecules linked to the surface as a model molecule due to its redox properties (**Figure 4.13d**). "Clicking" uniquely azidomethylferrocene (10 µM) to the ethynyl-terminated sensors results in the surface coverage of Γ= 5.9 ×10^{-11} mol cm^{-2} giving 13% of the maximum surface coverage estimated. As the bulky TIPS protective groups do not allow close packing of the ethynyl-terminated ligands on the graphene surface and the concentration of N_3-ferrocene was very low in analogous to N_3-aptemer, the surface coverage is not reaching the theoretical maximum. The ratio of the linked molecules can be controlled by diluting azidomethylferrocene with N_3-terminated poly(ethylene glycol) (PEG) in a mass ratio of 1:2 and 2:1 (aptamer/PEG). The ferrocene coverage of Γ= 3.0 ×10^{-11} mol cm^{-2} (ferrocene:PEG=2:1), and Γ= 1.02 ×10^{-11} mol cm^{-2} (ferrocene:PEG=1:2) were determined corresponding to 6 and 2% of the theoretical coverage respectively. The use of PEG chain is beneficial as anti-fouling agent to prevent non-specific adsorption of proteins to the graphene surface, but also as a molecule which increases Debye sensing length important for electric sensing. In consequence, we opted to use DNA:PEG=2:1 ratio in analogous to ferrocene:PEG integration. We expect that the interfaces modified only with the aptamer would have a higher concentration of the receptors on the interface, but not demonstrate the desired anti-fouling properties. Then the surface has reacted with the aptamer (10 µM)/PEG *via* Cu (I) catalyzed "click" chemistry under the same protocol as for ferrocene azide. The success of aptamer integration was further confirmed electrochemically by observing a decrease in DPV signal (**Figure 4.13b**) and electrically by shifting the Dirac point to negative values (**Figure 4.13c**).

The aptamer/PEG modified interfaces were further employed as GFET and assessed for their ability to convert the binding with cTnI into an electrical signal. The transfer characteristics in 0.01× PBS recorded after 10 min stabilization for each concentration of cTnI are presented in **Figure 4.14a**. No change in the shape of the $I_{DS}V_G$ curves was observed besides a negative shift in the Dirac point. With an estimated noise level of 1.22 µA and a $\Delta I_D/\Delta C_{cTnI}$ determined as 1.09 µA/pg mL^{-1}, a limit of detection equals to 3.3 ± 1.1 pg mL $^{-1}$ (S/N = 3) was recorded. A K_D = 54.9 pg mL^{-1} was extracted from Langmuir binding isotherm fit (**Figure 4.14b**). The value is in the same order of magnitude and comparable to other field-effect transistors reported so far.[122] However, the device's response is highly dependent on the ionic strength of the solution due to Debye screening effects (**Figure 4.14c**). Indeed, shifting from 0.01× PBS to 1 × PBS had a strong effect on the detected ΔI_D for each cTnI concentration. The electrical aptamer sensor featured good specificity for cTnI, allowing to differentiate another cardiac biomarker BNP-32 (**Figure 4.14b**).

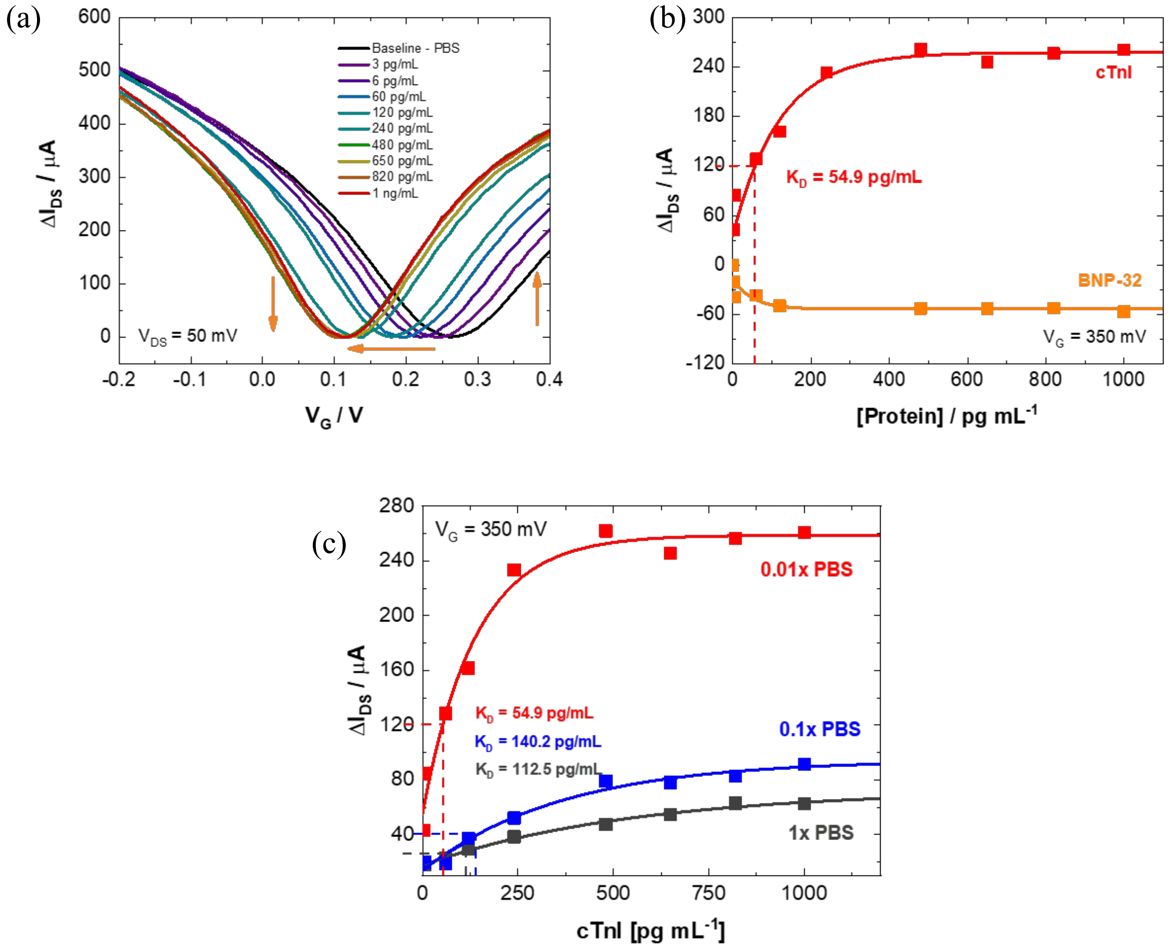

Figure 4.14: Sensing of cTnI biomarker: (a) Graphene transfer characteristics in 0.01× PBS (pH 7.4) without washing steps for different cTnI concentrations. Applied V_{DS} = 50 mV; (b) ΔI_{DS} for each cTnI concentration (red curve) and BNP-32 concentration (orange curve) at a fixed gate voltage V_G = 350 mV with respective Langmuir binding isotherm and estimated K_D; (c) Transfer characteristics for cTnI concentration in 0.01× PBS (pH 7.4) (black), 0.1× PBS (pH 7.4) (blue) and 1× PBS (pH 7.4) (grey), applied V_{DS} = 50 mV.

Compared to the other electrical sensing devices for cTnI reported so far, the values are coherent and in the same order of magnitude (**Table 4.2**). Up to date, this is the first cTnI biosensor utilizing not only GFET technology as a transducer but also covalent modification via the diazonium salt reduction on the graphene basal plane to link the bioreceptor and improve the device performance.

Table 4.2: Compilation of electrical aptasensors performances for the detection of cTnI.

Electrode architecture	**Method**	**Ligand attachement**	**LOD [pg mL^{-1}]**	**Linear range [ng mL^{-1}]**	**Ref**
CNN-GNPs/apta	ACEF	thiol	2400	2.4-2400	[123]
Si-NW/AzPTES/apta	FET	click	1000	1-1000	[124]
AlGaN/GaN/Au/apta	HEMT	thiol	6	0.006–148	[125]
IDE/G-aptamer	**GFET**	**“click”**	**3.3**	**0.003-0.15**	**This work**
AlGaN/GaN/Au/apta	HEMT	thiol	1	0.001-10	[126]

Si-NW: silicon nanowire; AzPTES: (3-azidopropyl)triethoxysilane; HEMT: high-electron-mobility transistor; ACEF: alternating current electrothermal flow; CNN: carbon nanotube network; GNPs: gold nanoparticles.

4.6. Conclusions

In summary, the manufacturing process of monolayer graphene FETs has been reported and discussed. The electrical and spectral characteristics have been demonstrated for unmodified devices to compare them with the once where the surface chemistry was applied. The influence of pH and ionic strength of the solution was highlighted and compared to rGO FETs. We found that the ionic strength conditions are optimal in 0.01xPBS for the electrical sensing corresponding to 7.80 nm of Debye length.

The CVD graphene interfaces were electrochemically grafted with 4-[(triisopropylsilyl)ethylenyl]benzenediazonium tetrafluoroborate diazonium salt to form a functional monolayer and the electrical and spectral characteristics were investigated and compared. The simple graphene modification occurs in one voltametric cycle enhancing the charge mobility compared to the bare GFET. The observed results can be explained as the aryl groups in close vicinity to the graphene plane act as short-range defect scattering centers “healing” the graphene edge defects. Raman spectroscopy data confirms the preservation of the high-quality graphene with only small defects brought by the surface modification. The improved electrical characteristics are conserved upon TIPS deprotection and after the “click” chemistry utilizing ethynyl groups and ferrocene azide as a model molecule. The surface coverage of ferrocene derivatives almost reaches the theoretical maximum. This paves the way for the enhanced biosensing applications, where the high slope in $I_{DS}V_G$ and its symmetrical shape allow the improved readout with an increased sensitivity.

Such highly suited GFET devices were covalently modified with cTnI aptamer/PEG in order to selectively detect this cardiac biomarker. The electrical sensing profiles was evaluated for cTnI in 0.01xPBS giving the limit of detection equals to 3.3 ± 1.1 pg mL $^{-1}$ and K_D = 54.9 pg mL^{-}

[1] in good agreement with the previously reported results and the clinically relevant cut off level. The observed diminution of the signal is directly correlated to the decrease of Debye sensing length.

Before proceeding, the results of the device manufacturing of CVD graphene-based liquid-gated field-effect transistors modified by 4-[(triisopropylsilyl)ethylenyl]benzenediazonium tetrafluoroborate diazonium salt and the biosensing of human cardiac biomarker cTnI are summarized in the attached publication, herein referred as [80] and [[122]] respectively:

Mishyn, V.; Rodrigues, T.; Leroux, Y.; Aspermair, P.; Happy, H.; Bintinger, J.; Kleber, C.; Boukherroub, R.; Knoll, W.; Szunerits, S. **Controlled Covalent Functionalization of Graphene-Channel of a Field Effect Transistor as Ideal Platform for (Bio) sensing Applications**. *Nanoscale Horiz* **2021**.

Mishyn, V.; Rodrigues, T.; Leroux, Y. R.; Butruille, L.; Woitrain, E.; Montaigne, D.; Aspermair, P.; Happy, H.; Knoll, W.; Boukherroub, R.; Szunerits, S**. Electrochemical and electronic detection of biomarkers in serum: a systematic comparison using aptamer-functionalized surfaces**. *Anal Bioanal Chem* **2021**.

Chapter 5: Pyrene-based ligands: systematic Raman studies and surface coverage using ferrocene derivatives

5.1. Introduction

While covalent functionalization has become by far the most promising approach for reaching robust and stable interfaces, this strategy causes the most significant change in the electric band structure of graphene due to the rehybridization of sp^2 carbons to sp^3 carbons not only on the graphene edges but also on the basal plane of the graphene lattice.[80] This has promoted the use of non-covalent modifications mainly replying on π-π stacking interactions of aromatic ligands to graphene with the obvious benefit that this approach retains the structures and electrical properties of the graphene. Because of the high protein absorption capability of graphene in a non-selective manner,[105] well-defined surface modification strategies have to be implemented to benefit from the excellent electrical and electrochemical properties of the devices for sensing of biomarkers in a selective manner. Surprisingly, while pyrene-based ligands are the most widely used graphene surface anchors for sensor related applications,[6, 26, 127] no systematic investigation on the reaction conditions has been employed and the influence of pyrene functionalities has not been reported so far. As these are the essential steps for efficient receptor integration and sensitive detection, by

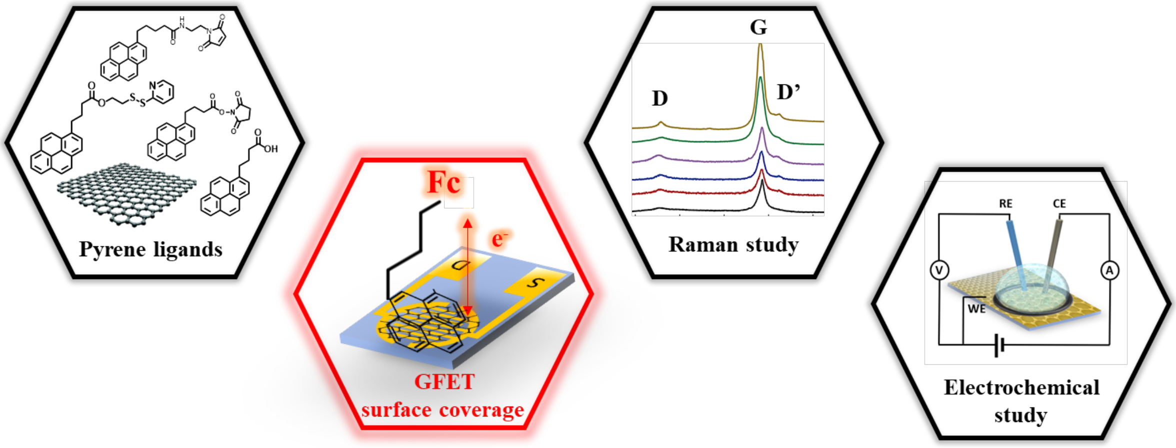

Figure 5.1: Non-covalent modification of graphene interfaces *via* π-π stacking: Different pyrene-based ligands used in this work for the modification of GFET devices; Raman investigation to optimize pyrene linkage conditions; electrochemical study of surface coverage using ferrocene derivatives as model ligands for post-functionalization.

utilizing Raman spectroscopy and electrochemical measurements we report here the optimized conditions for the surface modification as well as surface coverage using ferrocene derivatives as model compound to show that pyrene-maleimide and pyrene-conjugated dithiopyridine ligands attach ideally in the first 2h to graphene (**Figure 5.1**). We hope that this study will optimize and improve sensing performance of graphene-based devices.

5.2. Pyrene ligands and surface modification

The CVD graphene-based interfaces used in this study are the interdigitated gold electrode (IDE) arrays of 90 pairs, each with a width of 10 µm, and separated by 10 µm as used earlier in the Chapter 4 of this work. The reference Raman images of unmodified wet-transferred graphene showing the high-quality graphene channel are reported in **Figure 4.5a-c.** The interfaces were immersed in 5mM/ DMF solutions of pyrene-conjugated dithiopyridine (PSE), pyrene maleimide (PMAL), pyrenebutyric acid (PBA), pyrenebutanoic acid succinimidyl ester (PBASE) for 2, 4, 8, 12 and 24 hours following gentle washing step in DMF three time and nitrogen blow-drying (**Figure 5.2**).

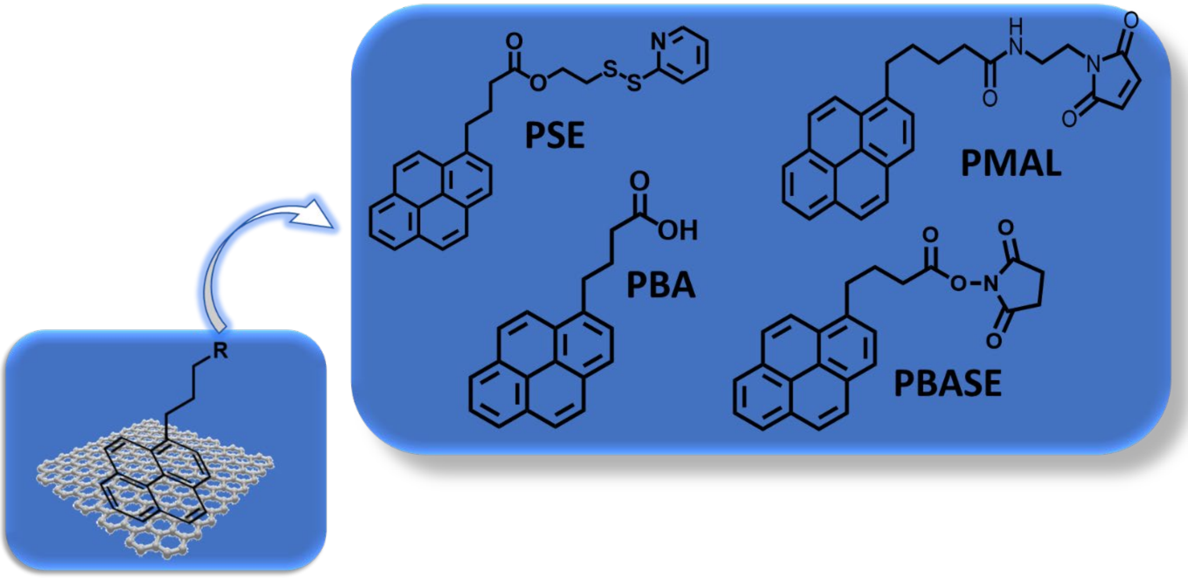

Figure 5.2: Different pyrene-based ligands for non-covalent modification of GFET interface: PSE: pyrene-conjugated dithiopyridine; PMAL: pyrene maleimide; PBA: pyrenebutyric acid; PBASE: pyrenebutanoic acid succinimidyl ester.

5.3. Modification with PBASE and PBA for amide coupling

1-pyrenebutanoic acid succinimidyl ester (PBASE) is the most widely used pyrene-based graphene ligand as it allows the coupling of molecules containing primary amines residues readily *via* the formation of amide bonds. Recorded Raman spectra of graphene coated interdigitated electrodes when immersed in PBASE for increasing times (**Figure 5.3a**) demonstrated the appearance of defect induced D' bands at 1620 cm^{-1} after 2h immersion, increasing with time.[128] The I_{2D}/I_G ratio (**Figure 5.3b**) gradually decreases approaching $I_{2D}/I_G < 2$ after 2h modification, with a I_{2D}/I_G approaching 1 after 6h pyrene/graphene interactions. Decrease of the I_{2D}/I_G ratio is associated with multilayer formation on graphene, where $I_{2D}/I_G = 1$ equal to a graphene bilayer.[129]

Aggregation of pyrene groups has taken place onto the monolayer graphene sheets due to π-π interactions, structurally similar to a bilayer graphene. It can be concluded that in order to avoid uncovered region but have limited defects, modification is optimal below the 6h time span using 5 mM PBASE in DMF.

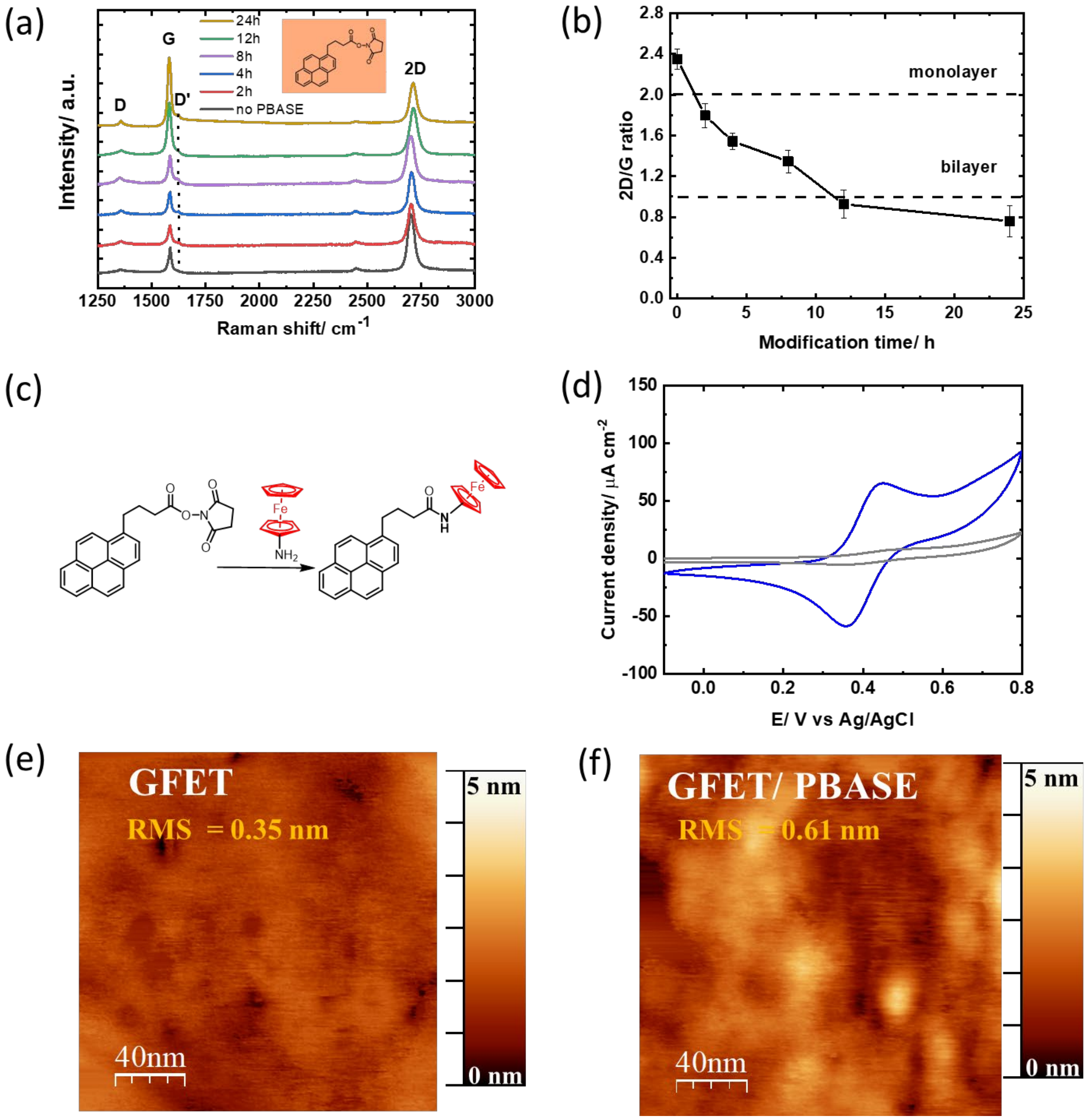

Figure 5.3: Surface characterization of interfaces modified with PBASE: (a) Raman images recorded at different time intervals (0, 2, 4, 8, 12 and 24 hours) upon immersion of GFET device into PBASE (5 mM, DMF); (b) I_{2D}/I_G ratio obtained from Fig. 5.3a as a function of modification time; (c) reaction scheme of PBASE with ferrocene-NH_2; (d) cyclic voltammograms of ferrocene modified GFET (4h) in acetonitrile/NBu_4PF_6 (0.1 M) (blue) and control experiment (grey): unmodified GFET device immersed in ferrocene-NH_2, scan rate=200 mV s^{-1}; (e) AFM image of GFET; (f) AFM image of GFET after PBASE modification for 4h.

To estimate the amount of receptor ligands which can be linked to PBASE modified GFEET at different time interfaces, post-treatment of the ester groups with ferrocene-amine (5mM)/ DMF for 4 hours was applied (**Figure 5.3c**). The success of ferrocene integration was observed by recording a cyclic voltammogram of the modified interfaces in acetonitrile/NBu_4PF_6 (0.1 M) conductive ionic medium **(Figure 5.3d** in blue). Approximating the size of pyrene molecule as a rectangular with 0.71 x 0.492 nm dimensions, the maximum possible pyrene surface coverage density is $\Gamma = 4.76 \times 10^{-10}$ mol cm^{-2}. The amount or redox species linked to the surface was derived using the **Equation 2.1** with the previously defined in the Chapter 4 electroactive surface of the electrode as 0.10 cm^2.

Table 5.1: Surface coverage of different pyrene-based ligands using ferrocene as a redox probe. Maximum possible surface coverage density is $\Gamma = 4.76 \times 10^{-10}$ mol cm^{-2} Approximating the size of pyrene molecule as a rectangular with 0.71 x 0.492 nm dimensions.

	Time/ h	Γ/ mol cm^{-2}
PBASE	2	$6.04 \pm 1.01 \times 10^{-11}$
	4	$6.44 \pm 1.52 \times 10^{-11}$
	6	$8.02 \pm 2.36 \times 10^{-13}$
	12	0
	24	0
PBA	2	$4.14 \pm 0.34 \times 10^{-10}$
	4	$4.11 \pm 0.52 \times 10^{-10}$
	6	$4.13 \pm 0.37 \times 10^{-10}$
	12	$4.17 \pm 0.29 \times 10^{-10}$
	24	$4.17 \pm 0.51 \times 10^{-10}$
PMAL	2	$4.18 \pm 0.25 \times 10^{-10}$
	4	$3.96 \pm 0.18 \times 10^{-10}$
	6	$1.77 \pm 0.28 \times 10^{-10}$
	12	$1.13 \pm 0.48 \times 10^{-10}$
	24	$1.11 \pm 0.33 \times 10^{-10}$
PSE	2	$4.30 \pm 1.20 \times 10^{-10}$
	2 (re-used)	$3.40 \pm 1.70 \times 10^{-10}$

In the case of 2-4h incubation times similar values of Γ=6.04 $\times10^{-11}$ and 6.44 $\times10^{-11}$ mol cm^{-2} were extracted respectively (**Table 5.1**) being two orders of magnitude larger compared to the ones when left of up to 6h. No ferrocene ligands were detected for 12 and 24h immersion times respectively. This indicates that the longer incubation times not only lead to the multilayer formation, but also results in hydrolyzation of the labile ester groups.

Aiming to estimate the effect of non-specific adsorption of ferrocene-NH_2 on the graphene surface, the unmodified graphene electrodes were immersed into ferrocene-amine (5mM)/ DMF solution for 4 hours as used before. The non-specific surface coverage of Γ=1.08 $\times10^{-11}$ was extracted (**Figure 5.3d** in grey). The background value caused by non-specific physical adsorption of aminoferrocene to the graphene basal plane is therefore negligible.

From the AFM images of unmodified graphene-coated electrodes (**Figure 5.3e**) and after 4h PBASE modification (**Figure 5.3f**), a root mean surface roughnesses of 0.35 and 0.61 nm were extracted respectively. The obtained increase in roughness is in agreement with the previously reported results.[130] The increase in the roughness indicates the formation of a dense pyrene layer after 4h, validating the hypothesis that the lower grafting density of ferrocene molecules is caused by the labile chemical nature of PBASE molecule rather than the pyrene stacks.

In order to elucidate the role of hydrolysis reaction of PBASE on the surface reactivity, the graphene channel was modified with 1-pyerebutyric acid (PBA) (5 mM)/ DMF with the same protocol as for PBASE. A similar to the PBASE trend was observed in Raman spectra of PBA modified interfaces (**Figure 5.4a**) with I_{2D}/I_G ratio (**Figure 5.4b**) decreasing below 2 after 2h modification and reaching a value below 1 after 24h of modification. The data suggest a similar non-specific pyrene multilayer formation when increasing incubation time is applied.

Then the carboxyl groups of PBA have been converted to succinimidyl ester *via* NHS/EDC protocol (**Figure 5.4c**) described in the literature.[26] This reaction converts PBA to PBASE where the carboxyl groups are freshly activated and the hydrolysis reaction is diminished. Then the reaction with ferrocene-NH_2 was carried out in the same manner as for PBASE-modified interfaces (**Figure 5.4c**) and the reaction was monitored by utilizing cyclic voltammetry in a conductive ionic medium of acetonitrile/NBu_4PF_6 (0.1 M) (**Figure 5.4d** in blue). Indeed, freshly activated PBA interfaces demonstrate as increased number of ferrocene molecules linked to the surface with Γ=4.14±0.34 × 10^{-10} mol cm^{-2} in 2h, reaching 4.17±0.51 × 10^{-10} mol cm^{-2} after 12h (**Table 5.1)**. The control experiment of non-specific adsorption of ferrocene-NH_2 on the graphene surface was performed identically as described above for PBASE (**Figure 5.4d** in grey). Interestingly, on the 4h-modified PBA interface immersed in ferrocene-NH$_2$ solution without NHS/EDC activation no ferrocene bound molecules were found as concluded by cyclic voltammetry (**Figure 5.4d** in black). This control experiments underline the lower surface coverage when succinimidyl of PBASE is hydrolyzed.

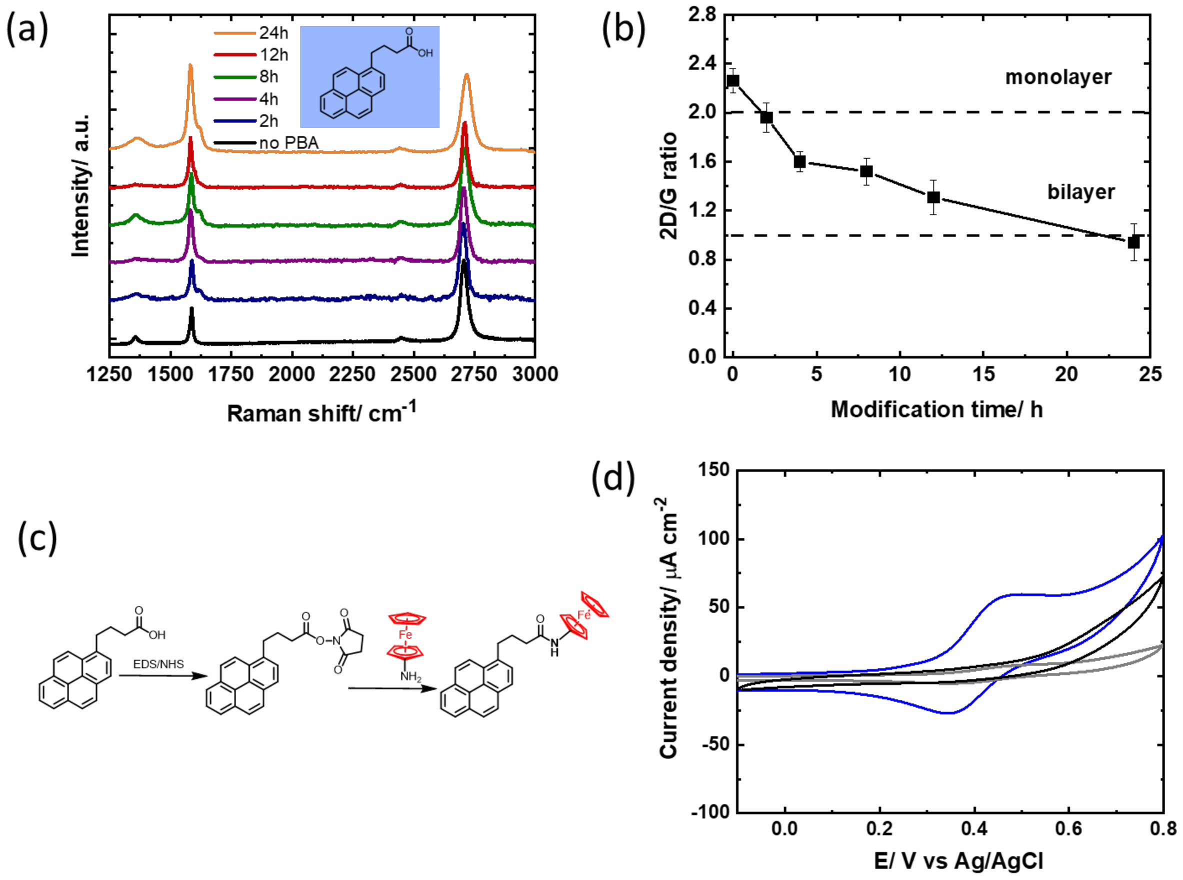

Figure 5.4: Surface characterization of interfaces modified with PBA: (a) Raman images recorded at different time intervals (0, 2, 4, 8, 12 and 24 hours) upon immersion of GFET device into PBA (5 mM, DMF); (b) I$_{2D}$/I$_G$ ratio obtained from Fig. 5.4a as a function of modification time; (c) reaction scheme of PBA activated *via* NHS/EDC protocol and coupling with ferrocene-NH$_2$; (d) cyclic voltammograms of ferrocene modified GFET (4h) (blue) and control experiments: upon immersion of GFET in ferrocene-NH$_2$ with no PBA on the interface (grey) and PBA modified interface immersed in ferrocene-NH$_2$ without NHS/EDC activation in acetonitrile/NBu$_4$PF$_6$ (0.1 M), scan rate=100 mV s^{-1}.

5.4. Modification with PMAL for thiol coupling

The interest of using PMAL instead of widely-used PBASE is that thiol carrying receptors can be linked to the graphene interfaces *via* thiol-maleimide chemistry.[131-133] In contrast to PBASE, Raman peak attributed to D' band rises on the interfaces with modification time longer than 12h (**Figure 5.5a**). Furthermore, the bilayer formation with $I_{2D}/I_G = 1$ is observed after 12h modification (**Figure 5.5b**). Longer modification time and formation of functional monolayer are explained due to the longer substituent chain of pyrene molecule. Chemical linkage of ferrocene thiol (5mM)/DMF for 4h (**Figure 5.5c**) followed by electrochemical investigation reveals a ferrocene coverage as high as $\Gamma=4.18\times 10^{-10}$ mol cm^{-2} after only 2h of PMAL incubation (**Figure 5.5d** in blue). This yields the surface coverage of more than 80%. This is due to the fact that the

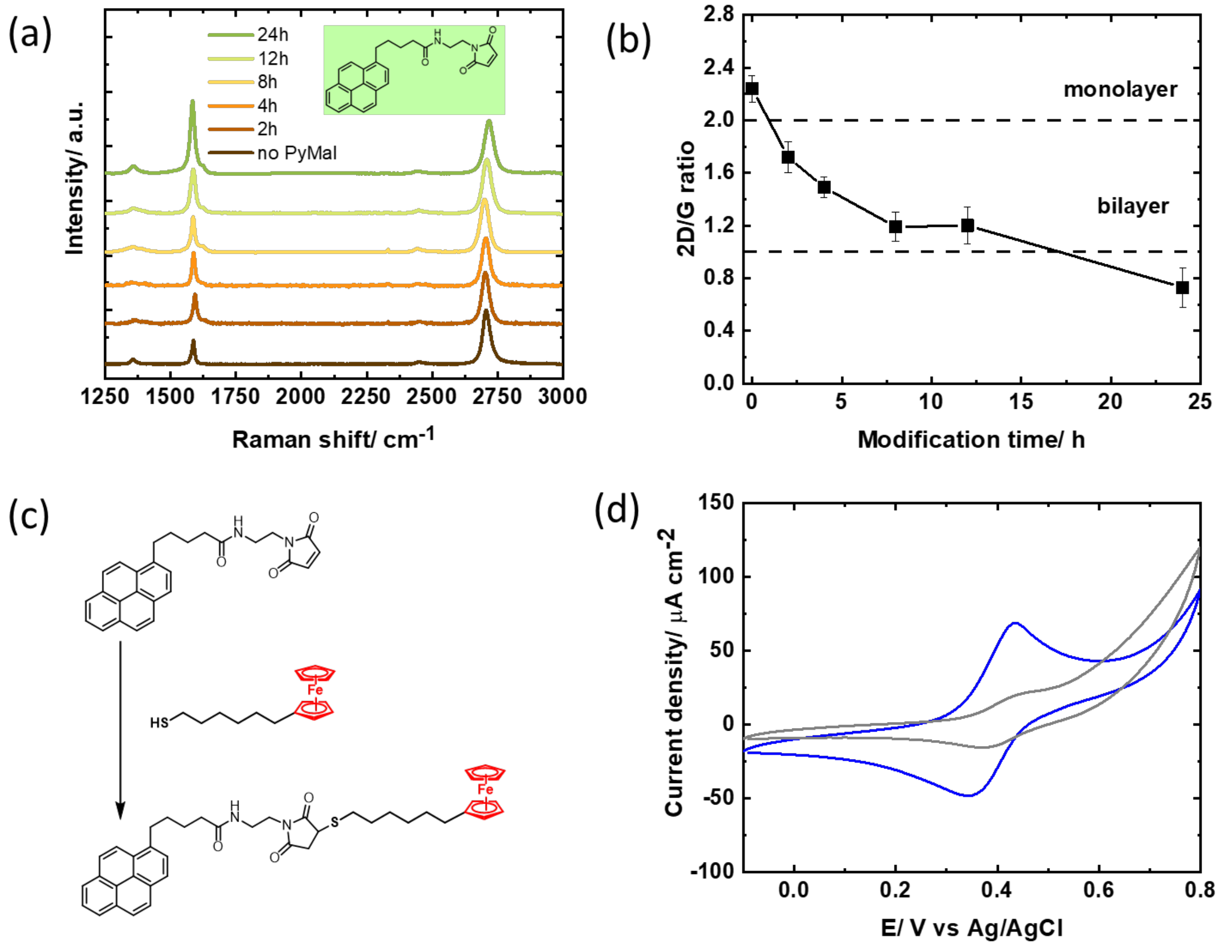

Figure 5.5: Surface characterization of interfaces modified with PMAL: (a) Raman images recorded at different time intervals (0, 2, 4, 8, 12 and 24 hours) upon immersion of GFET device into PMAL (5 mM, DMF); (c) I_{2D}/I_G ratio obtained from Fig. 5.5a as a function of modification time; (c) reaction scheme of PMAL with ferrocene-NH_2; (d) cyclic voltammograms of ferrocene modified GFET (4h) (blue) and control experiment with no PMAL on the interface (grey) in acetonitrile/NBu_4PF_6 (0.1 M), scan rate=100 mV s^{-1}.

maleimide groups are more stable against hydrolysis reaction and the reaction is overall more efficient. Longer incubation times result in decreasing the linkage efficiency (**Table 5.1**) due to the formation of multilayered structures of PMAL. As these layers have weak bounding, they can be easily washed from the surface reducing the efficiency of ferrocene integration. Moreover, the multilayered structures of PMAL increase the distance from the surface of electrode to the ferrocene molecule which reduces electron transfer efficiency during the electrochemical measurement. As thiol compounds can physically adsorb on the graphene and gold interfaces, the control experiment was carried by incubating the ferrocene thiol solution on unmodified graphene electrodes followed by electrochemical examination in acetonitrile/NBu_4PF_6 (0.1 M) solution (**Figure 5.5d** in grey). The data reveal minor signal of ferrocene molecules in the cyclic voltammogram occurring due to non-specific adhesion of the thiol-ferrocene derivative to the gold/graphene surface with $\Gamma=2.94\times 10^{-11}$ mol cm^{-2}.

5.5. Novel PSE ligand for reversible thiol coupling

A novel pyrene-based PSE surface ligand (**Figure 5.2**) with disulfide-based linker has been introduced by Sanyal et al.[134] Utilization of a disulfide-based linker as a surface ligand allows fabrication of specifically modified interfaces that incorporates a ‘catch and release’ reaction of a biorecognition element. As in case of PBASE, PBA and PMAL ligands, recording Raman spectra of graphene coated interfaces when immersed in PSE solution for increasing times (**Figure 5.6a**) demonstrate the appearance of defect induced D’ bands only at 1620 cm^{-1} after 4h immersion, increasing with time. Interestingly, the I_{2D}/I_G ratio associated to multilayer formation on graphene is decreasing slower than for the other ligands (**Figure 5.6b**), not leading to the multilayered structures even after 24h of incubation due to the longer chain of pyrene substituent and the presence of sterically large pyridyl disulfide group. As the formed layer of PSE molecules does not tend to form thick multilayers, this can be beneficial for the biosensing application as this allows to integrate biorecognition elements in a controlled manner with a very close proximity to the graphene interface. To validate the surface coverage chemical linkage of ferrocene thiol (5mM)/DMF for 4h was used (**Figure 5.6c**). The electrochemical analysis (**Figure 5.6d** in red) reveals ferrocene surface density equals to $\Gamma=4.3\pm1.2\times10^{-10}$ mol cm^{-2} after only 2h of PSE incubation. This is the highest surface coverage achieved among the investigated pyrene-ligands. Incubation of the ferrocene-modified interfaces attached to the graphene surface in dithiothreitol (DTT) and then in 2,2′-dithiodipyridine (2PDS) solutions leads to facile detachment from the interface (**Figure 5.6c**). Recording cyclic voltammogram in acetonitrile/NBu_4PF_6 (0.1 M) after the DDT/ 2PDS treatment confirms elimination of most ferrocene molecules from the surface (**Figure**

5.6d in black). The regenerated interface was used to re-link ferrocene molecules. Cyclic voltammogram of the recycled interface with the ferrocene re-linked molecules reveals a recovered signal close to the initial one (**Figure 5.6d** in blue). A slight decrease in the signal intensity ($\Gamma=3.4\pm1.7\times10^{-10}$ mol cm^{-2}) is explained due to the weak bond nature between the pyrene ligand and eventual molecules detachment during the washing steps.

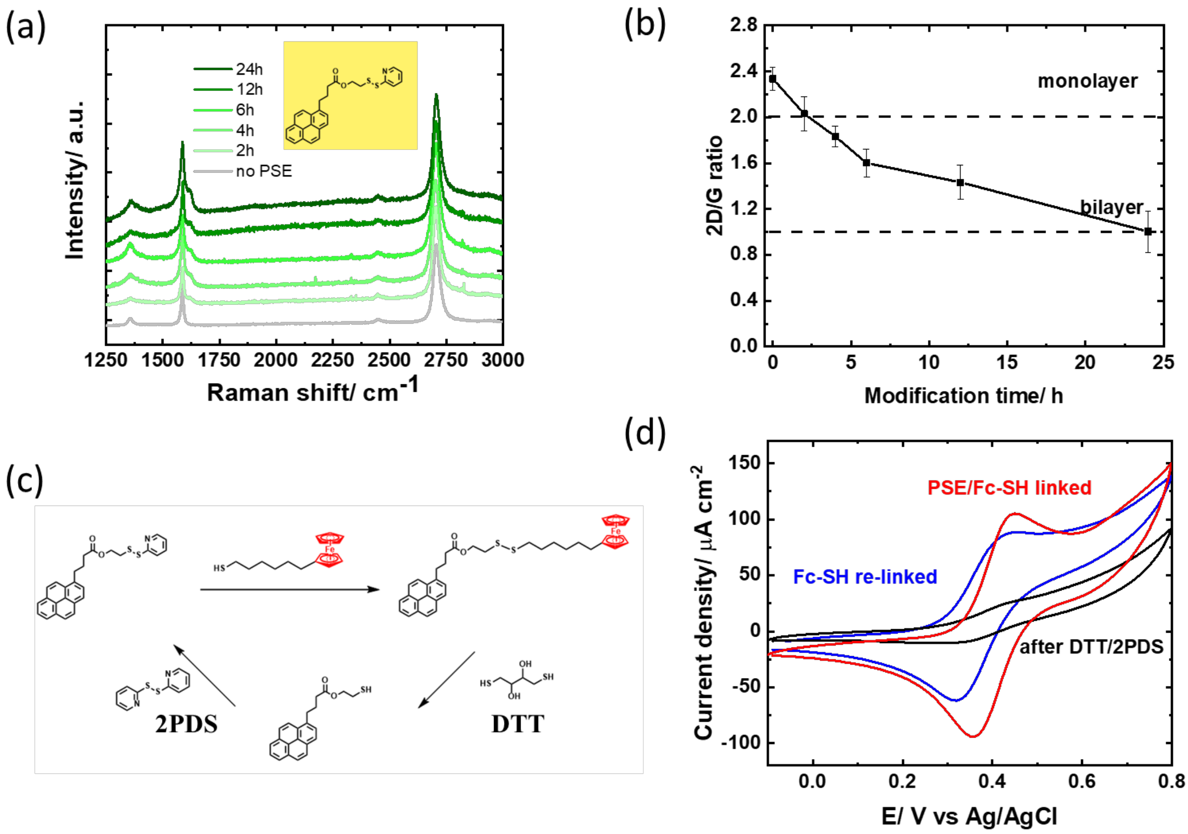

Figure 5.6: Surface characterization of interfaces modified with PSE: (a) Raman images recorded at different time intervals (0, 2, 4, 8, 12 and 24 hours) upon immersion of GFET device into PSE (5 mM, DMF); (c) I_{2D}/I_G ratio obtained from Fig. 5.6a as a function of modification time; (c) reaction scheme of PSE with ferrocene-SH showing the reversibility of the reaction; (d) cyclic voltammograms of initially modified ferrocene GFET (4h) (red), after surface regeneration (black) and re-attachment of ferrocene thiol (blue) in acetonitrile/NBu_4PF_6 (0.1 M), scan rate=100 mV s^{-1}.

5.6. Conclusions

In summary, four different pyrene-based ligands for non-covalent graphene modification have been investigated using Raman spectroscopy and electrochemical measurements using surface linked ferrocene molecules as a redox probe. We used two different kinds of reaction to link the ferrocene derivatives to the ligands: amide bond formation and thiol chemistry. The role and limitations of widely used ligands such as PBA and PBASE have been demonstrated and discussed. We found that long time modification with PBA and PBASE leads to multilayered structures on the graphene interfaces limiting post-functionalization strategies. Moreover, the importance of the hydrolysis reaction in PBASE has been showed and discussed. The AFM images and control experiments underline the obtained results.

Aiming to improve the surface coverage and limit the multilayered structures, PMAL surface ligand was introduced. The multilayer formation was observed only after 24h incubation due to the chemical structure of the ligand. The surface coverage has almost reached its theoretical maximum already after 2h of incubation suggesting the high reactivity of thiol-maleimide coupling and the efficiency of optimized conditions.

A novel pyrene-based PSE surface ligand with disulfide-based linker has been introduced as an alternative for thiol coupling. Because of the longer carbon chain between the pyrene and the sterically large pyridyl disulfide group, the I_{2D}/I_G ratio associated to multilayer formation on graphene was not leading to the multilayered even after 24h incubation time. Using the optimized conditions for PMAL, the thiol coupling with PSE ligand has yielded the ferrocene surface coverage close to the theoretical maximum value. The benefit of reaction reversibility was demonstrated.

The obtained results summarizing the role of the pyrene-based surface ligands on the sensitivity of graphene-based biosensors are summarized in a paper draft prepared for the submission:

Mishyn, V.; Hugo, A.; Rodrigues, T.; Aspermair, P.; Happy, H.; Bouchiat, V.; Boukherroub, R.; Knoll, W.; Szunerits, S. **The holy grail of pyrene-based surface ligands on the sensitivity of graphene-based field effect transistors.** *Sensors and Diagnostics*, submitted **2021**

General conclusions and perspectives

This thesis was focused on the development of graphene-based biosensors based on electrical and electrochemical read outs. Different graphene transfer protocols such as wet-chemical transfer of CVD graphene, drop-casting of chemically derived graphene such as reduced graphene oxide (rGO) in addition to electrophoretic deposition (EPD) of graphene oxide (GO) have been investigated and characterized by Raman and XPS spectroscopies, SEM and AFM imaging and electrochemical and electrical measurements. While the use and deposition of rGO and GO take advantage from being cost-effective and allowing to utilize the residual oxygen-containing functionalities for bioreceptor attachment, the devices based on CVD graphene have demonstrated excellent stability and reproducibility along with the possibility of robust chemical modification and are the preferred biosensing architecture.

Covalent and non-covalent strategies have been employed for post-functionalization with bioreceptors. First, the widely-used non-covalent π-π stacking modification was implemented in order to create rGO dopamine-modified β-cyclodextrin interfaces for electrochemical sensing of folic acid. We have demonstrated that coupling of β-CD onto an rGO-based integrated electrochemical system is a promising alternative for folic acid sensing with a detection limit of 1 nM. The linear response up to 10 μM allowed to distinguish healthy individuals as well as patients diagnosed with folic acid deficiency. Potential interference issues such as unrecorded metabolites/xenobiotics and other species have yet to be studied.

The same type of surface chemistry was used to create a liquid-gated rGO field-effect transistor for E7 protein of human papilloma virus detection. In our case, integration of HPV-16 E7–specific aptamer was achieved by covalent EDC/NHS coupling to rGO-FET pre-modified with 1-pyrenebutyric acid/pyrene-PEG in a ratio of 1:10. Monitoring the aptamer-protein binding in real time revealed preferential binding of HPV-16 E7 with a detection limit of about 100 pg mL^{-1} (1.75 nM) for HPV-16 E7 from five blank noise signals (95% confidence level). The dissociation constant K_D of the binding reaction was determined as 200 nM, consistent with previous reports of aptamer-protein binding reactions.

To elucidate the kinetics of multilayer formation of pyrene-based derivatives on a perfect graphene monolayer and evaluate its influence of the surface reactivity, four different pyrene ligands have been investigated. We found that short modification times are in general beneficial to avoid multilayered surfaces structures which are limiting the number of integrated species on the surface. Furthermore, the widely-used PBASE and PBA ligands have both different limitations. The ester of groups of PBASE are hydrolyzing readily resulting in inefficient post-functionalization. PBA forms pyrene pyramids at longer time and is not covering the entire graphene surface. This could result in non-specific absorption issues in sensors and will have also limited sensitivity for GFET sensing where the Debye length has an important influence on the sensing ability. We believe PBA, PMAL and PSE with short modification times to be ideal surface linkers for sensing based applications as they show full monolayer formation after 2h immersion and optimal post-functionalization strategies.

In order to validate the covalent modification strategy, a specially designed diazonium salt was first successfully electrochemically grafted to EPD rGO interfaces allowing to "click" ferroceneazide as a model molecule. The quantification of the linked species reveals the surface coverage value close to the theoretical maximum. Then the obtained ethynyl-terminated interfaces were covalently linked to cTnI aptamer via "click" chemistry to perform electrochemical sensing of cardiac biomarker cTnI. The obtained electrochemical aptasensor could differentiate the troponin I concentrations corresponding of healthy individuals from the once of patients in risk with the linear range from 1 pg mL^{-1} to 1 ng mL^{-1}.

Non-covalent surface modification strategies of GFETs are expected to be less compatible with long-term use of GFETs as required in sensing-based applications. To obtain stable and robust surfaces, chemical functionalization *via* covalent grafting is by far the most promising approach. Modification of GFETs in this manner without reducing the electrical characteristics remains a high challenge. It could be shown in this work that the use of ethynylphenyl monolayers formed *via* an electroreduction process as a surface linkage strategy for GFETs preserves GFET mobilities and even increases them. Under optimized conditions, formed alkynyl-terminated GFET keeps a charge mobility above 1000 cm^2 V^{-1} s^{-1} outperforming GFETs modified with other aryl diazonium salts, such as the well-known 4-nitrobenzene diazonium tetrafluoroborate. The preservation of the conductivity of the graphene sheet and its charge mobility together with the possibility to integrate ligands further via "click" chemistry are large steps further to the development of highly sensitive sensing interfaces. This was exemplified for the detection of the cardiac biomarker cTnI with a limit of detection equals to 3.3 pg mL^{-1}. The sensor is within the clinical important window, i.e. 25 to 500 pg mL^{-1}, allowing for differentiation between healthy people and those with low and high risk for myocardial infraction (AMI). Up to date, this is the first cTnI biosensor utilizing not only GFET technology as a transducer but also covalent modification *via* the diazonium salt reduction on the graphene basal plane to link the bioreceptor and improve the device performance.

The future of GFET biosensors is promising and is only limited by the diagnostic targets of interest. On a technical point, the GFET devices used in this work were coupled to a peristaltic pump to keep the constant flow rate over the transistor. This might be a limitation for creating a PoC device. To overcome this concern, we develop a back-gated graphene field-effect transistor where the gate electrode is separated from the graphene channel by a thin solid-state insulator (e.g. alumina, silicon oxide or organic polymer). The electrical field is propagated through the insulator and modulates the current through the graphene channel. As a result, this kind of devices would require some µL of the sample to be analyzed and the analyte could be directly introduced to the graphene surface without using the flow. As a result, this would simplify the setup and shorten the measurement time to some minutes.

A deeper understanding of the influence of PEG units on the anti-fouling properties but also on the influence on the Debey length screening still has to be obtained and is part of further work. The synthesis of novel pyrene heterofunctional ligands is another promising route for bioreceptor integration using modern surface chemistry. Combining all of these improvements, graphene-based biosensors one day will be available in a form-factor of PoC device with an excellent functionalities govern by the well-defined surface chemistry. The unique graphene properties such as transparency, flexibility, chemical and mechanical stabilities would make these devices compatible with the flexible and wearable electronics. As it was demonstrated in this work, the integrated electrodes with various layouts and functionalities can be already printed on the flexible and biocompatible substrate. Nowadays the efforts are put to demonstrate the relevance of these devices in the clinical diagnosis using real biological samples.

List of publications

1. Mishyn, V.; Hugo, A.; Rodrigues, T.; Aspermair, P.; Happy, H.; Bouchiat, V.; Boukherroub, R.; Knoll, W.; Szunerits, S. **The holy grail of pyrene-based surface ligands on the sensitivity of graphene-based field effect transistors.** *Sensors and Diagnostics*, submitted **2021.**
2. Mishyn, V.; Rodrigues, T.; Leroux, Y.R.; Butruille, L.; Woitrain, E.; Montaigne, D.; Aspermair, P.; Happy, H.; Knoll, W.; Boukherroub, R.; Szunerits, S. **Electrochemical and electronic detection of biomarkers in serum: a systematic comparison using aptamer-functionalized surfaces**. *Anal Bioanal Chem.* **2021**.
3. Mishyn, V.; Rodrigues, T.; Leroux, Y.R.; Aspermair, P.; Happy, H.; Bintinger, J.; Kleber, C.; Boukherroub, R.; Knoll, W.; Szunerits, S. **Controlled Covalent Functionalization of Graphene-Channel of a Field Effect Transistor as Ideal Platform for (Bio) sensing Applications.** *Nanoscale Horiz.* **2021**.
4. Rodrigues, T.; Mishyn, V.; Bozdogan A.; Leroux, Y. R.; Happy, H.; Kasry, A. et al. **On the detection of cTnI - a comparison of surface-plasmon optical-electrochemical-, and electronic sensing concepts.** *Ann Clin Med Case Rep.* **2021**;6(2):1-16.
5. Szunerits, S.; Pagneux, Q.; Swaidan, A.; Mishyn, V.; Roussel, A.; Cambillau, C. et al. **The role of the surface ligand on the performance of electrochemical SARS-CoV-2 antigen biosensors.** *Anal Bioanal Chem.* **2021**.
6. Aspermair, P.; Mishyn, V.; Szunerits, S.; Knoll, W. **Electronic biosensors based on graphene FETs.** *Methods Enzymol.* **2020**;642:371-401.
7. Pang, L.; Barras, A.; Mishyn, V.; Sandu, G.; Melinte, S.; Subramanian, P. et al. **Enhanced electrocatalytic hydrogen evolution on a plasmonic electrode: the importance of the Ti/TiO_2 adhesion layer.** *J Mater Chem A*. **2020**.
8. Saada, T. N.; Marques da Silva, A. G.; Subramanian, P.; Pang, L.; Adnane, N.; Djafari-Rouhani, B.; Mishyn, V. et al. **Plasmon-enhanced electrocatalytic oxygen reduction in alkaline media on gold nanohole electrodes.** *J Mater Chem A.* **2020**;8(20):10395-401.
9. Aspermair, P.; Mishyn, V.; Bintinger, J.; Happy, H.; Bagga, K.; Subramanian, P. et al. **Reduced graphene oxide–based field effect transistors for the detection of E7 protein of human papillomavirus in saliva.** *Anal Bioanal Chem.* **2020**.

10. Pang, L.; Barras, A.; Mishyn, V.; Heyte, S.; Heuson, E.; Oubaha, H. et al. **Plasmon-Driven Electrochemical Methanol Oxidation on Gold Nanohole Electrodes.** *ACS Appl Mater Interfaces*. **2020**;12(45):50426-32.
11. Amiri, M.; Tofighi, Z.; Khodayari, A.; Bezaatpour, A.; Sohrabnezhad, S.; Mishyn, V. et al. **Copper-based metal–organic framework decorated by CuO hair-like nanostructures: Electrocatalyst for oxygen evolution reaction.** *Appl Organomet Chem.* **2020**;34(10).
12. Mishyn, V.; Aspermair, P.; Leroux, Y. R.; Happy, H.; Knoll, W.; Boukherroub, R. et al. **"Click" Chemistry on Gold Electrodes Modified with Reduced Graphene Oxide by Electrophoretic Deposition.** *Surfaces.* **2019**;2(1).
13. Chekin, F.; Mishyn V.; Barras, A.; Lyskawa, J.; Ye, R.; Melinte, S. et al. **Dopamine-functionalized cyclodextrins: modification of reduced graphene oxide based electrodes and sensing of folic acid in human serum.** *Anal Bioanal Chem.* **2019**;411(20):5149-57.
14. Szunerits, S.; Mishyn, V.; Grabowska, I.; Boukherroub, R**. Electrochemical cardiovascular platforms: Current state of the art and beyond.** *Biosens Bioelectron.* **2019**;131:287-98.
15. Chekin, F.; Mishyn, V.; Ye, R.; Melinte, S.; Singh, S. K.; Kurungot, S. et al. **Graphene-modified electrodes for sensing doxorubicin hydrochloride in human plasma.** *Anal Bioanal Chem*. **2019**;411(8):1509-16.

Materials and methods

Materials and chemicals: CVD graphene on copper foil, graphene oxide (GO) and reduced graphene oxide (rGO) powder was purchased from Graphenea (Spain). Microelectrodes (ED-IDE1-Au w/o SU8) were purchased from Micrux Technologies (Spain).

Phosphate buffer tablets (PBS), tetrabutylammonium fluoride (TBAF), copper(II) sulfate ($CuSO_4$), sodium bicarbonate ($NaHCO_3$), hexamethyldisilazane (HMDS), L-ascorbic acid, ethylenediaminetetraacetic acid (EDTA), tetra-n-butylammonium hexafluorophosphate (NBu_4PF_6), methoxypolyethylene glycol azide PEG (average Mn=1,000), ammonium persulfate ($(NH_4)_2S_2O_8$), trimethoxyphenylsilane (TMPS), potassium hexacyanoferrate(II) ($K_4[Fe(CN)_6]$), potassium hexacyanoferrate(III) ($K_3[Fe(CN)_6]$), 3-amino-propyltriethoxysilane (APTES), hydrazine monohydrate, 1-pyrenebutyric acid (PBA), 1-pyrenebutyric acid N-hydroxysuccinimide ester (PBASE), N-ethyl-N′-(3-dimethylaminopropyl)carbodiimide (EDC), N-hydroxysuccinimide (NHS), folic acid (FA), ferrocenemethanol (FcMeOH), bovine serum albumin (BSA), dithiothreitol (DTT), dithiodipyridine (2PDS), hydrochloric acid (HCl), potassium hydroxide (KOH), poly(methyl methacrylate) (PMMA), 4-Nitrobenzenediazonium tetrafluoroborate, branched polyethyleneimine (PEI, Mw~25,000) and the solvents acetonitrile (CH_3CN), tetrahydrofuran (THF), acetone (C_3H_6O), isopropyl alcohol (IPA), ethanol (C_2H_5OH, EtOH), N,N-dimethylformamide (DMF) and dimethyl sulfoxide (DMSO) were purchased from Sigma-Aldrich and used as-received. Pyrene maleimide ($C_{26}H_{22}N_2O_3$, PMAL) was supplied form Lumiprobe GmbH (Germany).

The photoresist SPR 220 was purchased from Micro resist technology GmbH (Germany). Microposit MF -319 developer was supplied by Rohm and Haas Electronic Materials (USA). SVC-14 positive photoresist striper was obtained from Kayaku Advanced Materials (USA).

Azidomethylferrocene was synthesized according to literature.[135] 4-((triisopropylsilyl)ethylenyl)benzenediazonium tetrafluoroborate (TIPS-Eth-ArN_2^+) was synthesized as reported previously.[65] Pyrene-conjugated dithiopyridine (PSE) was synthetized by the group of Sanyal as described in the literature.[134] The blocking agent PEG was pre-conjugated with a PBSE linker (PyPEG) for later π-π immobilization on the rGO surface.[136] β-cyclodextrin-modified dopamine was synthetized according to the method in the literature.[6]

The 5’-azide modified troponin I aptamer (5’-N_3-TTT-TTT-CGT GCA GTA CGC CAA CCT TTC TCA TGC GCT GCC CCT CTT A-3’) and the 5’-amino modified HPV E7 aptamer NH_2-5′-$(TTT)_8$ GGG AGG ACG AUG CGG AAG CAT CAA GGG TGA TCG TTT GAC CCT CCC CAG ACG ACU CGC CCG A-3’ were purchased from integrated DNA Technologies (Leuven, Belgium). The Human Cardiac Troponin I (cTnI) was purchased from Abcam (Cambridge, UK). NP-32 peptide (MW = 3.4 kDa) was purchased from BACHEM AG (Switzerland). The HPV recombinant HPV-16 E7 (MW = 15 kDa) was obtained from LifeSpan BioSciences.

Electrochemical measurements: Electrochemical measurements (cyclic voltammetry and differential pulse voltammetry) were performed on a potentiostat/galvanostat/impedance analyzer (PalmSens4, PalmSens, The Netherlands). A conventional three-electrode cell (Micrux Technologies, Spain) was employed using a silver wire covered with silver chloride (Ag/AgCl) and a platinum mesh as the reference and auxiliary electrodes, respectively. The platform was equipped with the add-on (up to 400 µL samle volume) made of polyether ether ketone (PEEK) which is compatible with organic solvents. The IDEs or planar gold electrodes were acting as a working electrode.

Electrophoretic deposition (EPD): Autolab PGSTAT12 Potentiostat/Galvanostat Electrochemical System (Metrohm, Switzerland) was used to perform EPD and record amperograms. All the data were acquired by GPES Autolab (v.4.9) software.

Electrical sensing: Electrical measurements were conducted using a probe station source meter unit U2322A (Keysight Technologies, USA). All measurements were performed using a PMMA commercial flow cell (Micrux Technologies, Spain) with fixed flow channel geometry (16 µL), ensuring a defined flow rate of 50 µL min^{-1} to minimize mass transport limitation of the analyte to the sensor surface in all experiments. A silver chloride wire (diameter 1 mm, Sigma-Aldrich) was used to operate the FET device in liquid gate configuration with a constant source-drain bias (V_{DS}) of 50 mV.

Raman spectroscopy and imaging: Raman measurement were carried out using a visible Labram HR spectrometer (Horiba Gr, France). The Raman backscattering was excited with 473 nm excitation wavelength. The beam was focused on the sample surface through an optical objective 100x with a lateral resolution (XY) of <1 µm. The spectral resolution is better than 2 cm^{-1}. LabSpec (v.5.78.24) software was used to record and visualize the data.

Scanning electron microscope (SEM): Scanning electron microscopic images of the surfaces were obtained using an electron microscope ULTRA 55 (Zeiss, France) equipped with a thermal field emission emitter and three different detectors (EsB detector with filter grid, high efficiency In-lens SE detector and Everhart-Thornley Secondary Electron Detector). The accelerating voltage was 2 kV.

X-ray photoelectron spectrometer (XPS): X-ray photoelectron spectroscopy (XPS) was performed on a PHI 5000 VersaProbe-Scanning ESCA Microprobe (ULVAC-PHI, Japan/USA) instrument at a base pressure below $5\ 10^{-9}$ mbar. Core level spectra were acquired at pass energy of 23.5 eV with a 0.1 eV energy step. All spectra were acquired with 90º between X-ray source and analyzer and with the use of low energy electrons and low energy argon ions for charge neutralization. After subtraction of the linear background, the core-level spectra were decomposed into their components with mixed Gaussian-Lorentzian (30:70) shape lines using the CasaXPS software.

UV/Ozone cleaner: UVO-Cleaner 42-220 (Jelight, USA) with 184.9 nm and 253.7 nm excitation wavelengths was used. The light was produced by mercury vapor lamp with the average intensity of 28-32 mW cm^{-2} at 253.7 nm.

Atomic force microscopy (AFM): images in air and ambient temperate were recorded using a Bruker, Dimension 3100 AFM. The surfaces were imaged with a silicon cantilever (AppNano TM300, typical spring constant: 50 N m^{-1}) working at a frequency of 369 kHz. Image treatment and RMS (root-mean square) roughness were obtained with the WSXM software.

Optical lithography: high resolution direct lithography system for fast prototyping and maskless fabrication Dilase 650 was utilized to expose the photoresist. Laser source is 375 nm (maximum power 73 mW) with the laser spot size 10 μm and the stage travel resolution and repeatability is 100 nm. The layout of electrodes was developed in Layout Editor software.

Bibliography

1. Szunerits, S.; Boukherroub, R., Graphene-based biosensors. *Interface Focus* **2018,** *8* (3), 20160132.

2. Suvarnaphaet, P.; Pechprasarn, S., Graphene-based materials for biosensors: a review. *Sensors* **2017,** *17* (10), 2161.

3. Qlark Jr, L., Monitor and control of blood and tissue oxygen tensions. *ASAIO Journal* **1956,** *2* (1), 41-48.

4. Clark Jr, L. C.; Lyons, C., Electrode systems for continuous monitoring in cardiovascular surgery. *Annals of the New York Academy of sciences* **1962,** *102* (1), 29-45.

5. Morales, M. A.; Halpern, J. M., Guide to selecting a biorecognition element for biosensors. *Bioconjugate chemistry* **2018,** *29* (10), 3231-3239.

6. Chekin, F.; Mishyn, V.; Barras, A.; Lyskawa, J.; Ye, R.; Melinte, S.; Woisel, P.; Boukherroub, R.; Szunerits, S., Dopamine-functionalized cyclodextrins: modification of reduced graphene oxide based electrodes and sensing of folic acid in human serum. *Anal Bioanal Chem* **2019,** *411* (20), 5149-5157.

7. Whitford, D., *Proteins: structure and function*. John Wiley & Sons: 2013.

8. Branden, C. I.; Tooze, J., *Introduction to protein structure*. Garland Science: 2012.

9. Burrell, M. M., *Enzymes of molecular biology*. Springer: 1993; Vol. 16.

10. Oue, S.; Okamoto, A.; Yano, T.; Kagamiyama, H., Redesigning the substrate specificity of an enzyme by cumulative effects of the mutations of non-active site residues. *J Biol Chem* **1999,** *274* (4), 2344-9.

11. Titoiu, A. M.; Necula-Petrareanu, G.; Visinescu, D.; Dinca, V.; Bonciu, A.; Mihailescu, C. N.; Purcarea, C.; Boukherroub, R.; Szunerits, S.; Vasilescu, A., Flow injection enzymatic biosensor for aldehydes based on a Meldola Blue-Ni complex electrochemical mediator. *Mikrochim Acta* **2020,** *187* (10), 550.

12. Sharma, S.; Byrne, H.; O'Kennedy, R. J., Antibodies and antibody-derived analytical biosensors. *Essays Biochem* **2016,** *60* (1), 9-18.

13. Conroy, P. J.; Hearty, S.; Leonard, P.; O'Kennedy, R. J. In *Antibody production, design and use for biosensor-based applications*, Seminars in cell & developmental biology, Elsevier: 2009; pp 10-26.

14. Engvall, E.; Jonsson, K.; Perlmann, P., Enzyme-linked immunosorbent assay. II. Quantitative assay of protein antigen, immunoglobulin G, by means of enzyme-labelled antigen and antibody-coated tubes. *Biochim Biophys Acta* **1971,** *251* (3), 427-34.

15. Engvall, E.; Perlmann, P., Enzyme-linked immunosorbent assay (ELISA). Quantitative assay of immunoglobulin G. *Immunochemistry* **1971,** *8* (9), 871-4.

16. Engvall, E.; Perlmann, P., Enzyme-linked immunosorbent assay, Elisa. 3. Quantitation of specific antibodies by enzyme-labeled anti-immunoglobulin in antigen-coated tubes. *J Immunol* **1972,** *109* (1), 129-35.

17. Chekin, F.; Singh, S. K.; Vasilescu, A.; Dhavale, V. M.; Kurungot, S.; Boukherroub, R.; Szunerits, S., Reduced graphene oxide modified electrodes for sensitive sensing of gliadin in food samples. *ACS Sensors* **2016,** *1* (12), 1462-1470.

18. Liu, G.; Qi, M.; Zhang, Y.; Cao, C.; Goldys, E. M., Nanocomposites of gold nanoparticles and graphene oxide towards an stable label-free electrochemical immunosensor for detection of cardiac marker troponin-I. *Analytica chimica acta* **2016,** *909*, 1-8.

19. Jijie, R.; Kahlouche, K.; Barras, A.; Yamakawa, N.; Bouckaert, J.; Gharbi, T.; Szunerits, S.; Boukherroub, R., Reduced graphene oxide/polyethylenimine based immunosensor for the selective and sensitive electrochemical detection of uropathogenic Escherichia coli. *Sensors and Actuators B: Chemical* **2018,** *260*, 255-263.

20. Demarest, S. J.; Glaser, S. M., Antibody therapeutics, antibody engineering, and the merits of protein stability. *Current opinion in drug discovery & development* **2008,** *11* (5), 675-687.

21. Daniel, R. M.; Danson, M. J.; Eisenthal, R.; Lee, C. K.; Peterson, M. E., The effect of temperature on enzyme activity: new insights and their implications. *Extremophiles* **2008,** *12* (1), 51-59.

22. Neidle, S., *Nucleic acid structure and recognition*. Oxford University Press, USA: 2002.

23. Brody, L. C. Nucleic Acid. https://www.genome.gov/genetics-glossary/Nucleic-Acid (accessed 31/08/2021).

24. Tawa, K.; Knoll, W., Mismatching base-pair dependence of the kinetics of DNA-DNA hybridization studied by surface plasmon fluorescence spectroscopy. *Nucleic Acids Res* **2004,** *32* (8), 2372-7.

25. Zhou, W.; Huang, P. J.; Ding, J.; Liu, J., Aptamer-based biosensors for biomedical diagnostics. *Analyst* **2014,** *139* (11), 2627-40.

26. Aspermair, P.; Mishyn, V.; Bintinger, J.; Happy, H.; Bagga, K.; Subramanian, P.; Knoll, W.; Boukherroub, R.; Szunerits, S., Reduced graphene oxide-based field effect transistors for the

detection of E7 protein of human papillomavirus in saliva. *Anal Bioanal Chem* **2021,** *413* (3), 779-787.

27. Harley, C. C.; Rooney, A. D.; Breslin, C. B., The selective detection of dopamine at a polypyrrole film doped with sulfonated β-cyclodextrins. *Sensors and Actuators B: Chemical* **2010,** *150* (2), 498-504.

28. Saha, S.; Roy, A.; Roy, K.; Roy, M. N., Study to explore the mechanism to form inclusion complexes of β-cyclodextrin with vitamin molecules. *Scientific reports* **2016,** *6* (1), 1-12.

29. Tian, X.; Cheng, C.; Yuan, H.; Du, J.; Xiao, D.; Xie, S.; Choi, M. M., Simultaneous determination of l-ascorbic acid, dopamine and uric acid with gold nanoparticles–β-cyclodextrin–graphene-modified electrode by square wave voltammetry. *Talanta* **2012,** *93*, 79-85.

30. Liang, W.; Rong, Y.; Fan, L.; Dong, W.; Dong, Q.; Yang, C.; Zhong, Z.; Dong, C.; Shuang, S.; Wong, W.-Y., 3D graphene/hydroxypropyl-β-cyclodextrin nanocomposite as an electrochemical chiral sensor for the recognition of tryptophan enantiomers. *Journal of Materials Chemistry C* **2018,** *6* (47), 12822-12829.

31. Aspermair, P.; Mishyn, V.; Szunerits, S.; Knoll, W., Electronic biosensors based on graphene FETs. *Methods Enzymol* **2020,** *642*, 371-401.

32. Weber, J.; Kumar, A.; Kumar, A.; Bhansali, S., Novel lactate and pH biosensor for skin and sweat analysis based on single walled carbon nanotubes. *Sensors and Actuators B: Chemical* **2006,** *117* (1), 308-313.

33. Zeng, S.; Yong, K.-T.; Roy, I.; Dinh, X.-Q.; Yu, X.; Luan, F., A review on functionalized gold nanoparticles for biosensing applications. *Plasmonics* **2011,** *6* (3), 491-506.

34. Huang, Y.; Dong, X.; Shi, Y.; Li, C. M.; Li, L.-J.; Chen, P., Nanoelectronic biosensors based on CVD grown graphene. *Nanoscale* **2010,** *2* (8), 1485-1488.

35. Darabdhara, G.; Das, M. R.; Singh, S. P.; Rengan, A. K.; Szunerits, S.; Boukherroub, R., Ag and Au nanoparticles/reduced graphene oxide composite materials: synthesis and application in diagnostics and therapeutics. *Advances in colloid and interface science* **2019,** *271*, 101991.

36. Geim, A. K., Graphene: status and prospects. *science* **2009,** *324* (5934), 1530-1534.

37. Zhong, J.-H.; Zhang, J.; Jin, X.; Liu, J.-Y.; Li, Q.; Li, M.-H.; Cai, W.; Wu, D.-Y.; Zhan, D.; Ren, B., Quantitative correlation between defect density and heterogeneous electron transfer rate of single layer graphene. *Journal of the American Chemical Society* **2014,** *136* (47), 16609-16617.

38. Banszerus, L.; Schmitz, M.; Engels, S.; Dauber, J.; Oellers, M.; Haupt, F.; Watanabe, K.; Taniguchi, T.; Beschoten, B.; Stampfer, C., Ultrahigh-mobility graphene devices from chemical vapor deposition on reusable copper. *Science advances* **2015,** *1* (6), e1500222.

39. Zhou, M.; Zhai, Y.; Dong, S., Electrochemical sensing and biosensing platform based on chemically reduced graphene oxide. *Analytical chemistry* **2009,** *81* (14), 5603-5613.

40. Szunerits, S.; Boukherroub, R., Graphene-based nanomaterials in innovative electrochemistry. *Current Opinion in Electrochemistry* **2018,** *10*, 24-30.

41. Chekin, F.; Vasilescu, A.; Jijie, R.; Singh, S. K.; Kurungot, S.; Iancu, M.; Badea, G.; Boukherroub, R.; Szunerits, S., Sensitive electrochemical detection of cardiac troponin I in serum and saliva by nitrogen-doped porous reduced graphene oxide electrode. *Sensors and Actuators B: Chemical* **2018,** *262*, 180-187.

42. Fu, W.; Jiang, L.; van Geest, E. P.; Lima, L. M.; Schneider, G. F., Sensing at the surface of graphene field-effect transistors. *Advanced Materials* **2017,** *29* (6), 1603610.

43. Liu, J.; Tang, J.; Gooding, J. J., Strategies for chemical modification of graphene and applications of chemically modified graphene. *Journal of materials chemistry* **2012,** *22* (25), 12435-12452.

44. Avouris, P.; Dimitrakopoulos, C., Graphene: synthesis and applications. *Materials today* **2012,** *15* (3), 86-97.

45. Losurdo, M.; Giangregorio, M. M.; Capezzuto, P.; Bruno, G., Graphene CVD growth on copper and nickel: role of hydrogen in kinetics and structure. *Physical Chemistry Chemical Physics* **2011,** *13* (46), 20836-20843.

46. Vasilescu, A.; Boulahneche, S.; Chekin, F.; Gáspár, S.; Medjram, M. S.; Diagne, A. A.; Singh, S. K.; Kurungot, S.; Boukherroub, R.; Szunerits, S., Porous reduced graphene oxide modified electrodes for the analysis of protein aggregation. Part 1: Lysozyme aggregation at pH 2 and 7.4. *Electrochimica Acta* **2017,** *254*, 375-383.

47. Yi, M.; Shen, Z., A review on mechanical exfoliation for the scalable production of graphene. *Journal of Materials Chemistry A* **2015,** *3* (22), 11700-11715.

48. Ciesielski, A.; Samori, P., Graphene via sonication assisted liquid-phase exfoliation. *Chemical Society Reviews* **2014,** *43* (1), 381-398.

49. Hummers Jr, W. S.; Offeman, R. E., Preparation of graphitic oxide. *Journal of the american chemical society* **1958,** *80* (6), 1339-1339.

50. Pei, S.; Cheng, H.-M., The reduction of graphene oxide. *Carbon* **2012,** *50* (9), 3210-3228.

51. Park, S.; An, J.; Potts, J. R.; Velamakanni, A.; Murali, S.; Ruoff, R. S., Hydrazine-reduction of graphite-and graphene oxide. *Carbon* **2011,** *49* (9), 3019-3023.

52. Zhang, J.; Yang, H.; Shen, G.; Cheng, P.; Zhang, J.; Guo, S., Reduction of graphene oxide via L-ascorbic acid. *Chemical communications* **2010,** *46* (7), 1112-1114.

53. Chua, C. K.; Pumera, M., Reduction of graphene oxide with substituted borohydrides. *Journal of Materials Chemistry A* **2013,** *1* (5), 1892-1898.

54. Huh, S. H., Thermal reduction of graphene oxide. *Physics and Applications of Graphene-Experiments* **2011,** *19*, 73-90.

55. Shao, Y.; Wang, J.; Engelhard, M.; Wang, C.; Lin, Y., Facile and controllable electrochemical reduction of graphene oxide and its applications. *Journal of Materials Chemistry* **2010,** *20* (4), 743-748.

56. Stankovich, S.; Dikin, D. A.; Piner, R. D.; Kohlhaas, K. A.; Kleinhammes, A.; Jia, Y.; Wu, Y.; Nguyen, S. T.; Ruoff, R. S., Synthesis of graphene-based nanosheets via chemical reduction of exfoliated graphite oxide. *carbon* **2007,** *45* (7), 1558-1565.

57. Piccinini, E.; Bliem, C.; Reiner-Rozman, C.; Battaglini, F.; Azzaroni, O.; Knoll, W., Enzyme-polyelectrolyte multilayer assemblies on reduced graphene oxide field-effect transistors for biosensing applications. *Biosensors and Bioelectronics* **2017,** *92*, 661-667.

58. Reiner-Rozman, C.; Hasler, R.; Andersson, J.; Rodrigues, T.; Bozdogan, A.; Bintinger, J.; Aspermair, P., The top performer: Towards optimized parameters for reduced graphene oxide uniformity by spin coating. *Micro & Nano Letters* **2021**.

59. Chiong, S.; Goh, P.; Ismail, A., Novel hydrophobic PVDF/APTES-GO nanocomposite for natural gas pipelines coating. *Journal of Natural Gas Science and Engineering* **2017,** *42*, 190-202.

60. Larisika, M.; Huang, J.; Tok, A.; Knoll, W.; Nowak, C., An improved synthesis route to graphene for molecular sensor applications. *Materials Chemistry and Physics* **2012,** *136* (2-3), 304-308.

61. Diba, M.; García-Gallastegui, A.; Taylor, R. N. K.; Pishbin, F.; Ryan, M. P.; Shaffer, M. S.; Boccaccini, A. R., Quantitative evaluation of electrophoretic deposition kinetics of graphene oxide. *Carbon* **2014,** *67*, 656-661.

62. Suk, J. W.; Kitt, A.; Magnuson, C. W.; Hao, Y.; Ahmed, S.; An, J.; Swan, A. K.; Goldberg, B. B.; Ruoff, R. S., Transfer of CVD-grown monolayer graphene onto arbitrary substrates. *ACS nano* **2011,** *5* (9), 6916-6924.

63. Hu, Z.; Prasad Sinha, D.; Ung Lee, J.; Liehr, M., Substrate dielectric effects on graphene field effect transistors. *Journal of Applied Physics* **2014,** *115* (19), 194507.

64. Nagashio, K.; Nishimura, T.; Kita, K.; Toriumi, A., Systematic investigation of the intrinsic channel properties and contact resistance of monolayer and multilayer graphene field-effect transistor. *Japanese Journal of Applied Physics* **2010,** *49* (5R), 051304.

65. Leroux, Y. R.; Hapiot, P., Nanostructured monolayers on carbon substrates prepared by electrografting of protected aryldiazonium salts. *Chemistry of Materials* **2013,** *25* (3), 489-495.

66. Lomeda, J. R.; Doyle, C. D.; Kosynkin, D. V.; Hwang, W.-F.; Tour, J. M., Diazonium functionalization of surfactant-wrapped chemically converted graphene sheets. *Journal of the American Chemical Society* **2008,** *130* (48), 16201-16206.

67. Liu, J.; Li, C.; Brans, T.; Harizaj, A.; Van de Steene, S.; De Beer, T.; De Smedt, S.; Szunerits, S.; Boukherroub, R.; Xiong, R., Surface functionalization with polyethylene glycol and polyethyleneimine improves the performance of graphene-based materials for safe and efficient intracellular delivery by laser-induced photoporation. *International journal of molecular sciences* **2020,** *21* (4), 1540.

68. Gómez-Santos, G., Thermal van der Waals interaction between graphene layers. *Physical Review B* **2009,** *80* (24), 245424.

69. Sabio, J.; Seoanez, C.; Fratini, S.; Guinea, F.; Neto, A. C.; Sols, F., Electrostatic interactions between graphene layers and their environment. *Physical Review B* **2008,** *77* (19), 195409.

70. Luan, Y.-G.; Zhang, X.-A.; Jiang, S.-L.; Chen, J.-H.; Lyu, Y.-F., Self-healing supramolecular polymer composites by hydrogen bonding interactions between hyperbranched polymer and graphene oxide. *Chinese Journal of Polymer Science* **2018,** *36* (5), 584-591.

71. Björk, J.; Hanke, F.; Palma, C.-A.; Samori, P.; Cecchini, M.; Persson, M., Adsorption of aromatic and anti-aromatic systems on graphene through π− π stacking. *The Journal of Physical Chemistry Letters* **2010,** *1* (23), 3407-3412.

72. Zhang, Z.; Huang, H.; Yang, X.; Zang, L., Tailoring electronic properties of graphene by π–π stacking with aromatic molecules. *The Journal of Physical Chemistry Letters* **2011,** *2* (22), 2897-2905.

73. Plutnar, J.; Pumera, M.; Sofer, Z., The chemistry of CVD graphene. *Journal of Materials Chemistry C* **2018,** *6* (23), 6082-6101.

74. Lee, W. H.; Park, J.; Sim, S. H.; Lim, S.; Kim, K. S.; Hong, B. H.; Cho, K., Surface-directed molecular assembly of pentacene on monolayer graphene for high-performance organic transistors. *Journal of the American Chemical Society* **2011,** *133* (12), 4447-4454.

75. Loh, K. P.; Bao, Q.; Ang, P. K.; Yang, J., The chemistry of graphene. *Journal of Materials Chemistry* **2010,** *20* (12), 2277-2289.

76. Salavagione, H. J.; Martínez, G.; Ellis, G., Recent advances in the covalent modification of graphene with polymers. *Macromolecular rapid communications* **2011,** *32* (22), 1771-1789.

77. Asha, J. B.; Suresh, P., Covalently Modified Graphene Oxide as Highly Fluorescent and Sustainable Carbonaceous Chemosensor for Selective Detection of Zirconium ion in Complete Aqueous Medium. *ACS Sustainable Chemistry & Engineering* **2020,** *8* (38), 14301-14311.

78. Rodrigues, T.; Mishyn, V.; Bozdogan, A.; Leroux, Y.; Happy, H.; Kasry, A.; Boukherroub, R.; Dostalek, J.; Aspermair, P.; Bintinger, J., On the detection of cTnI-a comparison of surface-plasmon optical-electrochemical-, and electronic sensing concepts. *Annals of Clinical and Medical Case Reports* **2021,** *6* (2), 1-16.

79. Yuan, W.; Zhou, Y.; Li, Y.; Li, C.; Peng, H.; Zhang, J.; Liu, Z.; Dai, L.; Shi, G., The edge- and basal-plane-specific electrochemistry of a single-layer graphene sheet. *Scientific reports* **2013,** *3* (1), 1-7.

80. Mishyn, V.; Rodrigues, T.; Leroux, Y.; Aspermair, P.; Happy, H.; Bintinger, J.; Kleber, C.; Boukherroub, R.; Knoll, W.; Szunerits, S., Controlled Covalent Functionalization of Graphene-Channel of a Field Effect Transistor as Ideal Platform for (Bio) sensing Applications. *Nanoscale Horizons* **2021**.

81. Leroux, Y. R.; Fei, H.; Noël, J.-M.; Roux, C.; Hapiot, P., Efficient covalent modification of a carbon surface: use of a silyl protecting group to form an active monolayer. *Journal of the American Chemical Society* **2010,** *132* (40), 14039-14041.

82. Paulus, G. L.; Wang, Q. H.; Strano, M. S., Covalent electron transfer chemistry of graphene with diazonium salts. *Accounts of chemical research* **2013,** *46* (1), 160-170.

83. Ambrosio, G.; Brown, A.; Daukiya, L.; Drera, G.; Di Santo, G.; Petaccia, L.; De Feyter, S.; Sangaletti, L.; Pagliara, S., Impact of covalent functionalization by diazonium chemistry on the electronic properties of graphene on SiC. *Nanoscale* **2020,** *12* (16), 9032-9037.

84. Yang, H.; Li, F.; Shan, C.; Han, D.; Zhang, Q.; Niu, L.; Ivaska, A., Covalent functionalization of chemically converted graphene sheets via silane and its reinforcement. *Journal of Materials Chemistry* **2009,** *19* (26), 4632-4638.

85. Park, J.; Yan, M., Covalent functionalization of graphene with reactive intermediates. *Accounts of chemical research* **2013,** *46* (1), 181-189.

86. Wang, A.; Yu, W.; Huang, Z.; Zhou, F.; Song, J.; Song, Y.; Long, L.; Cifuentes, M. P.; Humphrey, M. G.; Zhang, L., Covalent functionalization of reduced graphene oxide with

porphyrin by means of diazonium chemistry for nonlinear optical performance. *Scientific reports* **2016,** *6* (1), 1-12.

87. Zhang, X.; Wan, S.; Pu, J.; Wang, L.; Liu, X., Highly hydrophobic and adhesive performance of graphene films. *Journal of Materials Chemistry* **2011,** *21* (33), 12251-12258.

88. Russo, C. J.; Passmore, L. A., Controlling protein adsorption on graphene for cryo-EM using low-energy hydrogen plasmas. *Nature Methods* **2014,** *11* (6), 649-652.

89. He, L.; Pagneux, Q.; Larroulet, I.; Serrano, A. Y.; Pesquera, A.; Zurutuza, A.; Mandler, D.; Boukherroub, R.; Szunerits, S., Label-free femtomolar cancer biomarker detection in human serum using graphene-coated surface plasmon resonance chips. *Biosensors and Bioelectronics* **2017,** *89*, 606-611.

90. Sapner, V. S.; Chavan, P. P.; Digraskar, R. V.; Narwade, S. S.; Mulik, B. B.; Mali, S. M.; Sathe, B. R., Tyramine Functionalized Graphene: Metal-Free Electrochemical Non-Enzymatic Biosensing of Hydrogen Peroxide. *ChemElectroChem* **2018,** *5* (21), 3191-3197.

91. Faria, L. V.; Pereira, J. F.; Azevedo, G. C.; Matos, M. A.; Munoz, R. A.; Matos, R. C., Square-wave voltammetry determination of ciprofloxacin in pharmaceutical formulations and milk using a reduced graphene oxide sensor. *Journal of the Brazilian Chemical Society* **2019,** *30*, 1947-1954.

92. He, L.; Wang, Q.; Mandler, D.; Li, M.; Boukherroub, R.; Szunerits, S., Detection of folic acid protein in human serum using reduced graphene oxide electrodes modified by folic-acid. *Biosensors and Bioelectronics* **2016,** *75*, 389-395.

93. Ji, D.; Liu, L.; Li, S.; Chen, C.; Lu, Y.; Wu, J.; Liu, Q., Smartphone-based cyclic voltammetry system with graphene modified screen printed electrodes for glucose detection. *Biosensors and Bioelectronics* **2017,** *98*, 449-456.

94. Aristov, N.; Habekost, A., Cyclic voltammetry-A versatile electrochemical method investigating electron transfer processes. *World J. Chem. Educ* **2015,** *3* (5), 115-119.

95. Ngamchuea, K.; Eloul, S.; Tschulik, K.; Compton, R. G., Planar diffusion to macro disc electrodes—what electrode size is required for the Cottrell and Randles-Sevcik equations to apply quantitatively? *Journal of Solid State Electrochemistry* **2014,** *18* (12), 3251-3257.

96. Roland, B. K.; Flora, W. H.; Armstrong, N. R.; Zheng, Z., Tetrameric arrays of the [Re6 (μ3-Se) 8] 2+ clusters supported by a porphyrin core: synthesis, characterization, and electrochemical studies. *Comptes Rendus Chimie* **2005,** *8* (11-12), 1798-1807.

97. Oprea, R.; Peteu, S. F.; Subramanian, P.; Qi, W.; Pichonat, E.; Happy, H.; Bayachou, M.; Boukherroub, R.; Szunerits, S., Peroxynitrite activity of hemin-functionalized reduced graphene oxide. *Analyst* **2013,** *138* (15), 4345-4352.

98. Rezaei, B.; Irannejad, N., Electrochemical detection techniques in biosensor applications. In *Electrochemical Biosensors*, Elsevier: 2019; pp 11-43.

99. Martínez, M.; Tseng, Y.; Ormategui, N.; Loinaz, I.; Eritja, R.; Salvador, J. P.; Marco, M. P.; Bokor, J., Carbon nanotubes field effect transistors biosensors. *Boletín del Grupo Español del Carbón* **2012,** (23), 2-6.

100. Smith, R.; Geary, S. M.; Salem, A. K., Silicon nanowires and their impact on cancer detection and monitoring. *ACS Applied Nano Materials* **2020,** *3* (9), 8522-8536.

101. Tung, N. T.; Tue, P. T.; Lien, T. T. N.; Ohno, Y.; Maehashi, K.; Matsumoto, K.; Nishigaki, K.; Biyani, M.; Takamura, Y., Peptide aptamer-modified single-walled carbon nanotube-based transistors for high-performance biosensors. *Scientific reports* **2017,** *7* (1), 1-9.

102. Shen, M.-Y.; Li, B.-R.; Li, Y.-K., Silicon nanowire field-effect-transistor based biosensors: From sensitive to ultra-sensitive. *Biosensors and Bioelectronics* **2014,** *60*, 101-111.

103. Vaziri, S., Fabrication and characterization of graphene field effect transistors. 2011.

104. Ping, J.; Vishnubhotla, R.; Vrudhula, A.; Johnson, A. C., Scalable production of high-sensitivity, label-free DNA biosensors based on back-gated graphene field effect transistors. *ACS nano* **2016,** *10* (9), 8700-8704.

105. Reiner-Rozman, C.; Larisika, M.; Nowak, C.; Knoll, W., Graphene-based liquid-gated field effect transistor for biosensing: Theory and experiments. *Biosens Bioelectron* **2015,** *70*, 21-7.

106. Wang, S.; Hossain, M. Z.; Shinozuka, K.; Shimizu, N.; Kitada, S.; Suzuki, T.; Ichige, R.; Kuwana, A.; Kobayashi, H., Graphene field-effect transistor biosensor for detection of biotin with ultrahigh sensitivity and specificity. *Biosensors and Bioelectronics* **2020,** *165*, 112363.

107. Lin, C. T.; Loan, P. T. K.; Chen, T. Y.; Liu, K. K.; Chen, C. H.; Wei, K. H.; Li, L. J., Label-Free Electrical detection of DNA hybridization on graphene using Hall Effect measurements: revisiting the sensing mechanism. *Advanced Functional Materials* **2013,** *23* (18), 2301-2307.

108. Chen, Z.; Appenzeller, J. In *Mobility extraction and quantum capacitance impact in high performance graphene field-effect transistor devices*, 2008 IEEE international electron devices meeting, IEEE: 2008; pp 1-4.

109. Bolotin, K. I.; Sikes, K. J.; Jiang, Z.; Klima, M.; Fudenberg, G.; Hone, J.; Kim, P.; Stormer, H., Ultrahigh electron mobility in suspended graphene. *Solid state communications* **2008,** *146* (9-10), 351-355.

110. Lang, M.; Luo, D.; Yang, G.; Mei, Q.; Feng, G.; Yang, Y.; Liu, Z.; Chen, Q.; Wu, L., An ultrasensitive electrochemical sensing platform for the detection of cTnI based on aptamer recognition and signal amplification assisted by TdT. *RSC Adv.* **2020,** *10* (60), 36396-36403.

111. Jo, H.; Her, J.; Lee, H.; Shim, Y.-B.; Ban, C., Highly sensitive amperometric detection of cardiac troponin I using sandwich aptamers and screen-printed carbon electrodes. *Talanta.* **2017,** *165*, 442-448.

112. Qiao, X.; Li, K.; Xu, J.; Cheng, N.; Sheng, Q.; Cao, W.; Yue, T.; Zheng, J., Novel electrochemical sensing platform for ultrasensitive detection of cardiac troponin I based on aptamer-MoS2 nanoconjugates. *Biosens. Bioelectron.* **2018,** *113*, 142-147.

113. Sun, D.; Luo, Z.; Lu, J.; Zhang, S.; Che, T.; Chen, Z.; Zhang, L., Electrochemical dual-aptamer-based biosensor for nonenzymatic detection of cardiac troponin I by nanohybrid electrocatalysts labeling combined with DNA nanotetrahedron structure. *Biosens. Bioelectron.* **2019,** *134*, 49-56.

114. Negahdary, M.; Behjati-Ardakani, M.; Sattarahmady, N.; Yadegari, H.; Heli, H., Electrochemical aptasensing of human cardiac troponin I based on an array of gold nanodumbbells-Applied to early detection of myocardial infarction. *Sens. Actuators, B.* **2017,** *252*, 62-71.

115. Chekin, F.; Vasilescu, A.; Jijie, R.; Singh, S. K.; Kurungot, S.; Iancu, M.; Badea, G.; Boukherroub, R.; Szunerits, S., Sensitive electrochemical detection of cardiac troponin I in serum and saliva by nitrogen-doped porous reduced graphene oxide electrode. *Sens. Actuators, B.* **2018,** *262*, 180-187.

116. Grabowska, I.; Sharma, N.; Vasilescu, A.; Iancu, M.; Badea, G.; Boukherroub, R.; Ogale, S.; Szunerits, S., Electrochemical aptamer-based biosensors for the detection of cardiac biomarkers. *ACS omega.* **2018,** *3* (9), 12010-12018.

117. Batra, B.; Narwal, V.; Kalra, V.; Sharma, M.; Rana, J., Folic acid biosensors: A review. *Process Biochemistry* **2020,** *92*, 343-354.

118. Mishyn, V.; Aspermair, P.; Leroux, Y.; Happy, H.; Knoll, W.; Boukherroub, R.; Szunerits, S., "Click" chemistry on gold electrodes modified with reduced graphene oxide by electrophoretic deposition. *Surfaces* **2019,** *2* (1), 193-204.

119. Jo, H.; Gu, H.; Jeon, W.; Youn, H.; Her, J.; Kim, S. K.; Lee, J.; Shin, J. H.; Ban, C., Electrochemical aptasensor of cardiac troponin I for the early diagnosis of acute myocardial infarction. *Anal Chem* **2015,** *87* (19), 9869-75.

120. Chekin, F.; Bagga, K.; Subramanian, P.; Jijie, R.; Singh, S. K.; Kurungot, S.; Boukherroub, R.; Szunerits, S., Nucleic aptamer modified porous reduced graphene oxide/MoS2 based electrodes for viral detection: Application to human papillomavirus (HPV). *Sensors and Actuators B: Chemical* **2018,** *262*, 991-1000.

121. Gao, N.; Gao, T.; Yang, X.; Dai, X.; Zhou, W.; Zhang, A.; Lieber, C. M., Specific detection of biomolecules in physiological solutions using graphene transistor biosensors. *Proceedings of the National Academy of Sciences* **2016,** *113* (51), 14633-14638.

122. Mishyn, V.; Rodrigues, T.; Leroux, Y. R.; Butruille, L.; Woitrain, E.; Montaigne, D.; Aspermair, P.; Happy, H.; Knoll, W.; Boukherroub, R.; Szunerits, S., Electrochemical and electronic detection of biomarkers in serum: a systematic comparison using aptamer-functionalized surfaces. *Anal Bioanal Chem* **2021**.

123. Lee, W. C.; Lee, H.; Lim, J.; Park, Y. J., An effective electrical sensing scheme using AC electrothermal flow on a biosensor platform based on a carbon nanotube network. *Appl. Phys. Lett.* **2016,** *109* (22), 223701.

124. Kutovyi, Y.; Li, J.; Zadorozhnyi, I.; Hlukhova, H.; Boichuk, N.; Yehorov, D.; Menger, M.; Vitusevich, S., Highly Sensitive and Fast Detection of C-Reactive Protein and Troponin Biomarkers Using Liquid-gated Single Silicon Nanowire Biosensors. *MRS Adv.* **2020,** *5* (16), 835-846.

125. Sarangadharan, I.; Regmi, A.; Chen, Y.-W.; Hsu, C.-P.; Chen, P.-c.; Chang, W.-H.; Lee, G.-Y.; Chyi, J.-I.; Shiesh, S.-C.; Lee, G.-B., High sensitivity cardiac troponin I detection in physiological environment using AlGaN/GaN High Electron Mobility Transistor (HEMT) Biosensors. *Biosens. Bioelectron.* **2018,** *100*, 282-289.

126. Sinha, A.; Tai, T.-Y.; Li, K.-H.; Gopinathan, P.; Chung, Y.-D.; Sarangadharan, I.; Ma, H.-P.; Huang, P.-C.; Shiesh, S.-C.; Wang, Y.-L., An integrated microfluidic system with field-effect-transistor sensor arrays for detecting multiple cardiovascular biomarkers from clinical samples. *Biosens. Bioelectron.* **2019,** *129*, 155-163.

127. Chekin, F.; Myshin, V.; Ye, R.; Melinte, S.; Singh, S. K.; Kurungot, S.; Boukherroub, R.; Szunerits, S., Graphene-modified electrodes for sensing doxorubicin hydrochloride in human plasma. *Anal Bioanal Chem* **2019,** *411* (8), 1509-1516.

128. Hinnemo, M.; Zhao, J.; Ahlberg, P.; Hagglund, C.; Djurberg, V.; Scheicher, R. H.; Zhang, S. L.; Zhang, Z. B., On Monolayer Formation of Pyrenebutyric Acid on Graphene. *Langmuir* **2017,** *33* (15), 3588-3593.

129. Hao, Y.; Wang, Y.; Wang, L.; Ni, Z.; Wang, Z.; Wang, R.; Koo, C. K.; Shen, Z.; Thong, J. T., Probing layer number and stacking order of few-layer graphene by Raman spectroscopy. *Small* **2010,** *6* (2), 195-200.

130. Seo, G.; Lee, G.; Kim, M. J.; Baek, S.-H.; Choi, M.; Ku, K. B.; Lee, C.-S.; Jun, S.; Park, D.; Kim, H. G., Rapid detection of COVID-19 causative virus (SARS-CoV-2) in human nasopharyngeal swab specimens using field-effect transistor-based biosensor. *ACS nano* **2020,** *14* (4), 5135-5142.

131. Northrop, B. H.; Frayne, S. H.; Choudhary, U., Thiol–maleimide “click” chemistry: evaluating the influence of solvent, initiator, and thiol on the reaction mechanism, kinetics, and selectivity. *Polymer Chemistry* **2015,** *6* (18), 3415-3430.

132. Fei, Z.; Liu, B.; Zhu, M.; Wang, W.; Yu, D., Antibacterial finishing of cotton fabrics based on thiol-maleimide click chemistry. *Cellulose* **2018,** *25* (5), 3179-3188.

133. Pounder, R. J.; Stanford, M. J.; Brooks, P.; Richards, S. P.; Dove, A. P., Metal free thiol–maleimide ‘Click’reaction as a mild functionalisation strategy for degradable polymers. *Chemical communications* **2008,** (41), 5158-5160.

134. Gevrek, T. N.; Cosar, M.; Aydin, D.; Kaga, E.; Arslan, M.; Sanyal, R.; Sanyal, A., Facile Fabrication of a Modular "Catch and Release" Hydrogel Interface: Harnessing Thiol-Disulfide Exchange for Reversible Protein Capture and Cell Attachment. *ACS Appl Mater Interfaces* **2018,** *10* (17), 14399-14409.

135. Casas-Solvas, J. M.; Vargas-Berenguel, A.; Capitán-Vallvey, L. F.; Santoyo-González, F., Convenient methods for the synthesis of ferrocene− carbohydrate conjugates. *Organic letters* **2004,** *6* (21), 3687-3690.

136. Liu, J.; Bibari, O.; Mailley, P.; Dijon, J.; Rouviere, E.; Sauter-Starace, F.; Caillat, P.; Vinet, F.; Marchand, G., Stable non-covalent functionalisation of multi-walled carbon nanotubes by pyrene–polyethylene glycol through π–π stacking. *New Journal of Chemistry* **2009,** *33* (5), 1017-1024.